EPITAXIAL GRAPHENE ON SILICON CARBIDE: LOW-VACUUM GROWTH, CHARACTERIZATION, AND DEVICE FABRICATION

A Thesis
Presented to
The Academic Faculty

by

Michael W. Sprinkle

In Partial Fulfillment
of the Requirements for the Degree
Doctor of Philosophy in the
School of Physics

Georgia Institute of Technology
August 2010

EPITAXIAL GRAPHENE ON SILICON CARBIDE: LOW-VACUUM GROWTH, CHARACTERIZATION, AND DEVICE FABRICATION

Approved by:

Professor Walt A. de Heer, Advisor
School of Physics
Georgia Institute of Technology

Professor Edward H. Conrad, Advisor
School of Physics
Georgia Institute of Technology

Professor Phillip N. First
School of Physics
Georgia Institute of Technology

Professor Andrew Zangwill
School of Physics
Georgia Institute of Technology

Professor John D. Cressler
School of Electrical and Computer Engineering
Georgia Institute of Technology

Date Approved: 2 June 2010

To carbon, without which I wouldn't be what I am today.

ACKNOWLEDGEMENTS

I sincerely thank my advisors and thesis committee for their support, encouragement, and endless questions. I am deeply grateful to the other distinguished scientists, including Drs. Claire Berger, Patrick Soukiassian, Jeff J. Peterson, Amina Taleb-Ibrahimi, Antonio Tejeda, Xiaosong Wu, and Valery Borovikov, with whom I have been privileged to work and learn. I would like to thank my fellow graduate students, including Dr. Zhimin Song, Dr. Tianbo Li, Dr. Xuebin Li, Dr. Greg Rutter, Dr. Joanna Hass, Dr. Nikhil Sharma, Dr. Miguel Rubio Roy, Jorge Millán-Otoya, Farhana Zaman, Fan Ming, D. Lee Miller, Kevin Kubista, D. Britt Torrance, Ming Ruan, Yike Hu, John Hankinson, Jeremy Hicks, and Baiqian Zhang, for their help in executing all of the work presented here. I thank my family, including my wife, Brandalyn, and daughter, Lauren, for their help and encouragement. Finally, I am grateful to my undergraduate thesis advisor, Prof. Robert C. Davis, for excellent research opportunities and guidance, and to Mr. Jerome Lubetz, for introducing me to the elegance of physics. My thanks to all, for teaching me science and supporting me in that pursuit.

TABLE OF CONTENTS

LIST OF TABLES

LIST OF FIGURES

SUMMARY

In the past several years, epitaxial graphene on silicon carbide has been transformed from an academic curiosity of social scientists to a leading candidate material to replace silicon in post-CMOS electronics. This has come with rapid development of growth technologies, improved understanding of epitaxial graphene on the polar faces of silicon carbide, and new device fabrication techniques. The contributions of this thesis include refinement and improved understanding of graphene growth on the silicon- and carbon-faces in the context of managed local silicon partial pressure, high-throughput epitaxial graphene thickness measurement and uniformity characterization by ellipsometry, observations of nearly ideal graphene band structures on rotationally stacked carbon-face multilayer epitaxial graphene, presentation of initial experiments on localized *in situ* chemical modification of epitaxial graphene for an alternate path to semiconducting behavior, and novel device fabrication methods to exploit the crystal structure of the silicon carbide substrate. The latter is a particularly exciting foray into three dimensional patterning of the substrate that may eliminate the critical problem of edge roughness in graphene nanoribbons.

CHAPTER I

INTRODUCTION

1.1 Graphene

Graphene is a single (atomically thin) sheet of graphite. It's made up of a honeycomb-like array of carbon atoms with two (symmetric) atoms per fundamental *unit cell*, as pictured in Fig. 1.1. The structure and symmetry of graphene give it unique properties; in-plane C–C sigma-bonds impart exceptional mechanical strength (think of C–C bonds in diamond), while out-of-plane p-orbitals collectively constitute molecular π-oribitals that conduct electricity extremely well. Philip Wallace calculated in the 1940s[102] that the π energy bands corresponding to these orbitals are conical, intersecting in a single point in the areas of interest,[1] as opposed to the parabolic valence and conduction bands observed in most materials.

This is illustrated in Fig. 1.2a. In this plot of the π-band—charge carrier (electrons and holes[2]) energy $\mathcal{E}$ versus carrier momentum k—as calculated by Wallace, six cones are observed at the corners of the fundamental cell in momentum-space known as the *Brillouin zone*. The Brillouin zone is marked on the contour plot in Fig. 1.2b, with the cone locations K and K' indicated. Fig. 1.2c and d show cross-sections through the K and K' cones. Near $\mathcal{E} = 0$ eV (the charge neutrality point), the structure is

[1] Wallace's tight-binding calculation shows that the π-bands are described by

$$\mathcal{E}(\mathbf{k}) = \pm t\sqrt{1 + 4\cos^2\left(\frac{k_y a}{2}\right) + 4\cos\left(\frac{k_y a}{2}\right)\cos\left(\frac{\sqrt{3}k_x a}{2}\right)}, \tag{1.1}$$

where $t \approx 3\,\text{eV}$ is the nearest neighbor hopping energy and $a = 2.46\,\text{Å}$ is the graphene in-plane lattice constant. This is approximately conical near the K-points, $\mathbf{K}_\pm = \pm 2\pi/a(0, 2/3)$. There,

$$\mathcal{E}(\mathbf{k}) \approx \pm\hbar v_f |\mathbf{k}\text{-}\mathbf{K}_\pm|, \tag{1.2}$$

where $v_f \equiv \sqrt{3}ta/2\hbar$ is the Fermi velocity, which is constant near the K-points.

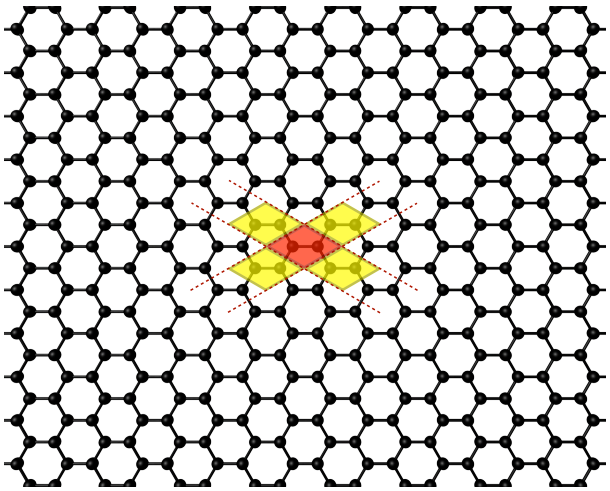

Figure 1.1: Graphene is made up of a hexagonal array of carbon atoms. The unit cell, the fundamental unit from which the graphene lattice may be constructed, consists of two carbon atoms, as highlighted here in red.

approximately conical.

These conical bands prompt comparison of charge carriers in graphene to photons and neutrinos, which travel at a constant speed (c, the speed of light) and have no mass. Electrons in graphene may analogously be considered effectively massless, and travel at constant speed $\approx c/300$. In this sense, they may be treated mathematically as relativistic particles. Deeper comparisons to relativistic neutrino physics arise due to symmetry.

The symmetry of the graphene lattice has profound effects on conduction. There are two distinct (triangular) *sub-lattices* corresponding to the two equivalent atoms in the unit cell that make up identical, yet orthogonal molecular orbitals. The binary quantum number that describes these orbitals/sublattices is referred to as *pseudo-spin*, in comparison to the (real) spin of neutrinos. By formulating the pseudospin as a vector in the momentum plane, it may be stated that the carrier momentum must always be parallel or anti-parallel (*i.e.*, parallel, with opposite direction) to the pseudospin, as illustrated in Fig. 1.3. This, in fact, is precisely the requirement of

[2]Because Fig. 1.2 features the valence rather than the conduction band, the charge carriers in this case are holes.

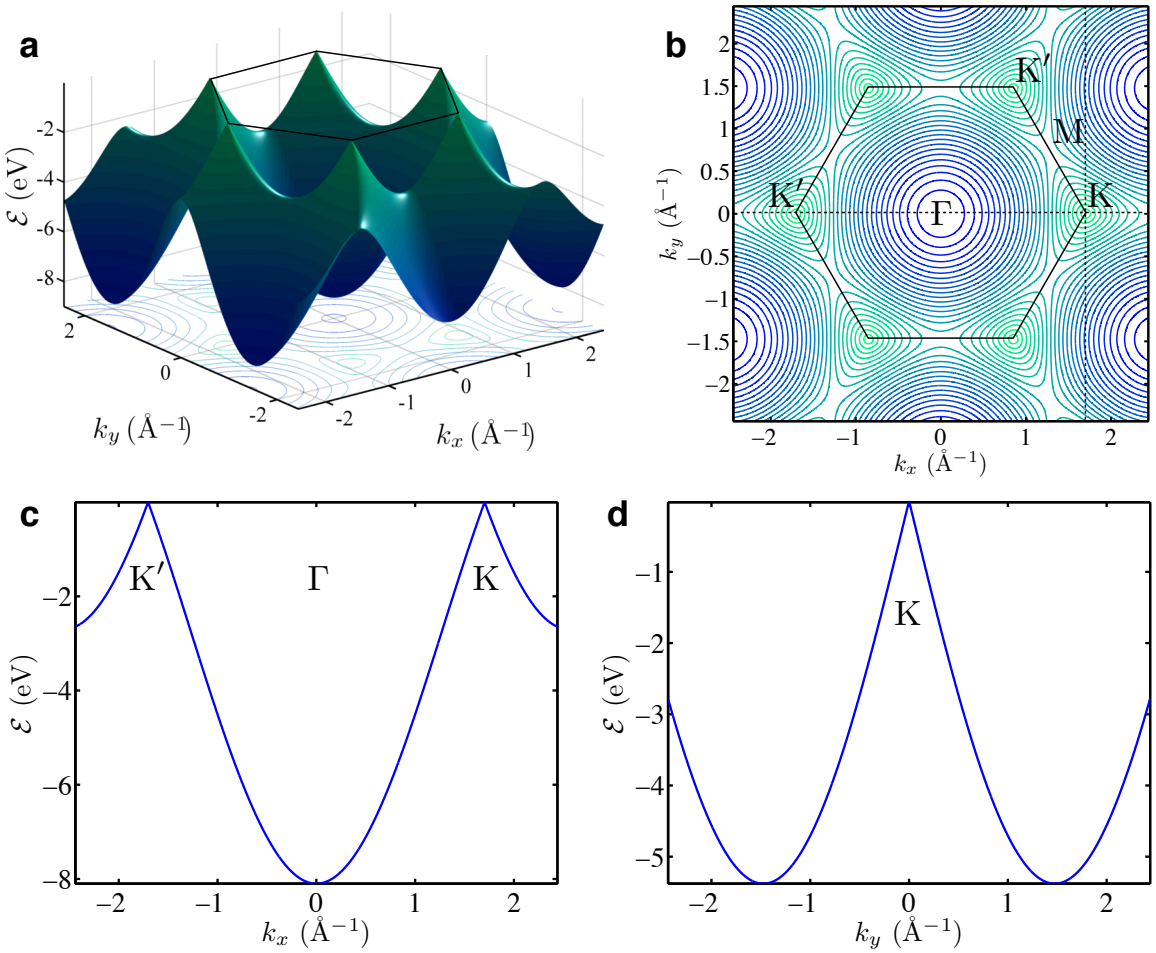

Figure 1.2: Nearest neighbor tight binding approximation of graphene energy band structure. (a) Graphene energy bands $\mathcal{E}$ vs. momentum k according to Eq. 1.1 with $t = 2.7\,\text{eV}$ for $\mathcal{E} \leq 0$. In this ideal case, the graphene sheet is undoped, so the Fermi energy is at $\mathcal{E}_F = 0\,\text{eV}$. (b) Corresponding contour plot. The hexagonal graphene Brillouin zone is marked, along with the locations of the Γ, K, M, and K′ points in momentum-space. (c) Cross-section along the horizontal dashed line in (b) through K′, Γ, and K. (d) Cross-section along the vertical dashed line in (b) through the K-point.

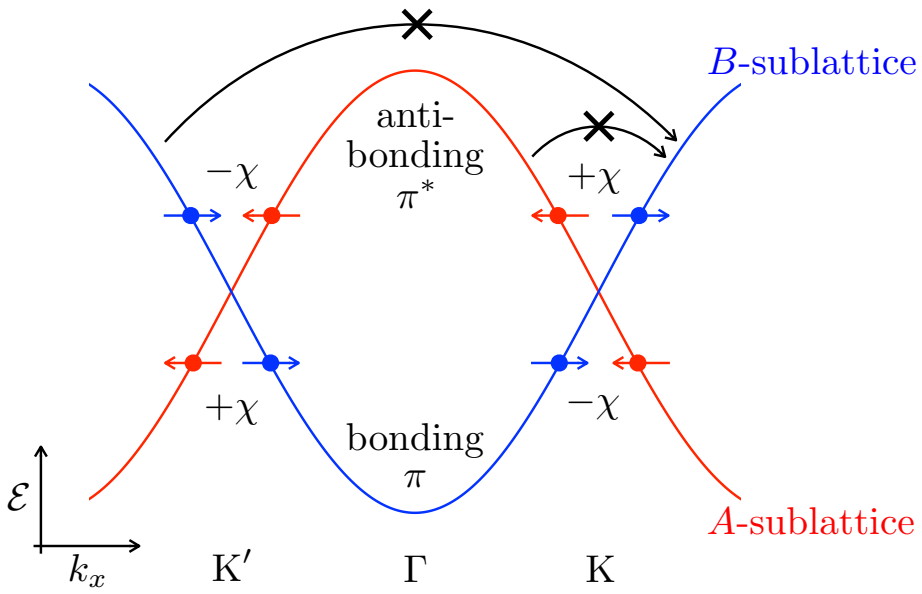

Figure 1.3: The unique electronic properties of graphene arise from its unusual symmetry. This illustration, taken along the horizontal line in Fig. 1.2b shows the conical electronic "valleys" at K and K′. Red and blue arrows indicate sublattice molecular orbital/pseudospin, and χ is chirality. Backscattering and intervalley scattering, depicted as black arrows, are generally prohibited, enhancing conductivity.

spin and momentum in neutrino physics, where this property is called *chirality*, and the term is co-opted here. Chirality on the K and K' cones, also known as *valleys*, is depicted in Fig. 1.3, where chirality χ is the projection of pseudospin, indicated as red or blue vectors corresponding to sublattice, on momentum $k \equiv k_x - K$ or $k_x - K'$. It is clear that the K and K' valleys are inequivalent, as chirality for holes (lower cone) and electrons (upper cone) on each valley differs.

Conservation of pseudospin (orthogonality of sublattices) excludes intra-valley scattering, commonly referred to as backscattering. That is, a reversal of momentum would require a reversal of pseudospin (transfer to opposite sublattice), and is generally disallowed. This is true even in the case of long-range perturbing potentials, such as those due to substrate or dielectric charges, as they affect both pseudospins (sublattices) uniformly and cannot effect a transfer from one to the other. This means that conductivity is amplified, even in imperfect samples, and is a principle basis for

observation of large carrier mobility (even *ballistic*, or zero resistance, mobility over μm-scale distances) in carbon nanotubes and graphene. Short-range potentials, however, if present, can affect pseudospin (couple sublattices) and induce backscattering.

Inter-valley scattering (upper arrow in Fig. 1.3), because it requires a large change in momentum, is ruled out in the absence of atomically sharp potentials/defects. Edge scatterers in narrow graphene wires/ribbons could cause this. The comparison to neutrinos, which are described by the relativistic Dirac equation, as opposed to the non-relativistic Schrödinger equation, leads to use of the monikers *Dirac cone* and *Dirac point* to describe the K and K' cones (valleys) and associated charge neutrality points.

In general, this mobility enhancement could be diminished by dephasing of carriers due to *electron-phonon* or *electron-electron* interactions. The former have been found theoretically and experimentally to be weak in graphene, but the latter can be a consideration, particularly as carrier density increases (that is, as the energy level moves up or down the cone, away from the neutrality point). The largest mobilities have been observed near the neutrality point.[75, 10, 22]

Molecular stability (imparted by C–C sigma bonds) down to atomic dimensions and the possiblity of ballistic conduction make graphene an extremely interesting candidate material to succeed silicon in the microelectronics industry.

1.2 History

Graphene as a material has been around for many decades, having first been produced on metals and carbides, and by oxidation-reduction of graphite. Oxidation was known as early as 1840 to expand graphite, resulting in extremely thin graphitic films, and this was quantified, as far as technically possible, by Hanns-Peter Boehm and coworkers in 1961. Boehm concluded, through multiple techniques, that his graphene films, reduced by hydrazine, were very thin, possibly including monolayer graphene flakes.[8]

This conclusion has since been thoroughly verified. Boehm wrote the formal definition of the term 'graphene' in 1994.[7] Preparation of single-layer graphene on silicon carbide (SiC) was reported by A.J. van Bommel *et al.* in 1975,[96] and preparation on various other substrates, notably including nickel, iridium, rhenium, platinum, and various carbides, was pursued in the following decades. While in-plane bonding is strong, graphene notoriously interacts with adjacent materials only via weak van der Waals forces (consider the operating principle of pencils). This was observed explicitly by Forbeaux and coworkers in 1998, noting that "the first graphene sheet [on SiC] may proceed on top of adatoms ... which reduce the chemical reactivity of the substrate. This layer-by-layer growth opens up the possibility to isolate a single graphene sheet 'floating' above the substrate."[26]

1.2.1 Carbon nanotubes

In the 1990s, there was much excitement around carbon nanotubes, which are essentially graphene sheets, cut and rolled-up (though this is certainly not how they are produced in practice), which share many properties with graphene, with modification due to the precise way in which they are cut/rolled. Certain configurations become semi-conducting, while others retain the metallic nature described above. This was elaborated by theoretical and experimental study of carbon nanotubes produced by chemical vapor deposition, laser ablation, and other techniques, and prototypic devices were produced with indeed promising qualities. Difficulty in selection (semiconducting versus metallic), placement, and organization of nanotubes, however, has plagued nanotube research, and this frustration led to increasing interest in production of graphene.

1.2.2 Electrical measurement of graphene

Electrical measurements of graphene, however, proved elusive until 2004, when researchers from the Georgia Institute of Technology and the University of Manchester

Table 1.1: Observation of expected graphene properties.

	Exfoliated graphene		**Epitaxial graphene on SiC**	
Expected property	**SiO_2**	**Suspended**	**Si-face**	**C-face**
Half-integer quantum Hall effect	[72, 110]	[10, 22]	[82, 46]	[108]
Fractional quantum Hall effect	—	[10, 22]	—	—
Berry's phase of π	[72, 110]	[10]	[82, 46]	[5, 108, 65]
Landau levels $\mathcal{E} \propto \sqrt{B}$	[44]	—	—	[78, 79, 75, 65]
Room temp. mobility $\mu > 10^6\,\mathrm{cm}^2/(\mathrm{V}\cdot\mathrm{s})$	—	[9]	—	[75]
Carrier density $n < 10^{10}\,\mathrm{cm}^{-2}$	—	[10, 22]	—	[75]
Weak anti-localization	[94]	—	—	[108]
Linear band structure	—	—	—	[86]

independently reported electronic measurement of thin graphitic films, obtained via disparate techniques. Subsequent exploration of these samples resulted in conclusive demonstration of expected graphene properties, including those summarized (non-exhaustively) in Table 1.1.

The Manchester group obtained graphene by exfoliation (peeling) of bulk graphite using adhesive tape and gentle deposition on an oxide-coated silicon wafer. Because the oxide thickness was just right, the researchers were able to locate single-layer graphene flakes by optical microscope, and the underlying silicon wafer afforded a built-in back gate for electrical measurement. The investigators claimed at the time that so-called "isolated" graphene had previously been "presumed not to exist" because it was "unstable with respect to the formation of curved structures such as soot, fullerenes, and nanotubes."[73] Later, it was claimed that the Mermin-Wagner theorem had justified the presumption,[72, 29] but, previous observations aside, a simple calculation shows that such "presumed" applicability of the theorem would have been mistaken by 36 orders of magnitude.[93] The ease and accessibility of the exfoliation technique has proven popular among academics, but it has been acknowledged from

the beginning that the decades-old epitaxial growth method was the only feasible avenue for technological applications.[29]

The Atlanta group elaborated the epitaxial graphene growth by thermal decomposition of silicon carbide initiated by van Bommel, Forbeaux, and company in their surface science characterizations through careful control of growth conditions and application of top-down lithography techniques to pattern epitaxial graphene on its inherent substrate, SiC. In comparison to other growth substrates, SiC is attractive because, as a wide-bandgap semiconductor, it is compatible with room temperature electrical operation of graphene devices. In addition to technological viability, which attracted the interest of Intel, Inc. and industry consortia, epitaxial growth ensures a flat, clean graphene film with uniform carrier density and is susceptible to large area measurements that $\sim 10\,\mu$m-scale exfoliated flakes preclude. The flatness, cleanliness, and uniformity of the epitaxial material is key in successful observation of such signatures of high-quality graphene as well-defined energy bands by angle-resolved photoemission [see Chapter 4], improved Raman lines, and well-defined Landau orbits in infrared Landau spectroscopy. Refinement of growth techniques [see Chapter 2] and device fabrication methods [see Chapter 6] is challenging, but encouraging data continue to drive sustained research efforts by academic and industrial researchers.

Chemical vapor deposition (CVD) of graphene on metals, notably including nickel and copper has received intensified attention as well, but this technique requires transfer to a non-metallic substrate for measurement or device fabrication. The crystallinity of graphene produced is furthermore dependent on the crystallinity of the metal catalyst layer.

1.3 Stacking

As the conducting π-orbitals are immediately above and below the graphene sheet, they are sensitive to materials in close proximity. Silicon carbide and, to a lesser

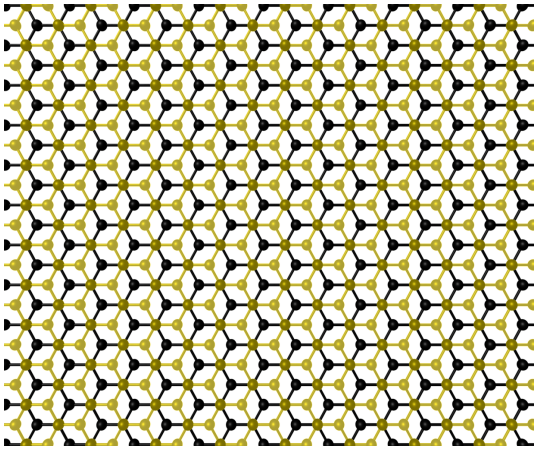

Figure 1.4: In Bernal, or AB-stacking, the two graphene basis atoms are no longer equivalent. This destroys the symmetry from which graphene's interesting properties are derived. In this illustration, the upper Bernal sheet is yellow (slightly transparent), and the lower sheet is black.

extent, silicon dioxide, leave key electronic properties unaltered, but this is not a generality. Interaction of graphene sheets with each other is of interest as it arises in graphite and multi-layer graphene.

Graphite by name has many stacking patterns. The most abundant (∼80%) and lowest energy configuration[32] is Bernal, or AB, stacking, shown in Fig. 1.4. This stacking destroys the graphene symmetry, as the two basis atoms are no longer equivalent—half of the atoms (the A-atoms, by convention) have adjacent atoms immediately above and below, while the nearest atoms vertically to the other half (B-atoms) are two planes away. This is seen predominantly in highly-ordered pyrolytic graphite (HOPG), Kish graphite, and others, which do not display graphene properties such as conical band structure at the K-point or particularly large mobility. The band structure of Bernal stacked graphene is shown in blue in Fig. 1.5.

A new and unique stacking order has been discovered recently in multi-layer epitaxial graphene on the carbon-terminated face of silicon carbide. The sheets are stacked with alternating rotations such that the symmetry of the graphene atoms is

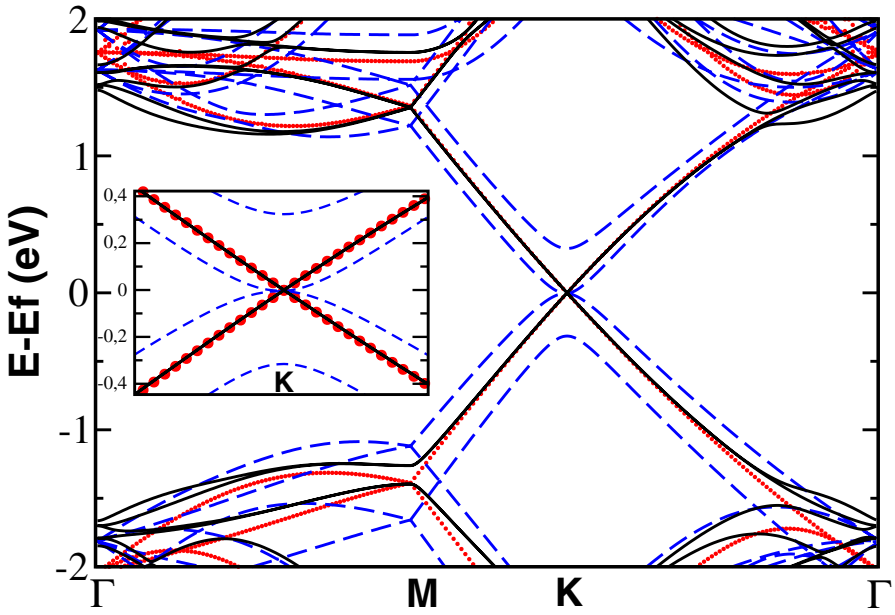

Figure 1.5: *Ab intio* DFT band structure calculation for three forms of graphene: (i) isolated graphene sheet (solid line), (ii) *AB* graphene bilayer (dashed line), and (iii) R30/R2+ fault pair (dots). Inset shows details of band structure at the K-point showing no difference between the Dirac cone for an R30/R2+ fault pair and a single graphene layer. Reproduced from Ref. [37].

preserved for essentially all of the atoms in each sheet. It was not immediately obvious, even given high-quality, well-ordered samples that this would be the case, but it has been confirmed by multiple measurements and subsequently understood with the help of density functional theory (DFT) *ab initio* calculations, as shown in Fig. 1.5. See Section 2.4 and Chapter 4 for further discussion.

1.4 Outline

Epitaxial graphene growth by thermal decomposition of silicon carbide will be discussed in detail in Chapter 2, after which characterization techniques including ellipsometry for determination of thickness and uniformity mapping [Chapter 3], and angle-resolved photoemission for experimental observation of π energy bands [Chapter 4] will be addressed. The important field of graphene chemistry and selective modification of epitaxial graphene properties will be introduced in Chapter 5, and

epitaxial graphene device fabrication, including definition of nanoribbons to obtain semiconducting graphene, will be covered in Chapter 6.

CHAPTER II

GRAPHENE GROWTH BY THERMAL DECOMPOSITION OF SIC

2.1 Atomic force microscopy

As this chapter will include several atomic force microscopy (AFM) images, it is pertinent to begin with a few notes on the capabilities and limitations of the technique. AFM is a scanning probe method that utilizes a sharp probe tip on a cantilever, a reflected laser/photodetecter-based feedback loop, and piezoelectrics to scan the tip across sample topographies. The van der Waals forces that govern the tip-sample interaction give rise to the name *atomic force*. AFM is capable of extremely precise height resolution, $\sim$1 Å, allowing observation of sample height variation with essentially atomic resolution. Lateral resolution, however, is dependent on the dimension of the probe tip, with commonly-used silicon tips having an end radius of $\sim$7 nm. It must be noted when viewing AFM images that the vertical height range is typically amplified by $\sim 1000\times$ in comparison to the lateral scale, as illustrated in Fig. 2.1.

2.2 Experimental considerations

When heated to high temperatures ($\sim 1000-1600$ °C, depending on pressure), silicon preferentially sublimates from SiC, leaving a surplus of carbon on the sample surface. These carbon atoms assume the energetically favorable state that is graphene. This process has been known for many decades, and is similar to processes on other carbides and metals (in which carbon impurities diffuse to the surface), but is not yet fully understood. In particular, graphene production on the two polar faces of hexagonal

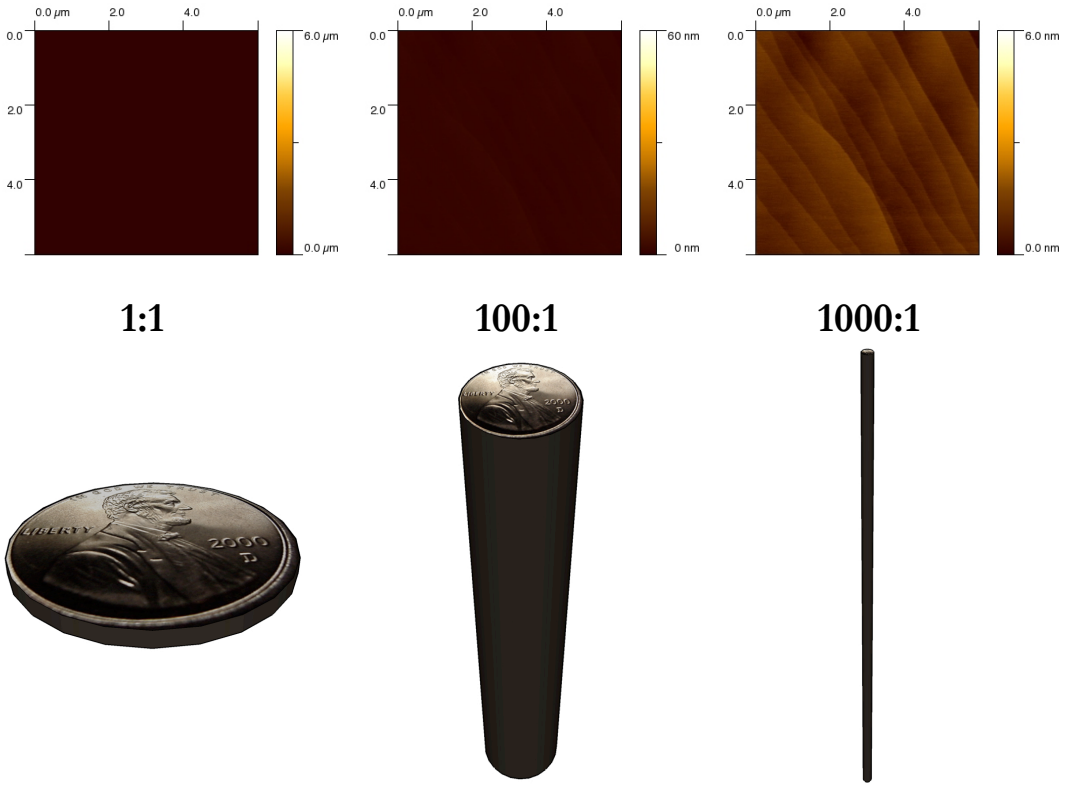

Figure 2.1: Care must be taken in interpretation of atomic force microscope (AFM) images, as the height range is generally greatly amplified relative to the lateral scale. This is illustrated here by comparison to a coin with height amplification matching that in the AFM images, at 1:1, 100:1, and 1000:1, respectively. The surface features are just discernible at 100:1, and entirely lost at 1:1.

SiC, the silicon-terminated (0001) and carbon-terminated ($000\bar{1}$) faces (or Si- and C-faces) proceeds in radically different ways that are not obvious based on the slightly different atomic structures exposed. These will be explored in the following sections, but we will first discuss some universal considerations regarding epitaxial graphene growth that have recently become understood.

2.2.1 Silicon carbide

Silicon carbide has many polytypes, but hexagonal polytypes including $2H$, $4H$, and $6H$ afford a nice epitaxy with graphene. The numbers 2, 4, and 6 refer to the number of Si-C *bilayers* in the polytype unit cell. Each bilayer has height ≈ 2.5 Å, so $4H$-SiC, with four bilayers, has unit cell height ≈ 1 nm, and $6H \approx 1.5$ nm. $6H$-SiC is intuitively attractive because approximately three Si-C bilayers are required to provide carbon for one graphene sheet, but until recently, $6H$-SiC has not been available in non-conductive/"semi-insulating" (as opposed to n- or p-doped conductive) form for room-temperature electrical measurements. In practice, we have found similar results on $4H$- and $6H$-SiC.

Silicon carbide wafers are available nominally on-axis and vicinally miscut (at, for example, 4° or 8°). There are arguments for preferring vicinal surfaces, but the best results published to date have been obtained on on-axis substrates, and this is the clear choice for targeting atomically flat active device regions. The typical unintentional miscut angle on nominally on-axis wafers available from Cree, Inc. is $0.1° - 0.2°$.[18]

3C-SiC, a cubic polytype, is interesting in that it is available as an epitaxial layer on silicon wafers, which could facilitate integration of graphene electronics with silicon CMOS, if graphene of sufficient quality is obtainable on 3C. This may be unlikely because silicon melts at 1414 °C.

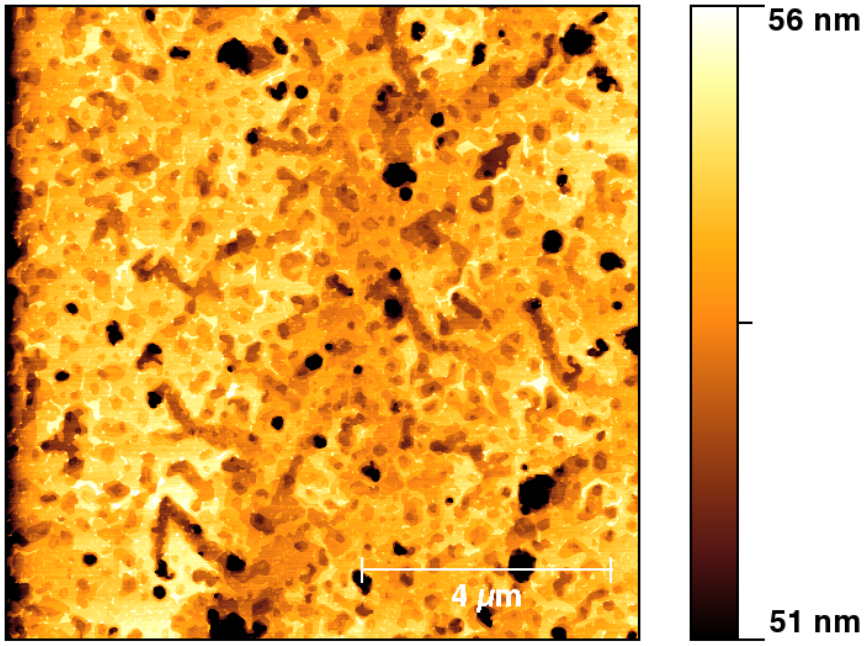

Figure 2.2: Traditional (UHV) growth results in rough topography, as observed on this Si-face 6H-SiC sample, heated by e-beam bombardment (of the back side) to 1350 °C for 4 min. at 10^{-9} Torr.

2.2.2 Growth pressure

The first epitaxial graphene films on SiC were prepared in ultra-high vacuum (UHV, $\lesssim 10^{-9}$ Torr). In the surface science tradition, this was viewed as the best possible condition for clean, defect-free growth, and gave nice low-energy electron diffraction (LEED) patterns[96, 26] and nm-scale scanning tunneling microscopy images, but AFM reveals that topography at the μm-scale is poor, as shown in Fig. 2.2. This is reflected in micro-LEED ($1-2$ μm spot) patterns obtained recently in a low-energy electron microscope (LEEM), as shown in Fig. 2.3.[84] The relatively poor quality of UHV-grown graphene may be understood in terms of silicon flux. When silicon atoms leave the surface in an ultra-high vacuum environment, they are not likely to return, and the process proceeds chaotically, with escaping silicon atoms leaving edges and pits from which subsequent silicon atoms are energetically more likely to sublimate in an escalating process.

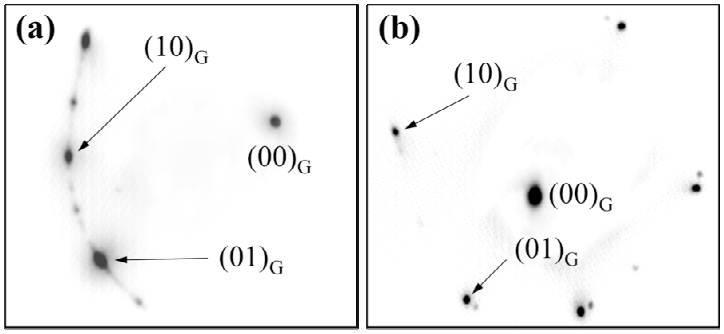

Figure 2.3: LEEM micro-LEED patterns of (a) a $3-4$-layer C-face graphene film prepared in UHV. Only one quadrant of the pattern is shown, but the two primary graphene reflections are labeled for reference. Note the numerous graphene spots and diffuse arcs. (b) 11-layer C-face graphene film prepared in a low-vacuum environment. Only two rotated graphene planes are represented. The images are slightly distorted by aberrations in the LEEM optics.

We have approached[5] this problem by placing samples inside an enclosure with a controlled leak rate that reduces silicon flux by locally increasing partial pressure as depicted in Fig. 2.4. Returning silicon slows the net flux, and with sufficient reduction, the process becomes much more orderly, as shown in Fig. 2.9. This explanation is supported by reports of similar success obtained by back-filling with argon to nearly atmospheric pressure.[24] This, of course, has a similar effect on the silicon flux away from the sample, but cleanliness is only that of the back-filled argon, which is generally not better than 99.999%. A vacuum pressure of 10^{-3} or 10^{-4} Torr inside an enclosure is much cleaner, at one part in $10^6 - 10^7$ of atmosphere. Furthermore, the gas present in the enclosure is likely predominantly silicon (*e.g.* SiO). The induction furnace with internal sample enclosure is shown in Fig. 2.5.

2.2.3 Step flow/surface cleaning stage

A typical temperature-time process curve is shown in Fig. 2.6. Of particular note is the second plateau, which is carried out at a temperature sufficient to evaporate native SiO_2 from the sample surface and induce SiC *step flow* to remove any residual wafer polishing scratches and prepare an atomically flat surface *in situ* immediately

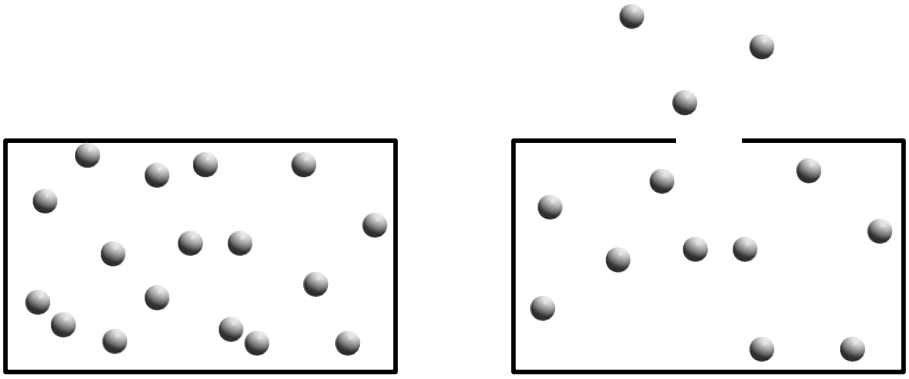

Figure 2.4: Management of local Si partial pressure is key in controlling thermal decomposition of SiC.

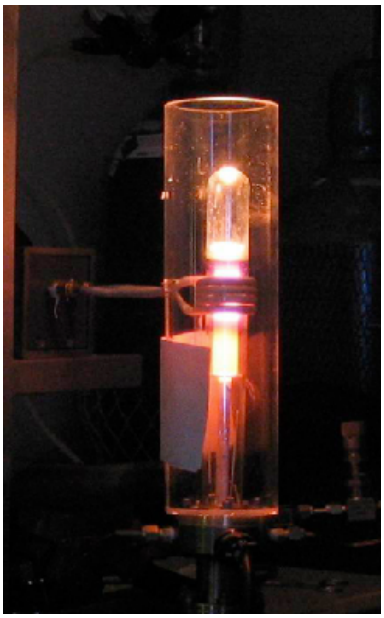

Figure 2.5: Induction furnace with graphite sample enclosure.

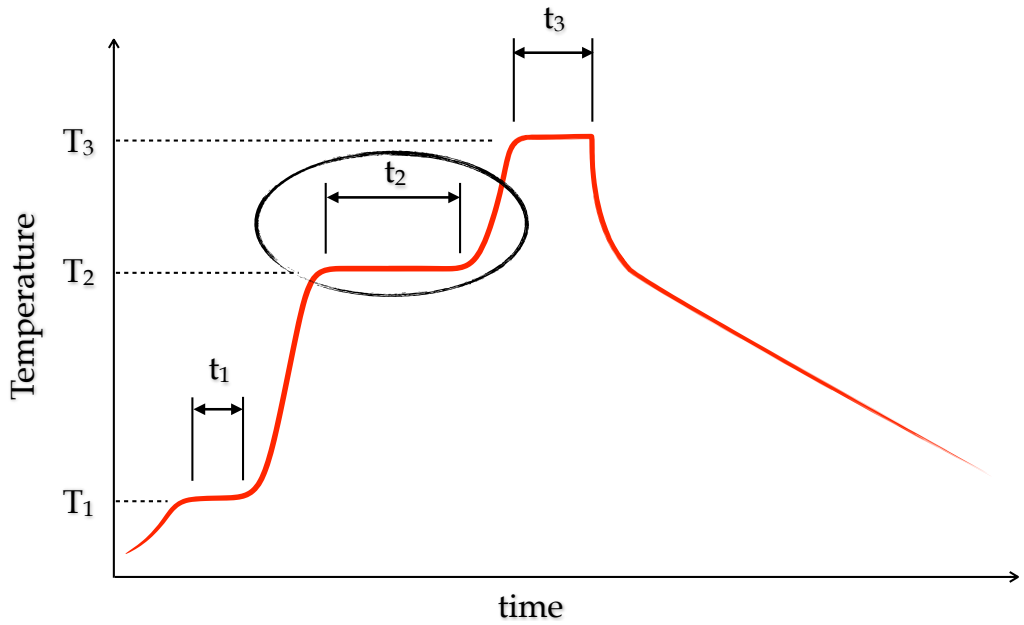

Figure 2.6: Typical graphene growth temperature vs. time. The three plateaus are initial pre-bake, step flow/surface cleaning stage, and graphene growth stage, respectively.

prior to graphene growth. This is particularly efficient when working with chemically-mechanically polished (CMP) SiC wafers, as it likely deprecates the hitherto standard pre-growth SiC surface preparation step of hydrogen etching.[56] It is recommended even in the case of hydrogen-etched SiC for the purpose of oxide removal. In the induction furnace, this step is performed at $\sim$ 1200 °C for $\sim$ 20 min.

The effects of this heating stage are shown in Fig. 2.7 and Fig. 2.8. For demonstration purposes, these non-CMP samples were not hydrogen etched, so the initial surface was polished with $\sim$nm-roughness and residual scratches (from the polishing process). After heating, on the Si-face [Fig. 2.7], atomically flat terraces are obtained with no remaining scratches, while on the C-face [Fig. 2.8], atomically flat steps form, but scratches remain following heating at 1200 °C, and even after heating at 1400 °C, just below the graphene growth temperature. This might be explained by the greater propensity for step-bunching on the Si-face. In the case of CMP wafers, there are no initial scratches, and final results on both faces are indistinguishable (by AFM) from

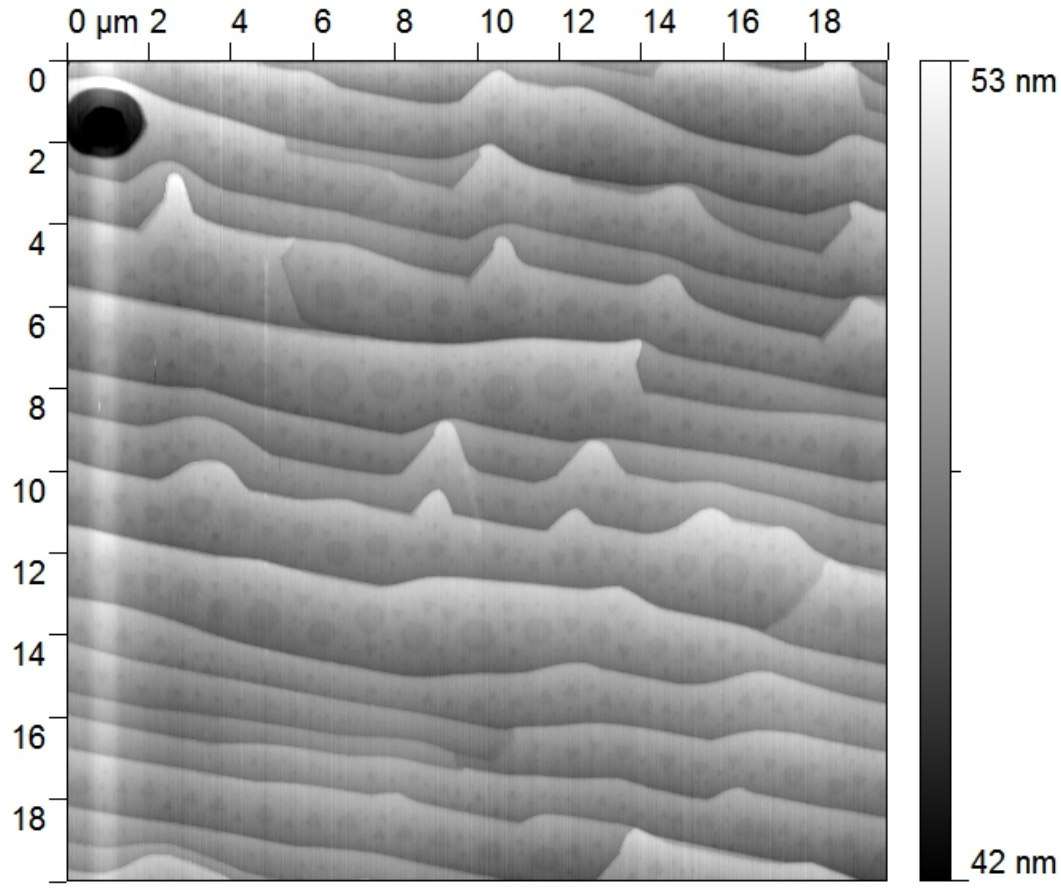

Figure 2.7: Si-face annealed at 1200 °C without H_2 etching. Depression depth is 3.3 Å. No scratches are apparent.

those of hydrogen etching.

The third plateau in Fig. 2.6 is the graphene growth stage. When preparing thin graphene films on the carbon face, this stage has been made to resemble back-to-back Heaviside functions, with rapid heating and cooling for a well-defined ($\sim$ 7 min. at growth temperature) growth period. It is intuitively desirable to use much lower heating and cooling rates for slower, near-equilibrium processes, but this has been difficult to achieve while maintaining thin final graphene thickness.

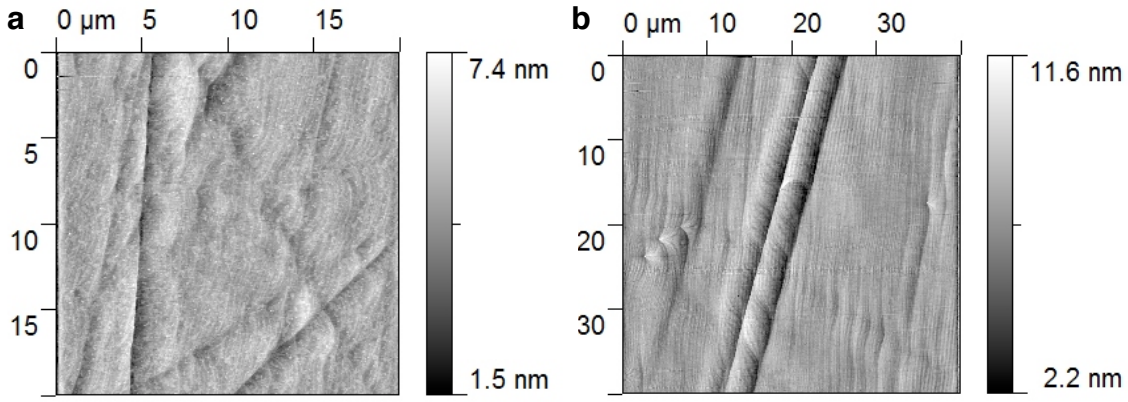

Figure 2.8: C-face sample annealed at (a) 1200 °C and (b) 1400 °C without H_2 etching. Residual scratches are less apparent, but remain just below the graphene growth temperature at 1400 °C. No scratches remain when the surface is chemical-mechanical polished (CMP).

2.2.4 Thermometry

It should be noted that, at temperatures above 1000 °C, care must be taken to avoid large thermal gradients and ensure accurate thermometry, particularly in relatively compact furnaces. Thermocouples should be placed as close as possible to the center of the inductive coil and, of course, the sample location. Thermocouple calibration may be gauged using optical/infrared pyrometry or known melting points (for precise determination of temperatures inside the sample enclosure). Finally, thermocouples used in low-vacuum environments must be replaced regularly.

2.3 Silicon-terminated face

Silicon-face growth is the more studied of the two because it appeared more ordered to the early surface science researchers. The growth proceeds slowly, so it is easy, even in UHV, to prepare thin films and study layer-by-layer growth. For unknown reasons, however, carrier mobility is generally worse than that on the C-face by at least a factor of two, often falling near $\sim 1000\,\mathrm{cm}^2/(\mathrm{V}\cdot\mathrm{s})$. Furthermore, epitaxial graphene films on this face thicker than a couple of layers are not useful, because the sheets stack like graphite (Bernal/AB). Bilayer Bernal-stacked sheets are interesting

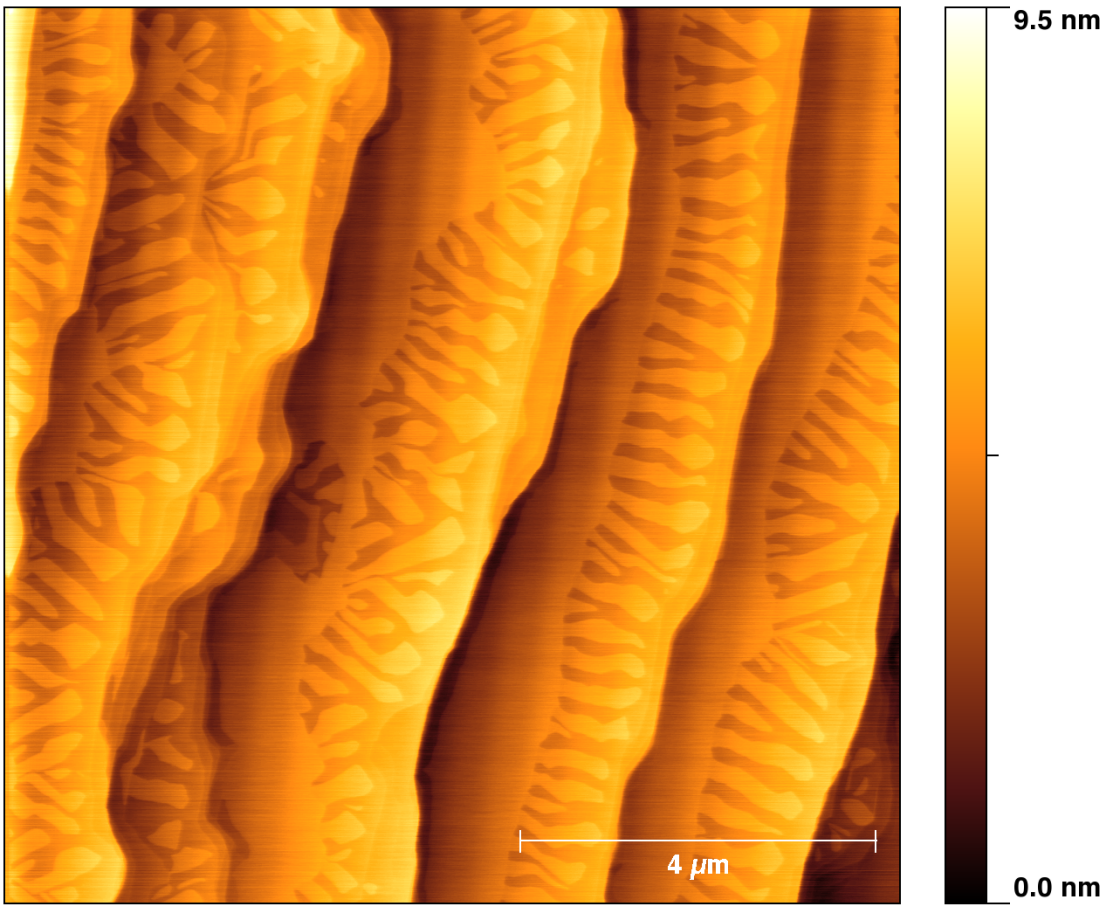

Figure 2.9: Silicon-face growth manifests several interesting features, including SiC step bunching and "fingered" graphene/buffer layer growth.

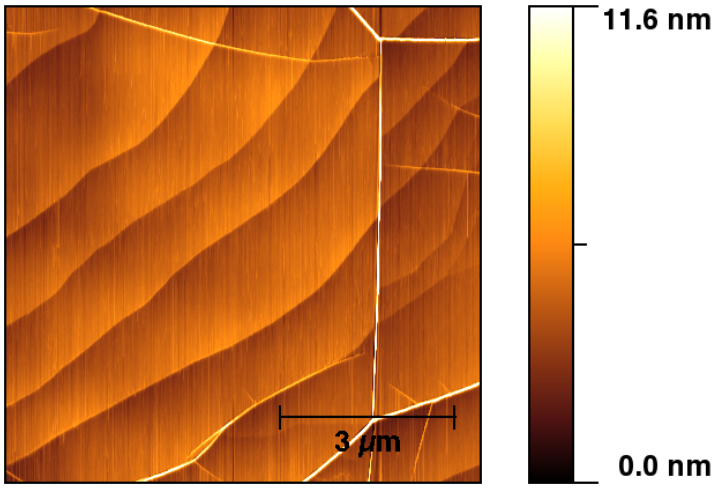

Figure 2.10: Step bunching is generally observed much less frequently on the carbon-face. A typical surface, such as this one, consists of graphene draping unit-cell-height SiC steps with pleats (seen here in white) that are a result of differential contraction of the SiC as the sample cools from the growth temperature.

because, as shown in Fig. 1.5, they retain a linear character, but exhibit a small band gap that could be useful in electronics. Well-controlled Si-face growth, as shown in Fig. 2.9, has been studied theoretically and explained in some detail.[12] Of note are the significant step-bunching and "fingered" buffer/graphene growth.

2.4 Carbon-terminated face: multi-layer epitaxial graphene

Carbon-face growth was believed inferior by early surface scientists because it manifests an unusual rotational stacking, and, coupled with small domain sizes induced by disordered growth and rough sample topography [see Fig. 2.2], early C-face LEED patterns looked more like continuous rings than distinct diffraction patterns. Controlled growth has revealed that, while the rotational stacking remains, it occurs in a *quasi-ordered* way, and is in fact advantageous [see Fig. 1.5] for maintaining graphene properties in a multi-layer film (hence the term *multi-layer epitaxial graphene*).

For unknown reasons, carbon-face growth proceeds inherently much more quickly than on the silicon-face. Still, management of the local silicon environment allows

production of thin graphene films with properties as shown in Fig. 2.10. Underlying silicon carbide steps are generally unit cell-height steps ($\sim$ 1 nm on 4H-SiC) and raised "pleats" are observed in the graphene film. These are understood as resulting from the difference in thermal contraction coefficient between graphene and SiC as the sample cools from $\sim$ 1500 °C. That is, silicon carbide contracts more than graphene, and the difference is absorbed by the pleats. The absence of pleats on the Si-face is understood as a manifestation of stronger graphene-SiC and/or graphene-graphene (Bernal) bonds there. In general, the density of pleats on the carbon-face is proportional to multi-layer graphene thickness.

Further improvements in epitaxial graphene topography are possible by refinements in preparation of the silicon carbide substrate and local silicon environment, as shown in Fig. 2.11, where atomically flat regions on the scale of tens of μm are observed. This is accomplished by further increasing the local silicon partial pressure to slow the graphene growth dramatically to near-equilibrium conditions. Details will be discussed in an upcoming publication.

Infrared magneto-transmission experiments provide detailed information on the nature of carbon-face graphene films. The transmission measurement is primarily sensitive to the bulk of the film, as opposed to electronic transport measurements, which probe the highly-charged layer at the SiC interface. The upper sheets in this $\sim$ 100-layer graphene film are found to be very nearly neutral ($n \sim 10^9 \mathrm{cm}^{-2}$), and, as shown in Fig. 2.12, they support Landau orbits down to a magnetic field of 40 mT, which orbit radius puts a lower limit on the carrier mobility at $250,000\,\mathrm{cm}^2/(\mathrm{V}\cdot\mathrm{s})$. See Chapter 4 for further discussion and characterization of C-face multi-layer graphene.

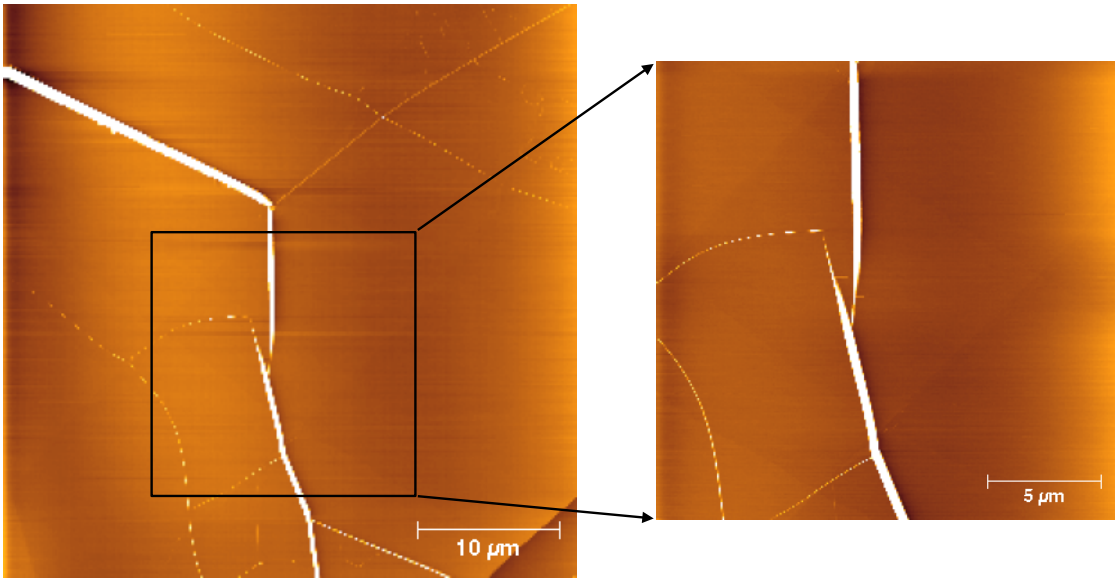

Figure 2.11: Careful management of the local Si partial pressure allows extended flattening of the SiC surface and extremely flat graphene films, as seen in this 40 μm image of a carbon-face sample. Atomically flat regions tens of μm in extent are observed.

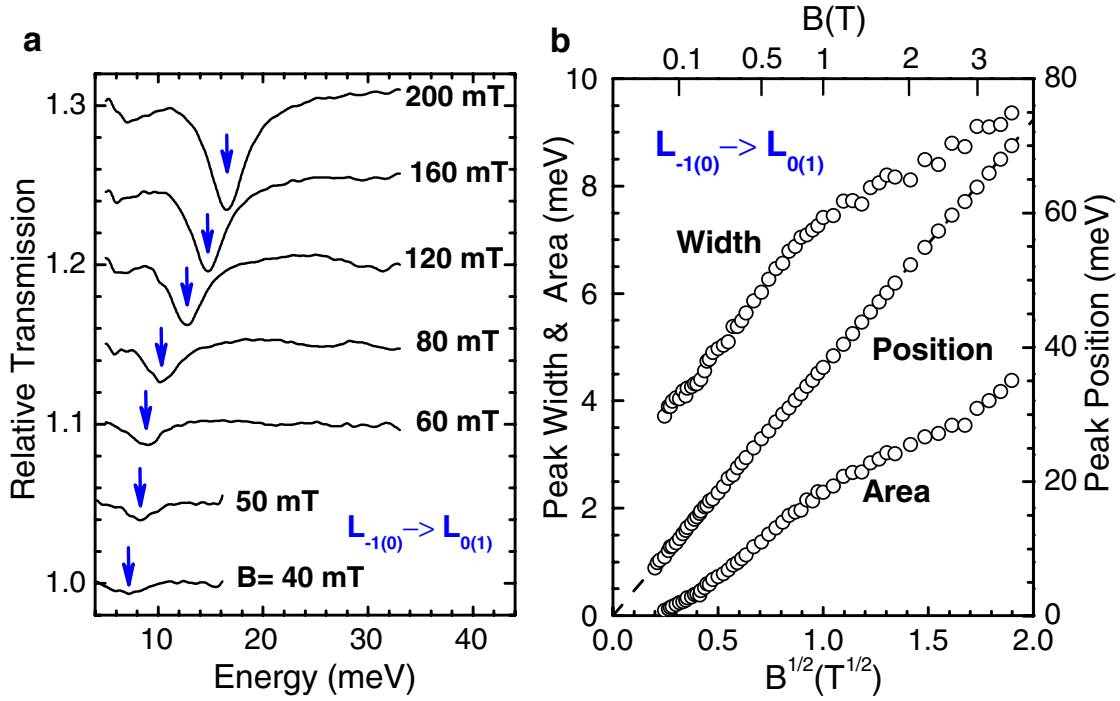

Figure 2.12: Quality of graphene films on carbon-face samples is confirmed by Landau level spectroscopy. Upper layers have carrier density $\sim 10^9\,\mathrm{cm}^{-2}$, and exhibit extremely large mobility at room temperature. (a) Infrared magneto-transmission probing Landau level transitions reveals persistence of Landau orbits at 40 mT. This corresponds to an extremely large orbit radius that places a lower limit on the carrier mobility of $250,000\,\mathrm{cm}^2/(\mathrm{V}\cdot\mathrm{s})$. (b) Absorption peak width, position, and area with field. Reproduced from Ref. [75].

CHAPTER III

THICKNESS DETERMINATION BY ELLIPSOMETRY

Ellipsometry is a powerful high-throughput, non-destructive thin film characterization technique applied widely in science and industry to, among other things, Å-scale determination of film thickness and uniformity. As depicted in Fig. 3.1, it relies on measurement of the change in polarization of incident light upon reflection from a sample surface; knowledge of the optical properties of the thin films and substrate and consideration of the measurement geometry allows highly precise extraction of film thicknesses. Ellipsometric measurement of epitaxial graphene on SiC was performed in 1975, but few details were provided.[63]

3.1 Theory

Reflection of light from a thin film surface is illustrated in Fig. 3.2. The reflection and transmission coefficients at a given interface (say, the $1-2$ interface in the figure) are described by the Fresnel equations,

$$r_{s12} = \left(\frac{E_{1r}}{E_{1i}}\right)_s = \frac{n_1\cos\theta_1 - n_2\cos\theta_2}{n_1\cos\theta_1 + n_2\cos\theta_2} \tag{3.1}$$

$$r_{p12} = \left(\frac{E_{1r}}{E_{1i}}\right)_p = \frac{n_2\cos\theta_1 - n_1\cos\theta_2}{n_1\cos\theta_2 + n_2\cos\theta_1} \tag{3.2}$$

$$t_{s12} = \left(\frac{E_{1t}}{E_{1i}}\right)_s = \frac{2n_1\cos\theta_1}{n_1\cos\theta_1 + n_2\cos\theta_2} \tag{3.3}$$

$$t_{p12} = \left(\frac{E_{1t}}{E_{1i}}\right)_p = \frac{2n_1\cos\theta_1}{n_1\cos\theta_2 + n_2\cos\theta_1} \tag{3.4}$$

where s and p refer to the s- and p-polarizations as shown in Fig. 3.1. The transmission angle θ_2 may be written in terms of the incident angle θ_1 using Snell's law (which is a statement of boundary conditions on Maxwell's equations), $n_1\sin\theta_1 = n_2\sin\theta_2$.

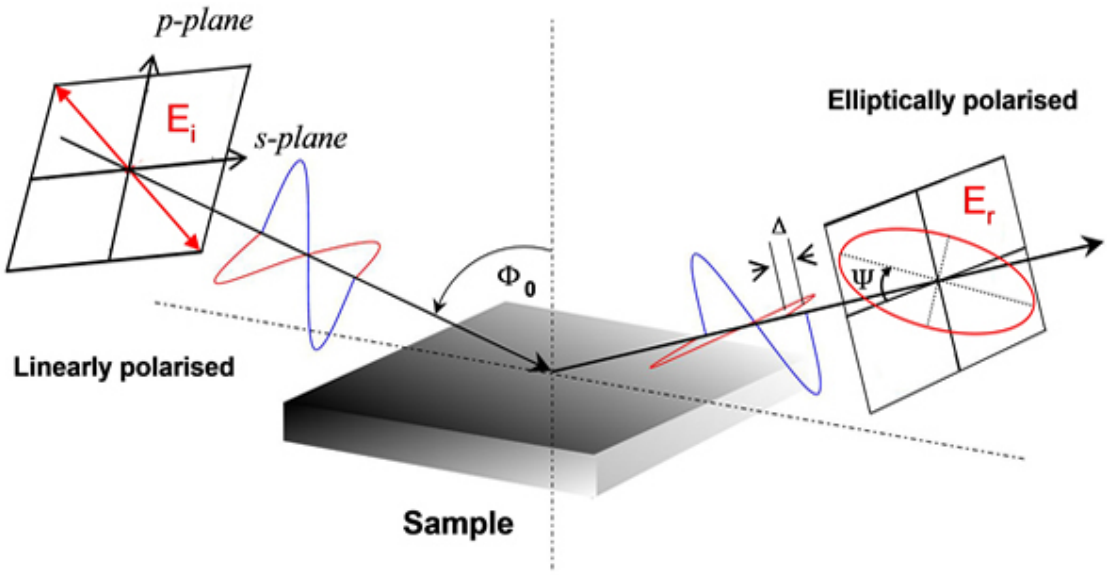

Figure 3.1: Ellipsometry measures the change in polarization of reflected light. Knowledge of the optical constants of the thin films and substrate allow extraction of thin film thicknesses using the Fresnel equations. The polarization state is defined by any one of a number of variable pairs, such as Ψ and Δ, labeled here, or I_s and I_c, as in Fig. 3.6. Reproduced from Ref. [83].

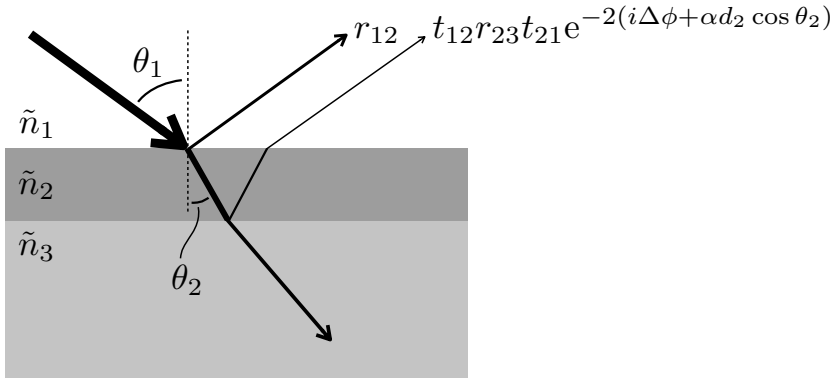

Figure 3.2: Geometrical schematic illustrating reflection coefficients of collected rays (upper right). Thin film thickness is extracted from the reflected s- and p- intensities (polarization).

When the material has a non-zero extinction coefficient κ, the intensity falls off inside the film as

$$I(d) = I_0 \mathrm{e}^{-\alpha d \cos\theta_2}, \tag{3.5}$$

where $\alpha \equiv 4\pi\kappa/\lambda$ (λ is the photon wavelength in air). Finally, the phase angle introduced by passing through a film of thickness d_2 is

$$\Delta\phi = 2\pi \left(\frac{d_2 \cos\theta_2}{\lambda/n_2} \right). \tag{3.6}$$

These coefficients collectively allow calculation of the reflected intensities as shown in Fig. 3.2. Conversely, measurement of the change in polarization allows determination of film parameters such as thickness or optical constants.

Depending on the instrumental setup, polarization is reported in terms of Ψ and Δ, where the change in polarization ρ is given by

$$\rho \equiv \frac{R_p}{R_s} = \tan\Psi \mathrm{e}^{i\Delta}, \tag{3.7}$$

I_s and I_c, where

$$I_s = \sin 2\Psi \sin\Delta \tag{3.8}$$

$$I_c = \sin 2\Psi \cos\Delta, \tag{3.9}$$

or another parameter pair.

3.2 Instrumentation

There are numerous experimental implementations for making ellipsometric measurements. Of note here are design aspects that influence measurement time, localization, and data complexity.

Collection of data at multiple photon wavelengths λ and incidence angles θ_1 allows greater confidence at the cost of measurement time and complexity. The J.A. Woollam Horizontal Variable-Angle Spectroscopic Ellipsometer (H-VASE) varies both, using a light source with a monochrometer to sweep through wavelengths at arbitrary increments, and motorized transmission and collection arms to adjust the incident angle, again at arbitrary increments. This system allows collection of extremely accurate data, but can be very slow, particularly when creating uniformity maps. Because the monochrometer must scan through each measurement wavelength in sequence, dwelling long enough at each point to collect sufficient intensity, spectral scans take minutes and maps take hours.

For much faster measurement and mapping, the J.A. Woollam M-2000 and Horiba Jobin Yvon Auto SE acquire data simultaneously at hundreds of pre-defined wavelengths. That is, there is a lower limit on spectral resolution, but spectral scans are completed in seconds, and maps in minutes. For further simplicity, the Auto SE and many Woollam models operate at a fixed angle, as the spectroscopic data set affords ample confidence. This is particularly true of single-purpose instruments that do not require a large degree of versatility.

The typical inherent measurement spot for most ellipsometers is $\sim 2\,\text{mm}$ in diameter. For more localized measurements, the spot size may be reduced using apertures or lenses. Woollam offers optional lenses for many of its ellipsometers, including the H-VASE, in which case the resulting measurement spot is $200\,\mu\text{m}$ in diameter. While lenses largely maintain intensity, the change in polarization induced by the lenses themselves must be calibrated. This may not be trivial, and alignment of the

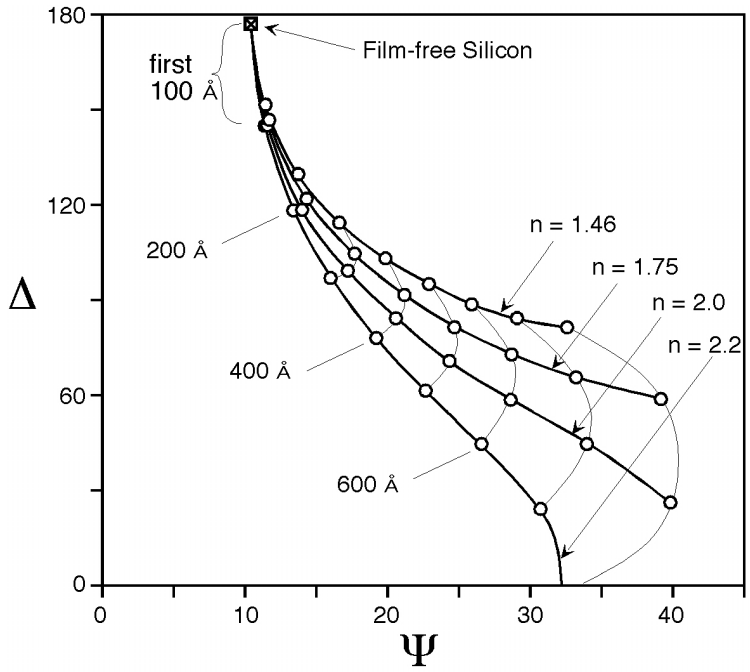

Figure 3.3: When working with extremely thin films (less than 100 Å in thickness), approximate optical constants yield highly accurate thickness values, as illustrated here for the case of thin films having indices of refraction varying from $n = 1.46$ to $n = 2.2$ on a polished silicon substrate. Reproduced from Ref. [95].

lenses can be cumbersome. Horiba's approach on the Auto SE is inclusion of a set of apertures for spots between $25 \times 60\,\mu$m and $500 \times 500\,\mu$m in size. No alignment or calibration is required, but intensity is reduced at the smallest sizes, necessitating somewhat longer collection times.

A motorized stage greatly simplifies uniformity mapping, and a built-in optical microscope is invaluable in positioning relatively small samples. The H-VASE stage is optimized for full wafers and doesn't have the movement resolution required for mapping of relatively small chips, but the Auto SE handles small chips very well.

3.3 Graphene model

Ellipsometric modeling of graphene is greatly simplified because it is an extremely thin film. As illustrated for the case of thin films on silicon in Fig. 3.3, widely varying indices of refraction result in nearly identical change in polarization and film thickness

Figure 3.4: Like calcite (pictured), silicon carbide is uniaxially birefringent. That is, it has two distinct optical directions, each with its respective refractive indices and one axis of anisotropy; light entering the crystal is decomposed into two rays. Reproduced from Ref. [104].

for films much less than 100 Å in thickness. That is, highly accurate thicknesses are obtained with optical constants that are within a reasonable range of the true values. This is not surprising, given that, in this case, the film thickness is much less than $\lambda/50$.

An obvious choice in approximating graphene is the optical constants of graphite. As explained by Jellison *et al.*,[43] accurate determination of the optical properties of graphite has been nontrivial. The uniaxial constants reported by Jellison fit epitaxial graphene data slightly better than those reported elsewhere.

3.4 SiC model: birefringence and backside reflections

There are a number of concerns in accurately representing silicon carbide. First, silicon carbide has many polytypes. The polytypes studied here, $4H$ and $6H$, have slightly different optical properties and must be considered individually. Published tabulations of optical constants and dispersion relations are widely available for these polytypes, and give a good starting point.

Secondly, the doping level (and dopant) of silicon carbide wafers varies from one manufacturer to another and even among nominally identical wafers from one manufacturer. The resistivity currently specified by Cree, Inc., for example, for $6H$ on-axis

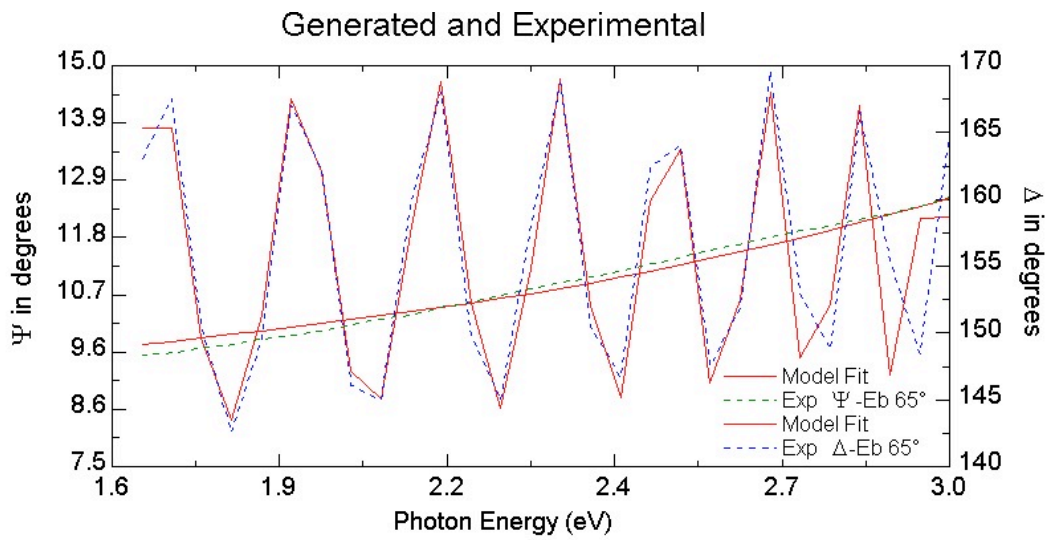

Figure 3.5: If reflections from the back side of the SiC substrate are collected, resulting birefringence oscillations must be modeled, as shown here. Here, graphene thickness is modeled as $33.5 \pm 0.5\,\text{Å}$, $4H$-SiC as $334.5 \pm 0.4\,\mu\text{m}$, with 0.48 ± 0.02 backside reflections. Data taken on J.A. Woollam H-VASE.

n-type wafers is $0.02-0.20\,\Omega$-cm.[18] The doping level has an obvious effect on optical properties, as n-type wafers are shades of green, while semi-insulating wafers are a light gray. For this reason, the silicon carbide model should be customized for the material in use. "Fine tuning" of models for particular materials or deposition/growth techniques is common practice, as ellipsometry is generally sensitive to precise film properties.

Next, transparency of the substrate means that, if the back side of the wafer is polished, as is commonly the case, reflections from the back side are normally collected. Because the substrate thickness is large ($> 500\lambda$), birefringent rays [see Fig. 3.4] reflected from the back side are no longer coherent, and a phase

$$\Delta\phi_B = \frac{2\pi d_3}{\lambda}\left(n_{3e} - n_{3o}\sin\theta_3\right) \approx \frac{2\pi d_3}{\lambda}\Delta n_3 \tag{3.10}$$

is introduced, where d_3 is the SiC thickness, and $\Delta n_3 \equiv n_{3e} - n_{3o}$, the difference of the extraordinary (parallel to c-axis) and ordinary (perp. to c-axis) indices of refraction of silicon carbide, n_{3e} and n_{3o}, respectively. This results in oscillations

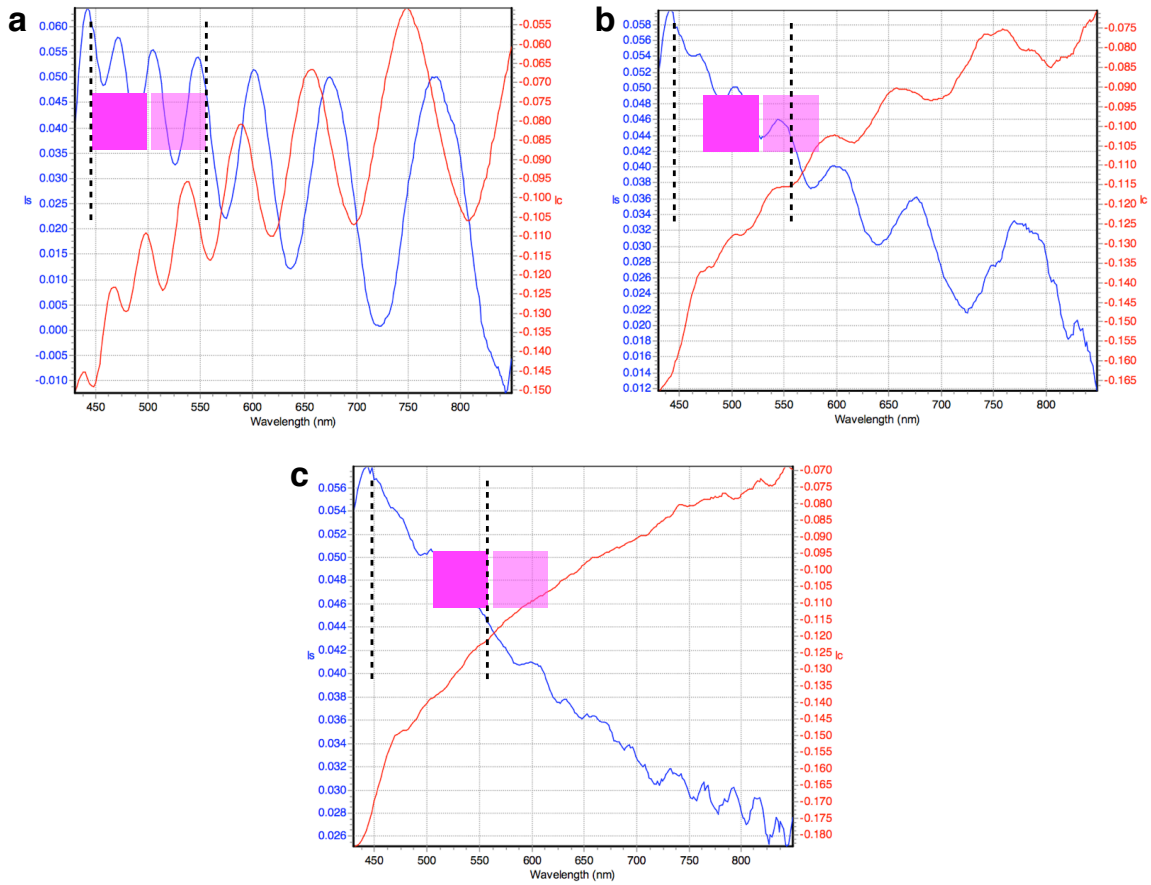

Figure 3.6: Eliminating backside reflections on the HJY Auto SE with $250 \times 250\,\mu$m spot size by adjusting sample height. Insets, upper left: dark and light pink squares represent primary and secondary (backside) reflections, respectively. Black dashed lines mark collection range, as indicated on the instrument. (a) Secondary reflection fully collected. (b) Secondary reflection partially collected. (c) Secondary reflection collection minimized; SiC birefringence oscillations are largely eliminated. This situation is much simpler to model.

with approximate frequency $f \approx d_3 \Delta n_3 / hc$ in the ellipsometric data as a function of photon energy. This can be modeled by taking into account the above and fitting the substrate thickness and number of backside reflections collected, as shown in Fig. 3.5, but a better approach for routine analysis is simplification of the data by using apertures to avoid collection of the backside reflections.

This is demonstrated in Fig. 3.6 with three measurements performed in sequence on the Auto SE. A relatively small spot size, such as 250×250 or $100 \times 100\,\mu$m, should

be chosen so that the incident and backside reflected rays, (visible in the microcope view, depicted here as pink squares) are spatially separated. The sample height can then be adjusted to move the backside-reflected ray out side the collection range as marked by dashed lines here and on the instrument. As shown in Fig. 3.6c, this nearly eliminates the birefringence oscillations. Analysis of the resulting data is much simpler, as backside reflections and two fitting parameters (substrate thickness and number/percent of backside reflections collected) may be removed from the model. In this case, epitaxial graphene thickness is the only free parameter in the fit. Backside reflections may alternatively be eliminated by roughening the back side, or placing it in contact with an index-matching material (such as a liquid), but these are more difficult and often not desirable, particularly when graphene on the back side is also of interest.

Finally, silicon carbide has a band gap and becomes absorbing at $\approx 3.2\,\mathrm{eV}$. The analysis is significantly simpler when studying the spectrum below this value. It is furthermore convenient to use an intuitive dispersion model, such as the Cauchy dispersion, which is valid in the transparent region.

3.5 Thickness uniformity mapping

Ellipsometry is extremely useful for gauging film thickness uniformity over large areas. This is possible on the J.A. Woollam H-VASE using lenses to reduce the spot size to $200\,\mu\mathrm{m}$ in diameter. Fig. 3.7 shows a 15-point map of epitaxial graphene thickness over a $3.5 \times 4.5\,\mathrm{mm}$ SiC$(000\bar{1})$ chip with average 29.3 Å, or 9 layers, and standard deviation 2.7 Å, or 0.8 layers. This is comparable to a value of 31 Å obtained in roughly the same average location with the native 2 mm diameter spot. Because of the inherent limitations of the scanning monochrometer, reduced intensity with the lenses in place, limitations of the stage motion, and alignment considerations, it took seven hours to create this map. A similar map is easily created on the Auto SE in

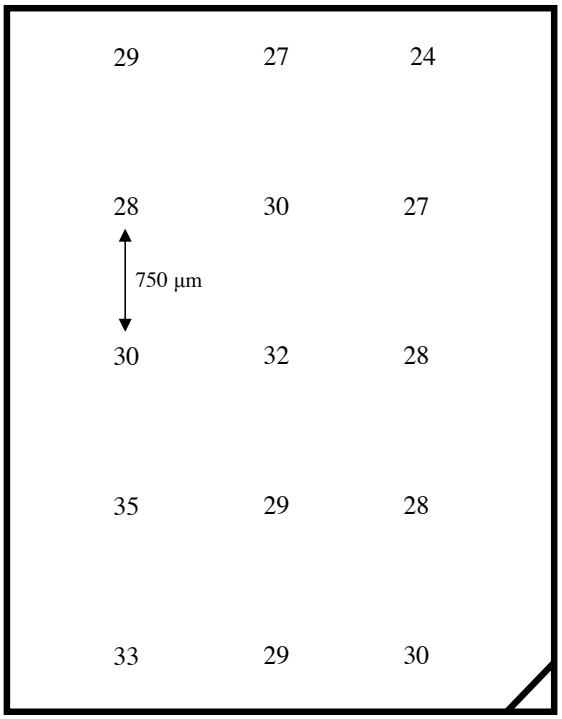

Figure 3.7: On some ellipsometers, such as the J.A. Woollam H-VASE, more localized data may be acquired through use of focusing lenses, which reduce the measurement spot size from 2 mm in diameter to 200 μm. This allows thickness uniformity mapping, as shown here for a $\sim$ 10-layer C-face sample in 2007. Values indicate graphene thickness (in Å) at 15 locations across the 3.5×4.5 mm surface.

about ten minutes, where smaller spot sizes and a fully automated stage with fine position control improve resolution and accelerate measurement dramatically. This has enabled routine ellipsometric thickness mapping as a part of standard epitaxial graphene sample characterization procedures.

3.6 Comparison to other techniques

Like some other techniques, including x-ray photoelectron spectroscopy (XPS) and Auger electron spectroscopy (AES), ellipsometry does overestimate the number of epitaxial graphene layers on SiC by one or two as compared to lower-throughput methods including surface x-ray diffraction (SXRD), angle-resolved photoemission spectroscopy (ARPES), scanning tunneling microscopy (STM) and low-energy electron microscopy (LEEM).[35, 38] Ellipsometry (and XPS, AES) does not distinguish well [see Fig. 3.3] graphene sheets from the carbon-rich buffer layer at the graphene-silicon carbide interface, and therefore includes it in the reported thickness, augmenting the total by one or two layers. Ellipsometry, however, is much higher-throughput than all of these techniques, which require ultra-high vacuum, delicate equipment, and/or a synchrotron. Furthermore, ARPES, STM, XPS, and AES cannot identify thicknesses larger than a few layers,[35] while ellipsometry can measure film thicknesses as large as 1000 layers. Ellipsometry has the distinction of speed while maintaining accuracy.

3.7 Physical trends with thickness

Non-destructive determination of epitaxial graphene thickness allows study of graphene properties by various techniques, including x-ray diffraction, scanning tunneling microscopy, low-energy electron diffraction, angle-resolved photoemission, and infrared magneto-transmission as a function of the number of graphene layers in a multi-layer graphene stack. The latter is shown in Fig. 3.8, where a Landau level transition characteristic of graphene is probed in rotationally-stacked carbon-face epitaxial graphene samples 3, 9, and 60 layers in thickness. The depth of the absorption valley becomes

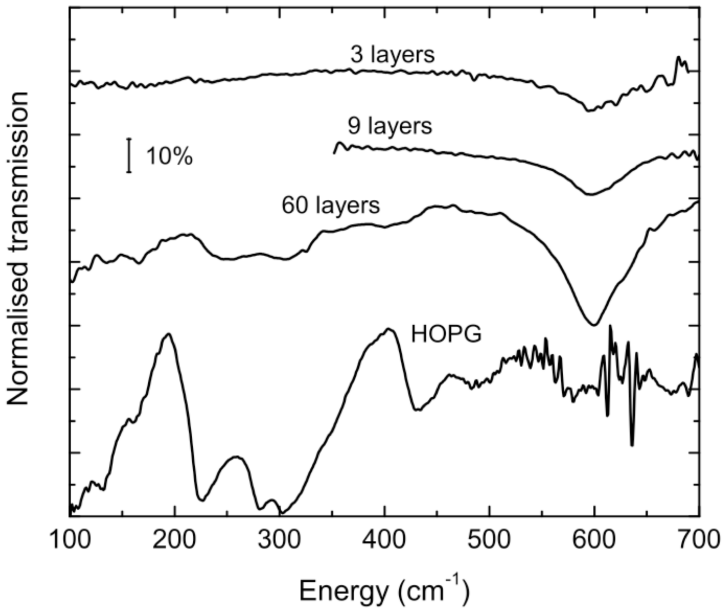

Figure 3.8: Non-destructive determination of graphene thickness allows study of physical trends with thickness. Here, infrared transmission probing Landau level transitions in C-face multi-layer graphene finds retention of graphene properties in even the extreme case of a 60-layer film, in contrast to the spectrum of HOPG (lower curve). This is due to a rotational stacking that decouples the graphene sheets [see Chap. 4]. Reproduced from Ref. [75].

larger as the number of graphene sheets increases, in contrast to the spectrum of highly-oriented pyrolytic graphite (HOPG), which does not exhibit this transition. See Chap. 4 for further measurement of carbon-face epitaxial graphene.

3.8 Outlook

Ellipsometry is a great tool for characterization of epitaxial graphene. In comparison to other techniques, it is extremely high-throughput, but still accurate. It is entirely nondestructive, requiring only brief exposure to visible light, whereas the prolonged x-ray, ultraviolet, or electron beam exposure required by other techniques, coupled with impurities in the atmosphere, can damage graphene. Ellipsometry is a versatile technique capable of extracting much more than thickness information. It may be useful, for example, in characterizing dielectrics on graphene, or studying the graphene-silicon carbide interface.

CHAPTER IV

ANGLE-RESOLVED PHOTOEMISSION ON THE CARBON-FACE

Angle-resolved photoemission and X-ray diffraction experiments show that multilayer epitaxial graphene grown on the SiC($000\bar{1}$) surface is a new form of carbon that is composed of effectively isolated graphene sheets. The unique rotational stacking of these films cause adjacent graphene layers to electronically decouple leading to a set of nearly independent linearly dispersing bands (Dirac cones) at the graphene K-point. Each cone corresponds to an individual macro-scale graphene sheet in a multilayer stack where AB-stacked sheets can be considered as low-density faults.

4.1 Linear dispersion

The most fundamental property of an ideal graphene sheet is the linear dispersion of the π- and π^*-bands, $E(\Delta k) = \hbar v_F \Delta k$, where v_F is the Fermi velocity and Δk is the momentum relative to the K-points of the hexagonal reciprocal unit cell.[102, 61] The linear dispersion defines a cone with an apex at the Dirac point, E_D.[102, 61] For undoped graphene, the Fermi energy, E_F, equals E_D, so the Fermi surface consists of six points [see Fig. 4.1]. This unique dispersion is one of two fundamental properties that motivate an all-graphene electronics paradigm.[4]

Despite its centrality to graphene physics, the unperturbed linear dispersion near E_D has not been directly observed. Exfoliated graphene flakes on SiO_2 have proven imperfect subjects in the study of Dirac-point physics because impurity-induced film disorder and mechanical deformation due to substrate interactions cause large position-dependent charge fluctuations ($> 10^{11}\,\mathrm{cm}^{-2}$), indicating that the Dirac cones

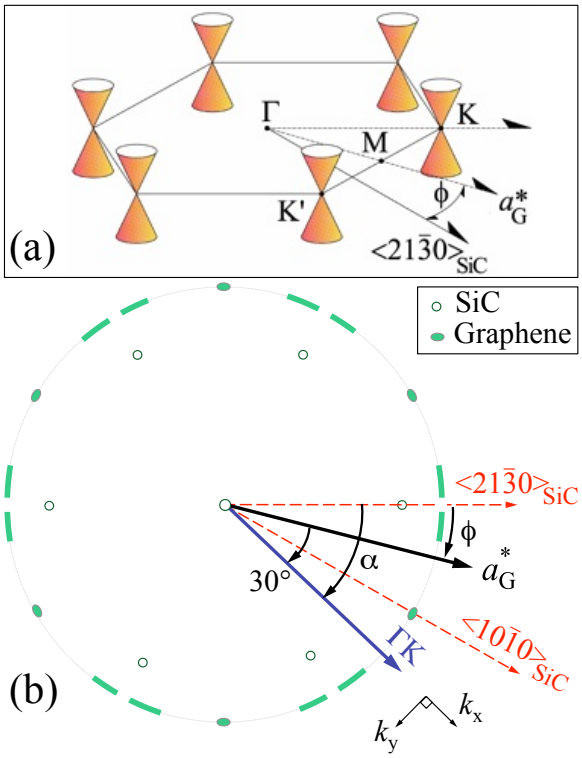

Figure 4.1: (a) 2D Brillouin zone of graphene near E_F showing the six Dirac cones at the K-points. The cones are shown rotated through an angle ϕ relative to the SiC $\langle 21\bar{3}0\rangle$ direction. (b) A schematic diffraction pattern of graphene grown on SiC$(000\bar{1})$. The SiC diffraction pattern ($\circ$) and the graphene pattern ($\bullet$) from a $\phi = 30°$ rotated film are shown. Diffuse graphene arcs seen on C-face graphene are shown rotated $\phi \sim 0°$ from the $\langle 21\bar{3}0\rangle$ direction.

are poorly defined for energies less than 0.3 eV from E_D.[60] In fact, disorder-induced broadening in these samples makes the Dirac cone and point essentially unresolvable in angle-resolved photoemission spectroscopy (ARPES) experiments.[49] The influence of the substrate has been somewhat reduced by suspending deposited films over microscopic holes,[21] but these remain susceptible to spontaneous rippling and strain.[64]

4.2 ARPES on the silicon-face

In contrast, epitaxial graphene (EG) grown directly on the SiC(0001) Si-face and SiC(000$\bar{1}$) C-face have exceptional film quality. This, coupled with scalability to integrated circuits, makes EG a serious candidate material for realization of graphene electronics.[35, 24] While disorder-induced band-broadening is not observed in EG, substrate interactions, as with exfoliated graphene, do play a role. Substrate interactions with Si-face graphene are known to distort the linear dispersion near E_D in the first graphene layer, causing a $\sim$ 200 meV band gap, up to $\sim$ 500 meV electron-doping, and enhanced electron-phonon coupling.[112, 74, 13] Furthermore, the graphitic *AB*-stacking of Si-face graphene causes the band structure of these films to converge to that of graphite as film thickness increases.[74]

4.3 Rotational stacking on the carbon-face

Of all the experimental forms of graphene, including single exfoliated sheets, multilayer epitaxial graphene (MEG) grown on the C-face of SiC shows the essential signatures of an isolated graphene sheet most completely [see Table 1.1]: Berry's phase of π, weak anti-localization, square-root dependence of Landau level energies with applied magnetic field,[5, 78, 79, 107, 19, 75, 65] a zero landau level,[65] and, as presented in this work, unperturbed linear band dispersion.

I present direct measurements of the linear band structure of MEG, explicitly

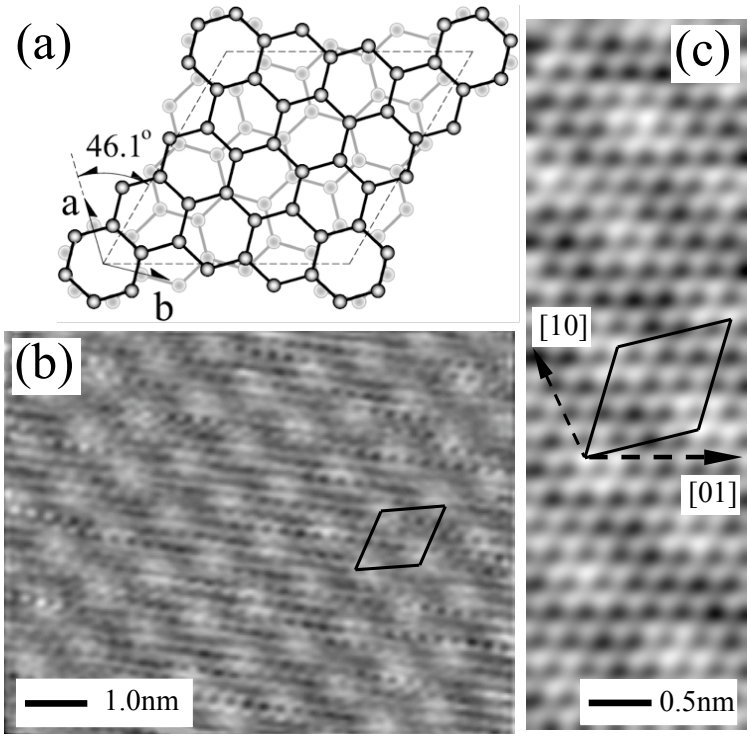

Figure 4.2: STM observation of rotational stacking on the carbon-face. Reproduced from Ref. [37].

demonstrating that it is *not* graphite, but rather a new material consisting of essentially decoupled graphene layers.[86, 87, 84] I show that these films have long electron relaxation times and a remarkable absence of electron-phonon coupling or other distortions of the Dirac cone. These measurements demonstrate that a new periodic rotational stacking (*not* the 60° associated with graphite—see Fig. 4.2) is responsible for MEG's exquisite 2D properties. These results support the theoretical explanation of preservation of linear bands in rotationally stacked films.[20, 53, 37]

Substrates used in these studies were nominally on-axis n-doped $n \approx 2\times10^{18}\,\mathrm{cm}^{-2}$ $6H$- and insulating $4H$-SiC from Cree, Inc.[18] Substrates were prepared by H_2 treatments and subsequent graphene growth was carried out in a closed RF induction furnace [see Chap. 2 for details]. The graphene films used in this study ranged from $11-12$ layers as estimated by ellipsometry [see Chap. 3]. Samples were transported in air and thermally annealed at $800-1100$ °C in UHV prior to measurement. It

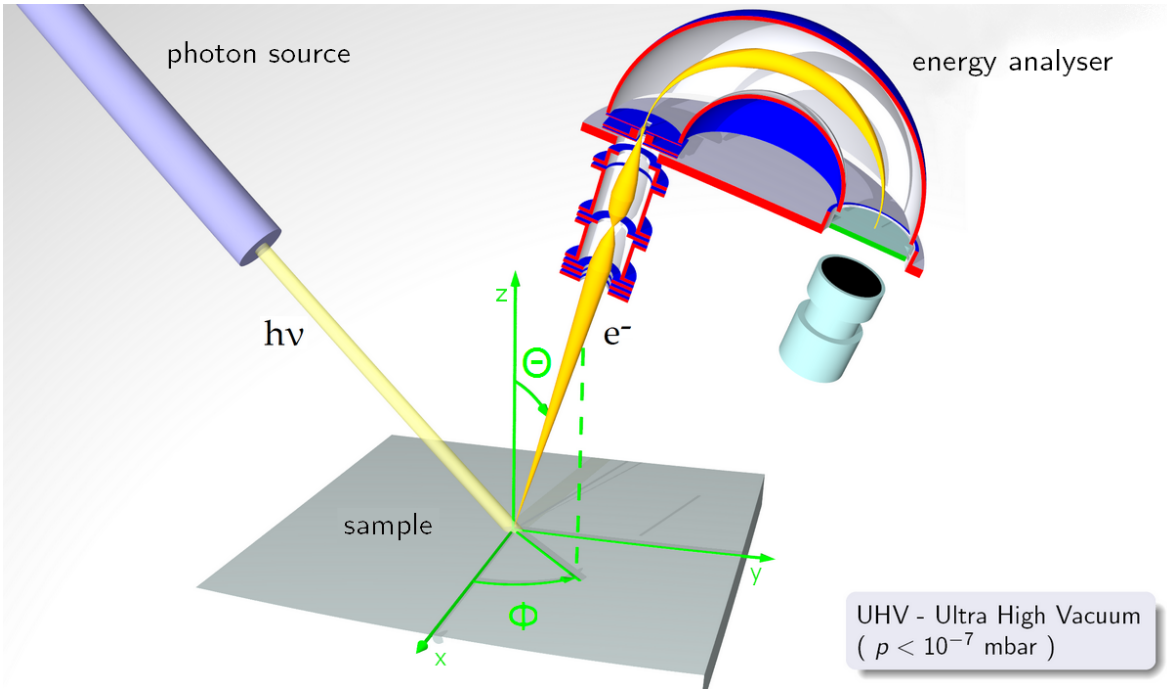

Figure 4.3: Angle-resolved photoemission spectroscopy (ARPES) is a photon-in, electron-out technique. Knowledge of the energy $h\nu$ of incoming photons and measurement of the momentum vector **k** of outgoing electrons allows mapping of sample band structures such as that illustrated in Fig. 1.2. Momentum is generally recorded in terms of angles, such as Θ and Φ indicated here. Reproduced from Ref. [103].

should be noted that furnace-grown samples have graphene domain sizes much larger than 20 μm, more than 100 times larger than those typical of graphene grown in UHV.[40, 35]

4.4 ARPES: nearly ideal linear bands

ARPES is a photon-in, electron-out technique that allows probing of a material's electronic structure, as illustrated in Fig. 4.3. Modern synchrotrons provide energetic, high-intensity photon beams for rapid measurements over a large energy range. ARPES measurements were made on different samples at both the Cassiopée beamline at the SOLEIL synchrotron in Gif sur Yvette and at the 12.0.1 beamline at the Advanced Light Source (ALS) at Lawrence Berkeley National Lab. The high-resolution Cassiopée beamline is equipped with a modified Peterson PGM monochromator with

a resolution $E/\Delta E \simeq 70,000$ at 100 eV and 25,000 for lower energies. The detector is a $\pm 15^\circ$ acceptance Scienta R4000 detector with resolution $\Delta E < 1$ meV and $\Delta k \sim 0.01\,\text{Å}^{-1}$ at $\hbar\omega = 30$ eV. Sample temperatures were varied from 6 K to 300 K. The surface x-ray diffraction (SXRD) experiments were performed at the Advanced Photon Source, Argonne National Laboratory, on the 6IDB-μCAT UHV beam line with $\hbar\omega = 16.2$ keV.

The primary result of this work is shown in Fig. 4.4a, where I display the band structure of an 11-layer graphene film grown on the C-face of 6H-SiC. Data is taken near the K-point ($k_{\Gamma K} = 1.704\,\text{Å}^{-1}$, $k_z \sim 0.02c^*$, where $c^* = 2\pi/6.674\,\text{Å} = 0.941\,\text{Å}^{-1}$) and not at the H-point of graphite ($k_z \sim 0.5c^*$). The figure shows two bright and one faint intersecting Dirac cones; the faint cone is more easily visible in the momentum dispersion curve (MDC) in Fig. 4.4b. A corresponding Fermi surface at $E = -225$ meV is shown in Fig. 4.5. The Dirac cones in Fig. 4.4a represent the first measurement of unperturbed π-bands as expected of an isolated graphene sheet. Band maps on various samples and locations show similar results: multiple rotated linearly-dispersing Dirac cones. Within experimental uncertainty (~ 20 meV), there is no evidence of a band gap. Because ARPES is sensitive to only the $3-4$ surface layers at this energy (as governed by the electron escape depth), there is no influence on the bands from the graphene-SiC interface. This leaves the observed graphene sheets nearly charge neutral, with the absolute difference between the Dirac point and Fermi energies being < 20 meV. This puts an upper limit on the doping level at $n < 10^{10}$ cm^{-2}, consistent with infrared magneto-transmission measurements of $n \sim 5 \times 10^9$ cm^{-2} in similar films.[75]

Two points must be stressed. First, these films are *not* graphitic. The *AB*-stacking of graphite would show parabolic bands[113] or the splitting seen in bilayer or multilayer graphene films grown on the Si-face.[112, 74] In fact, *AB*-planes are so few in C-face MEG films that they may be considered as stacking faults. The second point

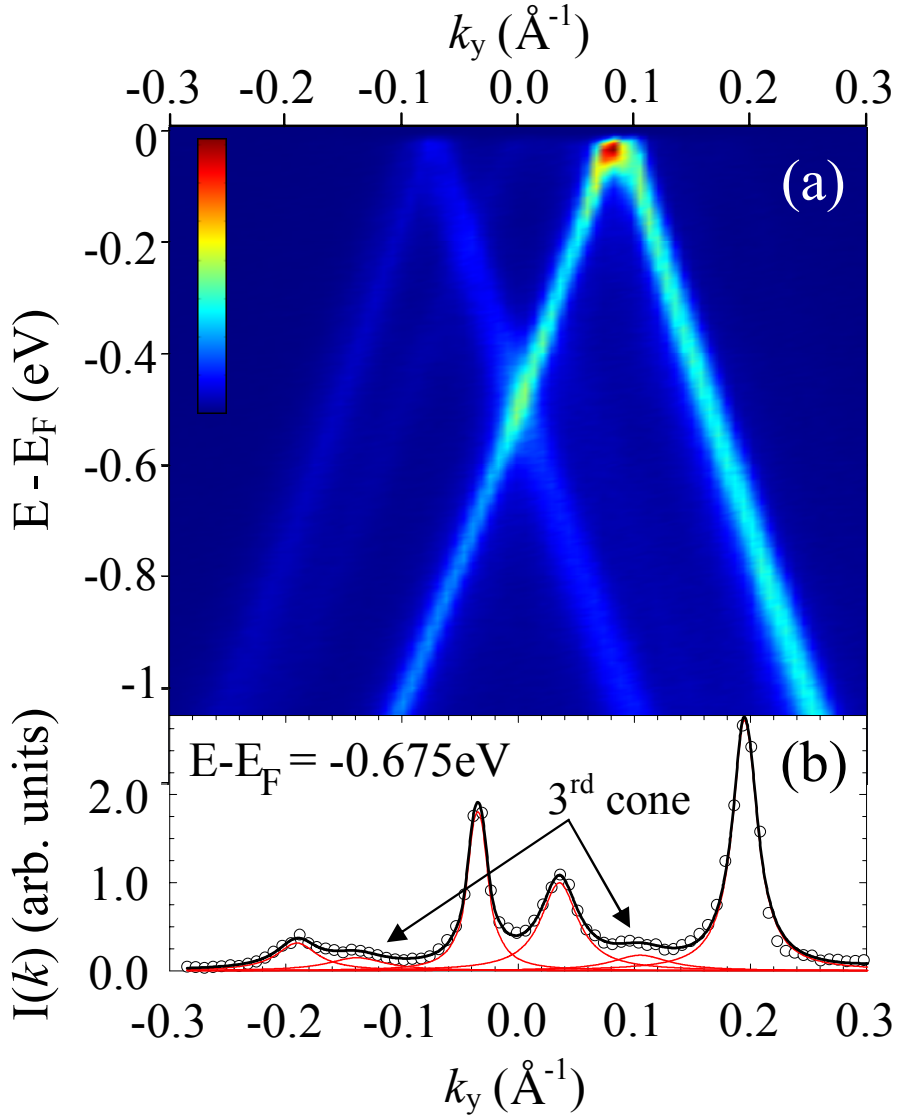

Figure 4.4: (a) ARPES measured band structure of an 11-layer C-face graphene film grown on the 6H-SiC. The sample temperature is 6K. The scan is perpendicular to the SiC $\langle 10\bar{1}0\rangle_{\mathrm{SiC}}$ direction at the K-point [See Fig. 4.1]. Three linear Dirac cones (one faint) are shown. (b) An MDC at $BE = E_F - 0.675$eV shows all three cones. Heavy solid line is a fit to the sum of six Lorentzians (thin solid lines).

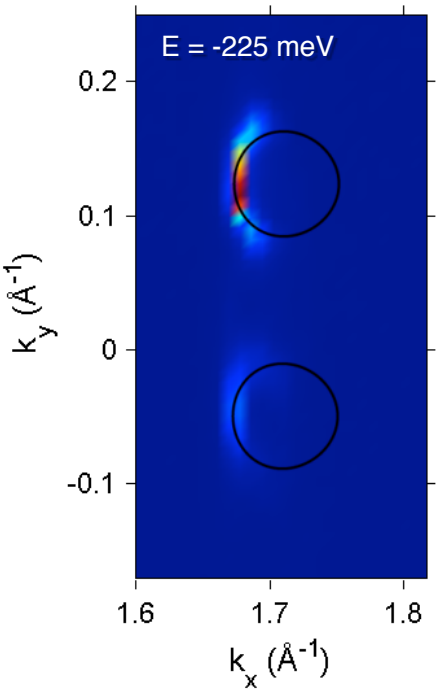

Figure 4.5: Fermi surface of the cones in Fig. 4.4 at $E = -225\,\text{meV}$. Theoretical curves according to Eq. 1.1 are overlaid in black. Intensity distribution is as expected due to matrix elements.

that must be emphasized is that furnace-grown and UHV-grown epitaxial graphenes on SiC are quite different, both structurally and electronically. In addition to a two-order-of-magnitude reduction in graphene domain size, ARPES measurements of UHV-grown C-face graphene show a large electron doping of $E_D - E_F = 0.2$ eV with poorly developed π- and σ-bands.[23] The doping level difference is likely due to charge coupling between SiC and the thinner UHV-grown films, while broad π-bands are due to film disorder. The remarkable result of multiple linear bands characteristic of rotated, effectively isolated single graphene sheets confirms predictions that the unique stacking of MEG grown on the carbon-face should preserve the symmetry of isolated graphene.[20, 53, 37] To demonstrate this, we first point out a few structural details of C-face films.

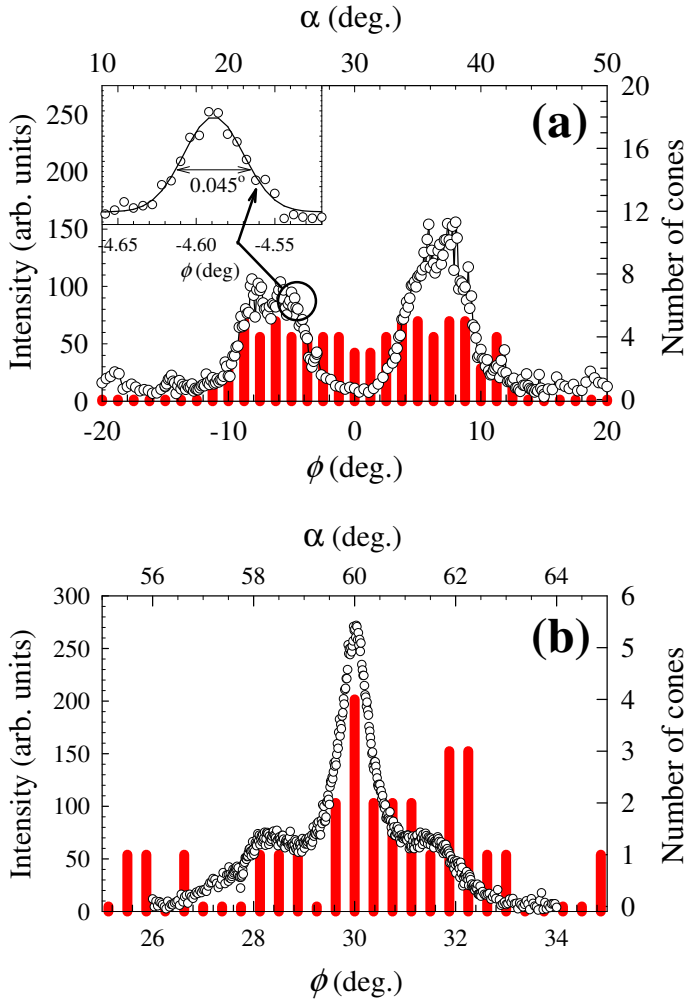

Figure 4.6: Comparison of the graphene SXRD angular distribution in ϕ ($\circ$) and the ARPES Dirac cone histograms in α (solid red). (a) SXRD graphene distribution taken around $\phi = 0°$ and corresponding ARPES histogram of cones distributed around $\alpha = 30°$. Inset, magnified view of a single rotation angle. (b) SXRD distribution taken around $\phi = 30°$ and corresponding ARPES histogram of cones distributed around $\alpha = 60°$.

4.5 Rotation angles

We have plotted SXRD azimuthal scans near $\phi = 0°$ and 30° in Fig. 4.6. Note that while the exact distribution of graphene rotation angles is sample-dependent (possibly due to SiC miscut angle/orientation), the probability of rotation angles near $\phi = 30°$ is nearly equal to the probability of angles near 0°, regardless of sample or film thickness (*i.e.*, the areas under the x-ray curves at each angle are nearly equal). This, along with SXRD reflectivity measurements, indicates that approximately every-other sheet is rotated $\sim 30°$ instead of the graphitic $\sim 60°$,[37, 35, 84] in contrast to the "occasional" small angles rotations proposed by STM measurements.[6] In other words, AB-pairs should be considered to be faults in the stacking order. The distribution of rotation angles around $\phi = 0°$ and 30° is determined by an entropy term that selects from a number of SiC-graphene commensurate angles with small energy differences.[35] There are more commensurate angles per radian of arc at $\phi = 0°$, which explains the observed broader distribution around 0° in Fig. 4.6a.[35] Note also that the angular width of each discrete rotation is very narrow; a detailed scan of one such angle is shown in the inset of Fig. 4.6a. Its width is 0.045°, corresponding to an x-ray rotational coherence distance of ~ 1 μm.

To show the correlation between graphene rotation angle ϕ and the ΓK rotation direction α, note that the ΓK direction in ARPES is rotated 30° from the graphene reciprocal space direction, a_G^* [see Fig. 4.1a]. This means that the ΓK direction for a graphene sheet rotated by ϕ from the $\langle 21\bar{3}0\rangle$ direction is at an angle $\alpha = \phi - 30°$ relative to the SiC $\langle 10\bar{1}0\rangle$ [see Fig. 4.1]. For example, graphene rotated $\phi = 30°$ relative to the $\langle 21\bar{3}0\rangle$ direction of SiC has the ΓK direction along the $\langle 21\bar{3}0\rangle$ direction. We have marked the discrete rotation angles of the ARPES Dirac cones (near $\alpha = 30°$) against the angular distribution measured by SXRD in Fig. 4.6a [$\alpha = 30° + \tan^{-1}(k_\perp/k_{\Gamma K})$, where $k_\perp$ is taken from ARPES scans like that shown in Fig. 4.4]. It is clear that the rotated cones correlate well with the SXRD data,

with many more rotations between 2° and 10°. Note that the SXRD beam size is $\sim$ 3 mm and the ARPES beam size is $\sim$ 40 μm, which explains why ARPES data shows a small number of discrete rotated cones and SXRD shows a more continuous distribution averaged over a larger beam footprint. In the $\alpha = 0°$ azimuth, discrete cones are not always resolved because of the narrow rotational distribution as seen in the inset in Fig. 4.6b. Note that the angular scale in Fig. 4.6b is expanded by a factor of two compared to (a). The reason discrete cones may not observed is a combination of the narrow distribution of commensurate rotations at $\phi = 30°$ and the wide angular acceptance of ARPES ($\sim 0.34°$). Nevertheless, the ARPES distribution of cones again coincides with the measured SXRD angular distribution [Fig. 4.6b].

4.6 Fermi velocity

The high-energy-resolution dispersion curves allow measurement of two important effects. First, the bands are linear. This is demonstrated more clearly in Fig. 4.7, where we plot the position of one branch of a Dirac cone (extracted by fitting the ARPES MDCs to Lorentzian peaks). Within the error bars of the experiment, there are no significant deviations from linearity, consistent with weak electron-phonon coupling at very low carrier densities.[16] The average Fermi velocity, derived from the slope of $E(\Delta k)$, was found to be $\langle v_F \rangle = 1.0 \pm 0.05 \times 10^6$ m/s for energies down to $\sim$ 0.5eV below E_D. This value is larger than v_F for bulk graphite ($v_F \simeq 0.86 \times 10^6$m/sec) [15] but within error bars of values obtained from infrared measurements ($1.02 \pm 0.01 \times 10^6$ m/s),[75] scanning tunneling spectroscopy ($1.07 \pm 0.01 \times 10^6$ m/s),[65] and electronic transport (1.0×10^6 m/s).[5]

4.7 Carrier scattering time

Secondly, the definition of the bands is an indication of long carrier scattering time (large scattering length). The Lorentzian half-width at half-maximum, γ, of observed MDCs [see inset, Fig. 4.7] is inversely proportional to the carrier scattering time

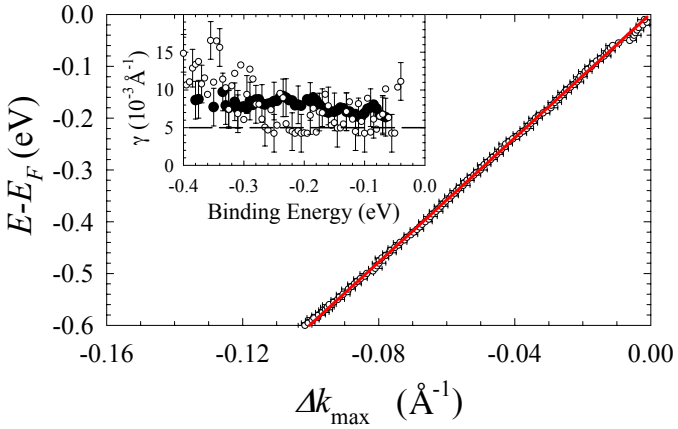

Figure 4.7: $E(\Delta k_{\max}) - E_F$ versus $\Delta k \equiv k_D - k$. k_D is the K-point position and k is the Lorentzian center from fits to ARPES MDCs. $\Delta k_{\max}$ is measured perpendicular to the ΓK direction near the K-point. Solid line is a linear fit. Inset is a plot of the MDC HWHM, γ, as a function of binding energy at 6 K ($\bullet$) and 300 K ($\circ$). Dashed line is the ARPES instrument resolution.

$\tau = 1/(2\gamma v_F)$.[16] Because the observed width is within error bars of the instrument resolution, I can only place a lower bound at $\tau > 20$ fs. This is consistent with measurements of τ in these samples in infrared experiments, which place the value at $\tau = 100 - 300$ fs,[75] and transport, which finds $\tau \sim 260$ ps.[107] Note also that there is no measurable change in τ between 6 K and 300 K.

ARPES measurements show that the band structure of MEG grown on the C-face of SiC consists of multiple undistorted, linearly dispersing graphene bands originating from individual rotated layers in the multilayer film. The observed Dirac cones definitively demonstrate that that the graphene sheets in the MEG film should be considered as electronically ideal, essentially isolated graphene sheets. The origin of this unusual behavior is MEG's unique stacking order. The requirement for preservation of graphene's linear dispersion in a multilayer stack is a breaking of the AB-stacking symmetry of graphite to maintain the equivalency of the A- and B-sublattices, and this is accomplished by introducing relative rotations between adjacent sheets at angles other than 60° (graphitic stacking).[20, 53, 37] As C-face graphene films grow,

the substrate apparently forces relative rotations of $\sim 30 \pm 7°$, with graphitic *AB*-stacked pairs appearing only as infrequent stacking faults. The physical basis of this tendency is not fully understood, but its implication is that uniform single- or double-layer graphene films are not necessarily required for fabrication of C-face graphene electronics, since even multilayer films have the desired electronic structure. Further study will no doubt lead to improved theoretical understanding of the growth process, enabling further optimization of the stacking order.

CHAPTER V

CHEMICAL MODIFICATION: GRAPHENE OXIDE

Graphene oxide (GO) flakes have been deposited to bridge the gap between two epitaxial graphene electrodes to produce all-graphene devices. Electrical measurements indicate the presence of Schottky barriers (SB) at the graphene-graphene oxide junctions, as a consequence of a band gap in GO. The barrier height is found to be about 0.7 eV, and is reduced after annealing at 180 °C, implying that the gap can be tuned by changing the degree of oxidation. A lower limit of the GO mobility was found to be $850\,\mathrm{cm}^2/(\mathrm{V}\cdot\mathrm{s})$, rivaling silicon. *In situ* local oxidation of patterned epitaxial graphene has been achieved.

5.1 Routes to semiconducting graphene

Inspired by the exceptional properties of carbon nanotubes, epitaxial graphene-based electronics was conceived as a possible new platform for post-CMOS electronics. In contrast to carbon nanotubes, graphene layers can be patterned to produce interconnected all-carbon structures, thereby overcoming a wide variety of problems facing nanotube-based electronics. The group's earlier work focused primarily on producing and characterizing device-quality epitaxial graphene (EG) on silicon carbide [4, 5, 107, 19, 36, 97]. Here we demonstrate the production and properties of the epitaxial graphene-graphene oxide Schottky barrier. We also successfully chemically patterned epitaxial graphene to produce seamless graphene oxide-to-graphene junctions, thereby dramatically enhancing epitaxial graphene electronics.

We recently showed that EG can be reliably patterned over large areas to produce hundreds of functioning high-mobility field effect transistors (FET) over the entire surface of a 3×4 mm chip using high-κ dielectrics [47]. Next steps involve patterning

and tailoring the properties of EG. Conventional semiconductor devices rely on a significant band gap; graphene, by contrast, is a semimetal, which severely limits the switching potential of graphene FETs (currently the maximum off-to-on resistance ratio for EG is about 35). The high mobility of EG (up to $250,000\,\mathrm{cm}^2/\mathrm{V}\cdot\mathrm{s}$) offsets this deficiency for certain specialized applications. Clearly, the versatility of graphene electronics is greatly increased by converting graphene into a semiconductor. One way to achieve this is by nanopatterning. It was predicted that the electronic structure of a nanoscopic graphene ribbon should mimic that of a carbon nanotube [67, 101] and semiconducting nanopatterned graphene ribbons on exfoliated graphene flakes have been demonstrated [34, 55].

A far more convenient scheme is to chemically convert graphene to a semiconductor. Here we demonstrate the properties of (semiconducting) graphene oxide (GO), integrated into patterned EG structures. GO, first described in 1859 [14], consists of graphene layers whose surfaces are oxidized without disrupting the hexagonal graphene topology. Impressive demonstrations of deposited single-layer GO [52] spurred research into alternative methods to produce a single graphene layer, by reducing deposited GO back to graphene [88, 31, 30]. In contrast, here we are interested in the semiconducting properties of GO and the capability to locally convert EG to GO. For electronics applications, multilayered epitaxial graphene has several advantages over single layer graphene: the patterned structures are more robust, the interior layers are protected from the environment, and the layered structure allows intercalation.

5.2 Graphene oxide deposition

Suspensions of $\sim 1\mu$m GO flakes were obtained from Mallouk *et al.*[52] An AC dielectrophoresis method was used to deposit flakes over pairs of Au electrodes patterned on an oxidized Si wafer, or over patterned EG electrodes, separated by 400, 800, or

1400 nm gaps. We found that an AC voltage of $2-3$ V peak-to-peak at $20-50$ kHz produced optimal results. Samples were finally heated to 100 °C for 30 minutes in order to drive off adsorbed water vapor.

We have taken AFM images of over 30 GO flakes spanning electrode gaps. Most of them are single layers that are usually flat and free of wrinkles. The measured thickness of a single GO layer on SiO_2 ranges from 0.9 to 1.5 nm, consistent with Ref. [52], while it is 1.5 to 2.2 nm on EG. Fig. 5.1a and 5.1b show typical images of flakes over pairs of electrodes. Fig. 5.1b shows a single-layer GO flake deposited over an EG gap. All single-layer flakes have remarkably similar I-V characteristics, as discussed in detail below. Fig. 5.1a shows a bilayer flake (indicated by the step on the right electrode) deposited over a Au electrode pair separated by a 400 nm gap. Unlike single layer flakes, the bilayer flake is insulating for bias voltages up to 20 V, which may indicate that the electronic properties of bilayer GO differ significantly from those of single-layer GO. Devices made on Au electrodes and on EG electrodes exhibit similar current-voltage (I-V) behavior, characteristic of back-to-back Schottky diodes (see below).

5.3 Back-to-back Schottky diodes

We have measured devices with varying gap widths: 400 nm, 800 nm, 1400 nm. A typical I-V curve of an EG-GO-EG device, shown in Fig. 5.1d, exhibits strong nonlinearity. The I-Vs do not systematically vary with the gap width. Because bulk resistance would scale with the applied electric field (not the potential), the nonlinearity is not an indication of bulk resistance in GO. This specifically rules out strong localization effects in GO as the origin of the nonlinearity [41].

Another important feature is the asymmetry of the I-V with respect to the bias voltage. This often-seen asymmetry correlates with the ratio of the lengths of the contact edges on the two electrodes (not the area of the two GO-contact overlap regions).

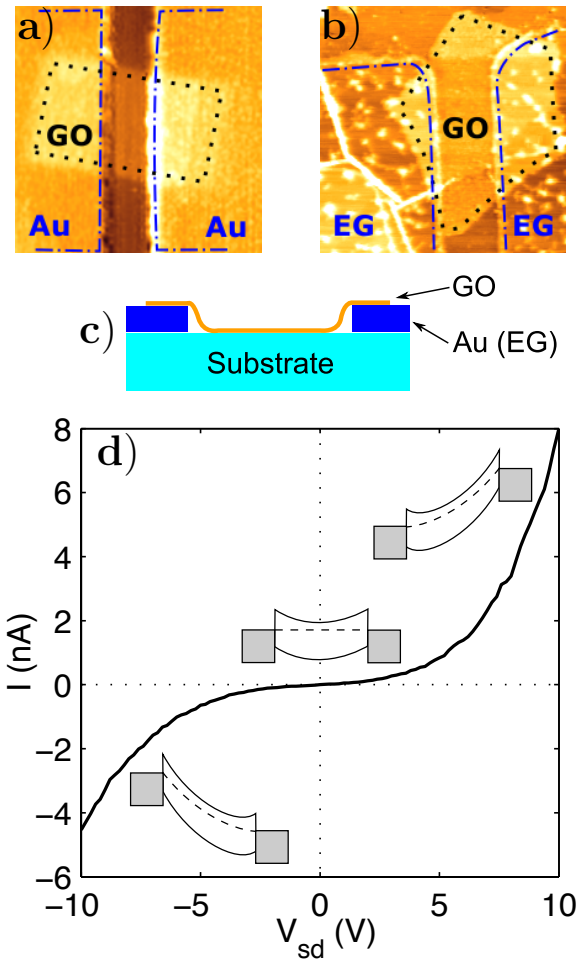

Figure 5.1: EG/GO metal-semiconductor-metal (MSM) device. **a**) A bilayer rectangular GO flake (outlined by a black dotted line) over a 400nm Au gap. The Au pads are outlined by blue dash-dot lines. **b**) A pentagonal GO flake bridges two EG electrodes. Both images are $2\,\mu$m $\times$ $2\,\mu$m. The bright spots on EG are e-beam resist (PMMA) residue, while the bright lines are wrinkles that are often seen on C-face EG. **c**) The layout of GO devices (side view). **d**) I-V characteristics of an 800 nm device, consisting of back-to-back Schottky diodes. The inset schematically shows band diagrams for the device under various biasing conditions. The asymmetry of the I-V characteristics reflects the dissimilarity of the two junctions.

The asymmetry, and its correlation with the length of the edge, indicates that the impedance is primarily due to the contact edge between one of the two EG electrodes and the GO flake (*i.e.* the junction length). As with carbon nanotube SBs [39], this picture is consistent with a SB at the GO-conductor edge, and inconsistent with an impedance distributed over the contact area of the GO and the electrode. Therefore, the structures correspond to two back-to-back SBs (Fig. 5.1d). When a bias voltage is applied, one SB is under reverse bias, while the other is forward-biased. Consequently, the impedance will always be dominated by characteristics of the reverse-biased SB. The impedance of the reverse-biased SB should be approximately inversely proportional to the junction length, *i.e.* the lower impedance branch of an I-V corresponds to the reverse-biased SB with the longer junction length. With this insight, the polarity of the SBs is determined and the carrier type can be identified. We find that some GO flakes are p-type, while others are n-type and carrier densities are rather low and variable (order of $10^{10} - 10^{11}$ cm^{-2}, see below). The arbitrary nature of the carrier type and density indicates that environment and substrate effects play a role. This situation is similar to carbon nanotubes and exfoliated graphene [51, 90], which are prepared under similar, non-pristine conditions, causing arbitrary doping by impurities.

5.4 Analysis

A detailed analysis of the SB characteristics follows. The SB at the interface of a 2-dimensional electron gas (2DEG) from a modulation doped heterostructure and 3-dimensional metal has recently been studied. Based on a thermionic emission model, the quasisaturation reverse bias current through a SB can be described by [2]:

$$J_s = \frac{2q}{h^2}\sqrt{2\pi m^*}(k_B T)^{\frac{3}{2}} \times \exp\left(-\frac{q\phi_b}{k_B T}\right) \times \exp\left(\frac{q\Delta\phi_b}{k_B T}\right) \tag{5.1}$$

where m^* is the effective electron mass, ϕ_b is the effective SB height. $\Delta\phi_b$ is the field dependence of the barrier. For image-force lowering of the barrier, it follows [76]:

$$\Delta\phi_b = \left\{ \frac{q^3 N_d}{8\pi^2(\epsilon_s')^2\epsilon_s} \left(\phi_b + V_r - \xi - \frac{k_B T}{q} \right) \right\}^{\frac{1}{4}} \tag{5.2}$$

where N_d is the ionized donor (or acceptor) density, V_r is the reverse bias voltage, ξ is the distance between the Fermi level of the semiconductor and the bottom of the conduction band. ϵ' and ϵ are high frequency and static dielectric constants of the semiconductor, respectively. ϕ_b is usually less than 1 eV and $k_B T \approx 30$ meV at $T = 300$ K, so at high bias, the image force lowering of the barrier is proportional to the one-fourth power of the bias.

Figure 5.2a and 5.2b show the I-V characteristics of a 400 nm device at 77, 100, 150, 200, 240, 270, 300 and 320 K. As the temperature decreases, the current is suppressed, as expected for a thermionic emission current. To test if Eq. (5.1) and (5.2) describe the data, we plot $I/T^{3/2}$ as a function of $V_{sd}^{1/4}/T$ in a semi-log plot. The curves are linear, which is consistent with Eq. (5.1). The barrier height of the SB was calculated from the intercept, assuming the mass of a free electron. This mass approximation is justified by the fact that the estimation of the barrier height weakly depends on m^* (*e. g.*, a change of two orders of magnitude in m^* results in a change of less than 10% in ϕ_b). The barrier height at room temperature is estimated to be 0.5 eV; it decreases with temperature (Fig. 5.3a). Such temperature dependence of the barrier height is commonly seen in SB diodes and is associated with the ideality factor n of the diode [99] or a temperature dependent band gap. Effects that can cause a departure from unity in the value of n include thermionic-field emission processes, interface effects, electron-hole recombination or nonuniformities in the SB [76]. Further study is needed to identify the effect in this case.

The ionized donor (or acceptor) density N_d was calculated from the slope of $\ln(I/T^{3/2})$ versus $V_{sd}^{1/4}/T$. The dielectric constant can be approximated as an average of that of the substrate SiC and that of the air above, *i.e.* $\epsilon = (\epsilon_{\mathrm{SiC}} + 1)/2$.

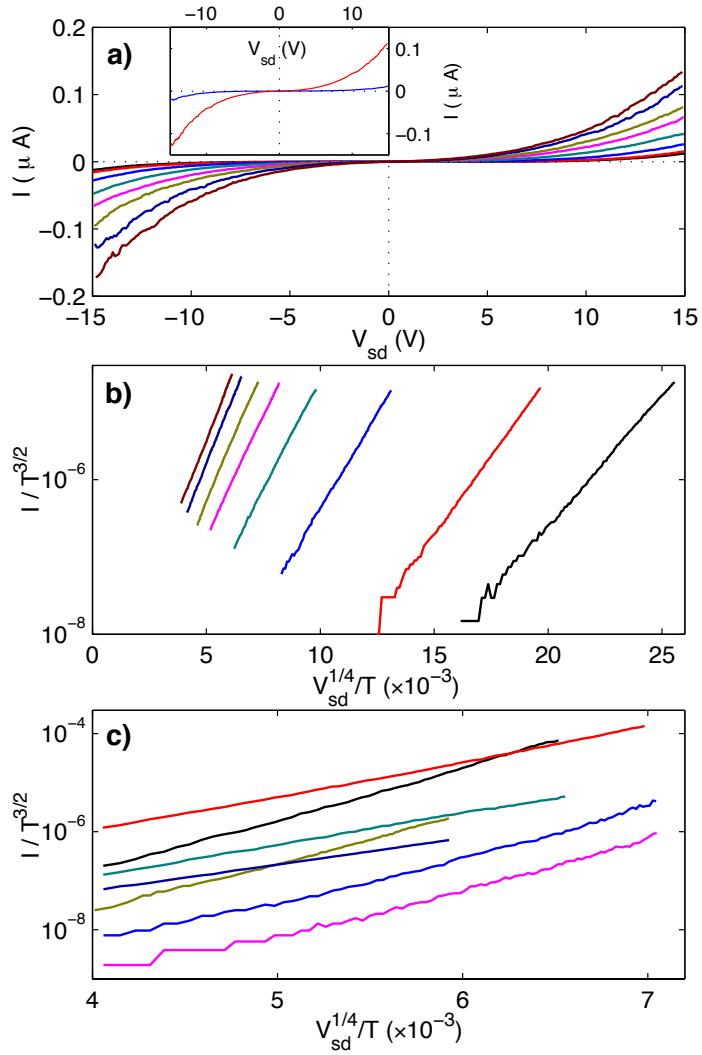

Figure 5.2: **a**) and **b**), I-V characteristics of a 400 nm device at several temperatures: 77 (black), 100 (red), 150 (blue), 200 (cyan), 240 (pink), 270 (dark yellow), 300 (dark blue) and 320 K (magenta). The sample was cured at 180 °C for 16 hours. **a**) Nonlinear I-V. Inset: I-V before (blue) and after (red) curing. The increased current indicates a lowering of the SB height. **b**) $I/T^{3/2}$ as a function of $V_{sd}^{1/4}/T$ for $V_{sd} > 2$ V. The observed linear dependence is as expected for a back-biased Schottky diode where the current is determined by thermionic emission over the barrier (Eq. (5.1), (5.2)). The slope of the line gives the ionized donor density. **c**) $I/T^{3/2}$ vs $V_{sd}^{1/4}/T$ plots at 300K for two Au/GO devices (black and red), the device in **a**) before annealing (blue), another 400 nm EG/GO device before and after annealing (cyan and pink), an 800 nm EG/GO device (dark yellow) and a 1400 nm EG/GO device (dark blue).

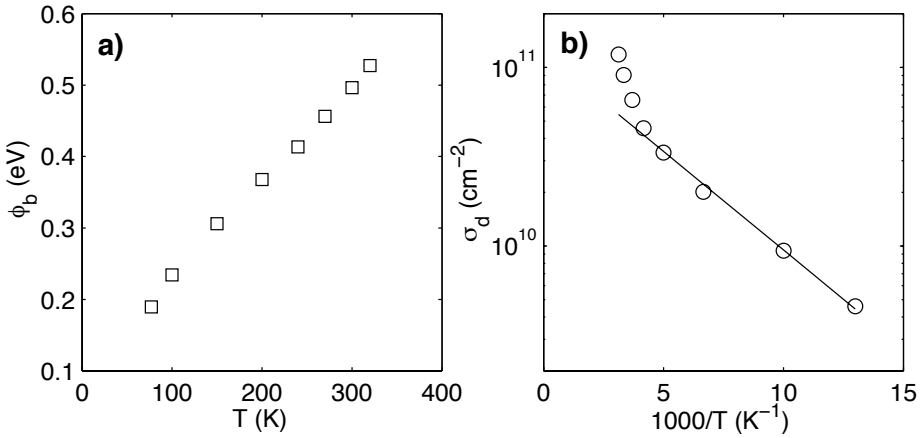

Figure 5.3: Temperature dependence of the device parameters. **a**) The temperature dependence of the SB height. **b**) The area density of ionized donors as a function of inverse temperature. Circles: experiment; Line: A fit to $N_d \propto \exp(-E_i/2k_BT)$ gives $E_i \approx 61$ meV.

Since $\epsilon_{\mathrm{SiC}} = 6.7$ and $\epsilon'_{\mathrm{SiC}} = 10$, we have $\epsilon = 3.85$ and $\epsilon' = 5.5$. According to Eq. (5.2), we find that $N_d \approx 4.5 \times 10^{17}$ cm^{-3} at 300 K, corresponding to an area density σ_d of 9.1×10^{10} cm^{-2}, assuming that the thickness of the flake is 2 nm. For donors with an ionization energy E_i, $N_d \propto \exp(-E_i/2k_BT)$ when $E_i \gg k_BT$ [48]. Consequently, E_i of the sample was obtained from the temperature dependence of N_d (Fig. 5.3b). We find $E_i \approx 61$ meV, a typical value for these SBs. More than twenty samples have been studied, and all are described by Eq. (5.1) (see representative data in Fig. 5.2c). The doping density was found to be between 2.2×10^{10} and 6.1×10^{11} cm^{-2}, while ϕ_b ranges from 0.45 to 0.7 eV.

5.5 Tuning degree of oxidation

It is known that GO loses oxygen when heated above 100 °C [88], *i.e.* the degree of oxidization can be adjusted by curing. The data in Fig. 5.2 were obtained after a curing process at 180 °C for 16 hours. The *I*-*V* characteristics before and after curing are plotted in the inset of Fig. 5.2a. A significant increase of the current after curing was observed and analysis reveals that the doping density decreased (from 3.8×10^{11}

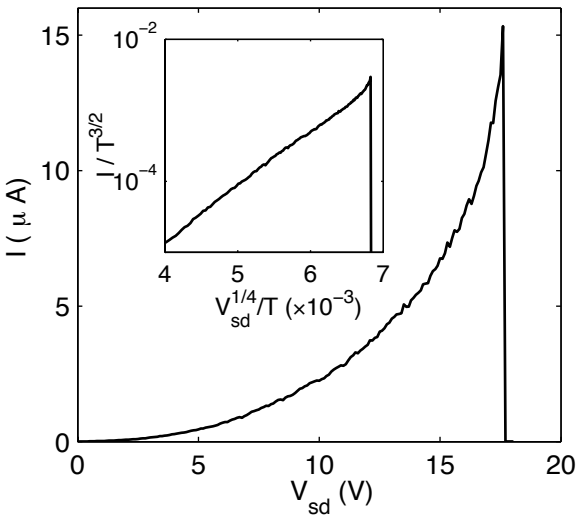

Figure 5.4: An Au-GO-Au device reached its breakdown voltage and burned out. The insets is a plot of $I/T^{3/2}$ as a function of $V_{sd}^{1/4}/T$ for $V_{sd} > 2$ V.

to 9.1×10^{10} cm^{-2}). More importantly, ϕ_b decreased from 0.7 to 0.5 eV. A similar trend was observed in all other cured samples. This indicates that we can use thermal oxygen desorption to tune the band structure, as suggested in Ref. [54].

5.6 Mobility estimate

Since the impedance of the device is dominated by the SB, we cannot directly measure the bulk resistivity of the GO flake. However, if we assume that the bulk resistance is ohmic, we can obtain an upper limit. The dynamic resistance of the device is the sum of the dynamic resistances of two SBs and the bulk: $R = R_{SB1} + R_{SB2} + R_{bulk}$. We measured the I-V of a Au-GO-Au structure up to the breakdown voltage of 17.5 V where it burned out (see Fig. 5.4). Just prior to failure, the dynamic resistance was only 74 kΩ, which sets the upper limit of the bulk resistivity at about 74 kΩ/sq (aspect ratio ~ 1). The doping density calculated from the slope of the $\ln(I) - V^{1/4}$ plot is about 9.9×10^{10} cm^{-2}, and the mobility of this flake is therefore at least $850\,\mathrm{cm}^2/(\mathrm{V} \cdot \mathrm{s})$.

5.7 *In situ* oxidized epitaxial graphene

I also succeeded in oxidizing both patterned and unpatterned EG chips. Unpatterned EG chips were oxidized by Hummers method as described in Appendix A.[42] The surface morphology (*cf.* Fig. 5.1b) as measured by AFM exhibited no apparent changes from before to after oxidation. GO formation was verified by its characteristic Raman signature [88] and a resistivity increase by orders of magnitude $> 10^4$. Likewise, several ribbons were patterned on an as-grown EG chip. Hydrogen silsesquioxane (HSQ) was spun on the sample and e-beam patterned to produce rectangular windows over the central portions of the ribbons. The sample was subsequently oxidized. The resultant EG/GO metal-semiconductor-metal device is completely off, even at bias voltages up to 60 V, suggesting a large SB height (as for the GO bilayer flake, Fig. 5.1a). However, after subjection to e-beam irradiation (30 keV), the devices displayed a nonlinear I-V, which again is well described by Eq. (5.1) and (5.2). Because the devices are made from a continuous sheet of EG, impurities and interface states are essentially excluded. Hence, other than the SB, an insulating tunnel-barrier layer is unlikely to exist. For all three types of junctions, i.e. Au/GO, EG/GO and EG/GO (oxidized *in situ*), the I-V is described by the same equations, strongly supporting our conclusion that the Schottky effect dominates the transport through those junctions. Further note that the Schottky barriers were found to be ≤ 0.5 eV after e-beam exposure. These significantly reduced SB heights indicate that e-beam treatment can be used to locally adjust the band gap, consistent with the known deoxidation of graphene oxide by electron beam exposure [28].

5.8 Summary

In summary, we successfully produced all-graphene metal-semiconductor-metal devices. The I-V characteristics of the device are explained by thermionic emission over a Schottky barrier. The barrier height is found to be as large as 0.7 eV, which

indicates a band gap of at least this value in GO. The mobility of GO is larger than 850 cm^2/Vs, hence in the range suitable for room temperature electronics. Further tuning the band gap has been achieved by changing the degree of oxidation both by thermal curing and by e-beam irradiation.

5.9 Methods

5.9.1 Optical absorption of graphene oxide suspension

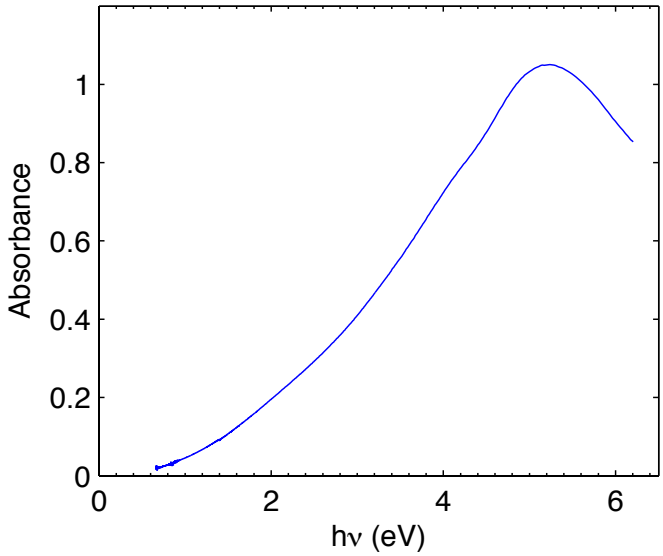

Figure 5.5: The absorbance spectrum of graphene oxide suspension.

Fig. 5.5 is the optical absorbance spectrum of a GO suspension. A strong absorbance gradually develops from near zero at low energies. The shape of the absorbance curve, noting that the extrapolated absorbance vanishes at $h\nu > 0$, is consistent with a semiconductor with a distribution of band gaps and/or an indirect band gap.[62] Considering that the spectrum is an average over flakes in the suspension, a distribution of band gaps is expected.

5.9.2 Conversion of epitaxial graphene to epitaxial graphene oxide

Hummers' method was used to convert epitaxial graphene on SiC to graphene oxide.

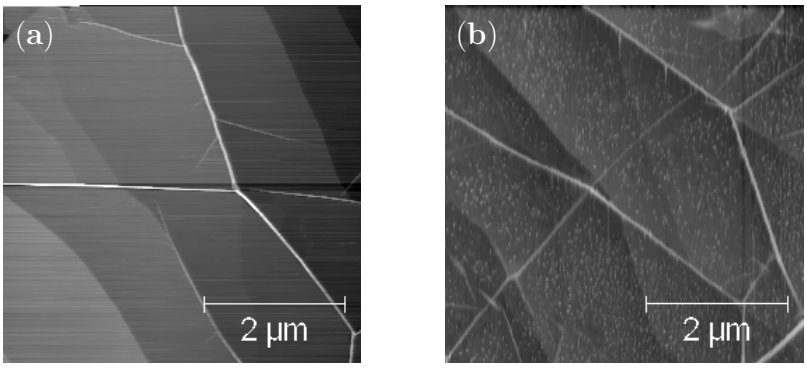

Figure 5.6: AFM images of EG and GO on SiC. (a) As grown EG. (b) Oxidized EG.

The surface morphology was examined by AFM, as shown in Fig. 5.6. Before oxidation, EG shows micron size terraces, which are in fact SiC terraces due to the $\sim 0.1^\circ$ miscut angle of the SiC wafer (nominally on-axis), blanketed by EG. The bright lines seen in the image are graphene pleats formed due to the difference in thermal expansion between EG and SiC. After oxidation, the surface looks similar and no apparent peeling was observed, indicating that the overall structure of EG remains intact.

Raman scattering measurements were carried out on different samples and locations using a laser excitation of 514 nm. The spectra for GO flakes deposited on a Si chip and GO made from EG on SiC are shown in Fig. 5.7. The absence of the 2D band around 2726 cm^{-1} after oxidation indicates that all graphene layers have been oxidized, as supported by subsequent electrical measurements. Two peaks around 1500 cm^{-1} (D and G band) are essentially identical to the characteristic peaks of graphene oxide. Therefore, oxidized EG is the same material as GO flakes made from graphite.

5.9.3 Creation of EG/GO junctions from a continuous EG film

To make an EG-GO junction from a continuous EG film, an EG sample was first patterned into 3 μm-wide ribbons using e-beam lithography. A 40 nm-thick e-beam

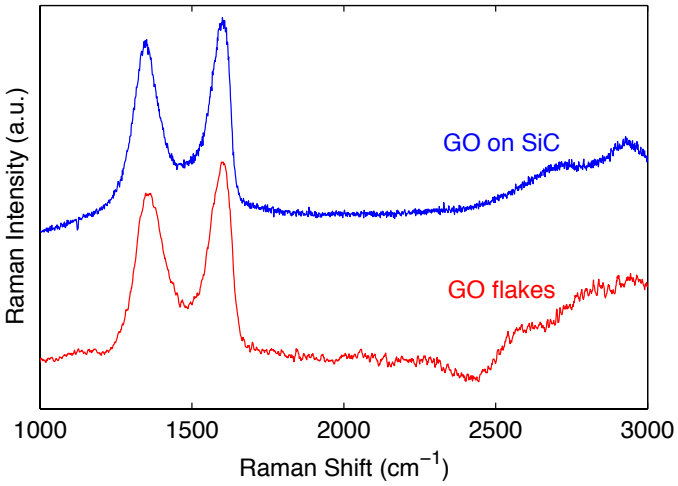

Figure 5.7: Raman spectra of GO flakes deposited on Si and GO made from EG on SiC.

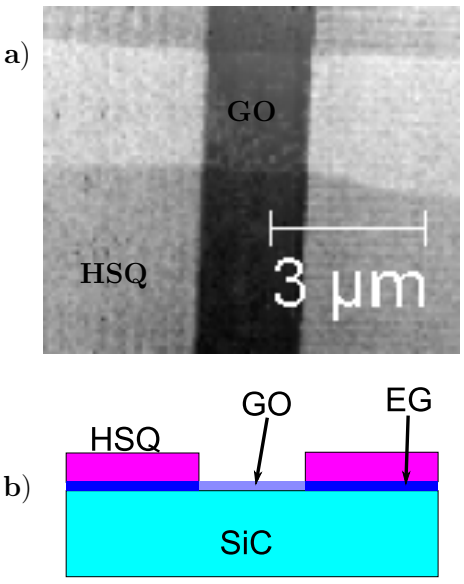

Figure 5.8: An EG-GO-EG device. (a) An AFM image of the device. (b) A schematic drawing of the device.

resist, hydrogen silsesquioxane (HSQ), was then spun on the sample. On an EG ribbon, I opened a window by e-beam patterning and development. After subjection to the chemical oxidation processes (Hummers' method), EG within the window was converted into GO, while EG under HSQ is protected from the chemical reactions. The resultant structure is an EG-GO-EG junction within a continuous sheet, as shown in Fig. 5.8. This is an intrinsic junction in that the "carbon skeleton" is continuous across the junction. As a result, extrinsic effects such as impurities and interface layers are obviated.

5.9.4 Electrical characterization of EG-GO junctions

Electrical measurements were performed on *in situ* oxidized EG/GO devices after annealing at 100 °C to remove water. The devices were completely off, *i.e.* no measurable current was observed up to 60 V for all devices, suggesting a large Schottky barrier. This also indicates that all graphene layers have been oxidized.

E-beam exposure is known to induce reduction of GO. For our multilayered GO on SiC, we found that brief exposure to a 30 kV e-beam reduces the Schottky barrier height, consistent with the known effect. Fig. 5.9 shows the $I-V$s of a device before and after e-beam exposure. The strong nonlinear $I-V$ after exposure has been successfully analyzed used the 2D Schottky barrier model. The barrier height was found to be 0.5 eV.

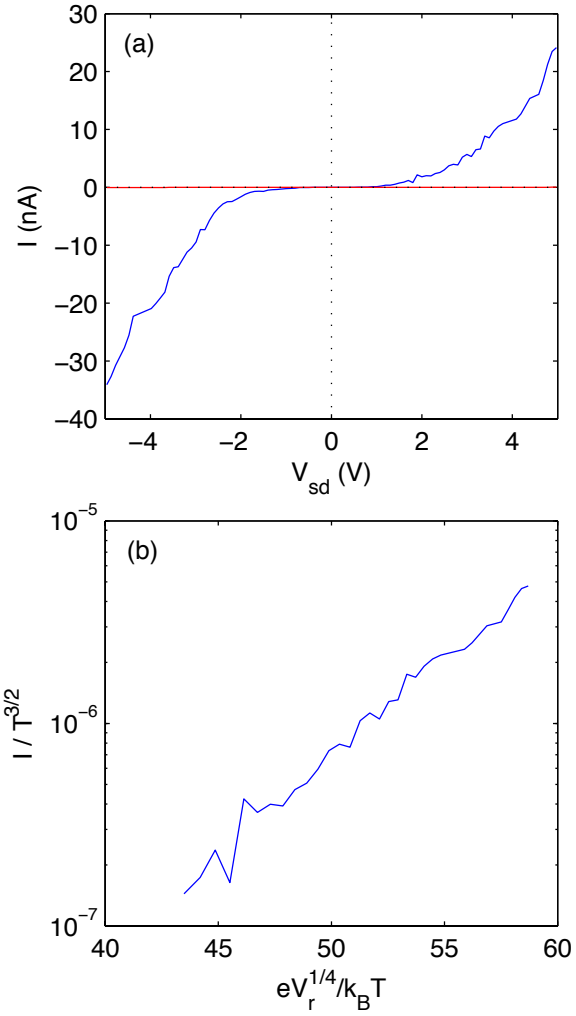

Figure 5.9: I-V characteristic of an *in situ* oxidized EG/GO device. (a) I-Vs of a device before e-beam exposure (red line) and after (blue line). (b) A plot of $I/T^{3/2}$ vs $eV_{sd}^{1/4}/k_BT$ for $V_{sd} > 1.4$V. The linear behavior is consistent with the 2D Schottky barrier model explained in the text.

CHAPTER VI

SELF-ORGANIZED GROWTH

Realization of post-CMOS graphene electronics requires production of semiconducting graphene, which has been a labor-intensive process.[33, 92, 45] I present tailoring of silicon carbide crystals via conventional photolithography and microelectronics processing to enable templated graphene growth on $4H$-SiC$\{1\bar{1}0n\}$ ($n \approx 8$) crystal facets rather than the customary $\{0001\}$ planes.[85] This allows self-organized growth of graphene nanoribbons with dimensions defined by those of the facet. Selective growth is confirmed by Raman spectroscopy and high-resolution transmission electron microscopy (HRTEM) measurements, and electrical characterization of prototypic graphene devices shows quantum confinement at low temperature and carrier mobilities up to 2,700 $\mathrm{cm}^2/(\mathrm{V} \cdot \mathrm{s})$ at room temperature. Fabrication of $> 10,000$ top-gated graphene transistors on a 0.24 cm^2 SiC chip demonstrates scalability of this process and represents the highest density of graphene devices reported to date.

Epitaxial graphene on SiC is an exciting new electronic material that presents the possibility of room temperature ballistic devices.[4, 5, 19] Extremely high carrier mobilities, exceeding 250,000 $\mathrm{cm}^2/(\mathrm{V} \cdot \mathrm{s})$ at room temperature, have been observed,[75] and epitaxial graphene has been shown to be compatible with traditional top-down processing techniques.[47, 57] Its linear semi-metallic band structure[86] allows ambipolar tuning of conduction and direct application to RF devices,[66, 58] while other devices require modification of the graphene sheet to induce a band gap. The latter has received significant attention, and has been accomplished by selective chemical treatment[106, 3] and nanoribbon fabrication,[33, 92, 45] which results in a band gap inversely proportional to ribbon width.[67] The nanoribbon approach is promising in

that it has shown large gating effects, but production methods documented thus far, including e-beam lithography[33] and other approaches,[92, 45] are too slow and/or not controllable enough for technological application.

Morphology of epitaxial graphene on SiC is highly influenced by the structure of the underlying substrate. In well-controlled graphene growth conditions,[5, 19, 35, 24, 98] nominally on-axis SiC retains an ordered terrace structure that originates in the miscut angle of the SiC wafer. Many interpret these steps as being problematic,[77] but scanning tunneling microscopy measurements have consistently observed that the graphene lattice is continuous over such steps. This is true of 0.5 nm $4H$-SiC half-unit cell steps and few-nm steps where step bunching occurs.[4, 38] I find [see Fig. 6.1] that this remains true at a much larger scale; graphene pleats typically present on the SiC$(000\bar{1})$ plane[35] are observed traversing prepared SiC steps as large as 150 nm, indicating continuity of graphene over the step. These observations explain transport measurements in which underlying SiC steps appear to have little effect on mobility[5, 108] or observation of the quantum Hall effect,[108] and suggest exploitation of the effect to produce nanoribbons by novel fabrication methods.

6.1 Nano-faceting of SiC

It has long been known[50] that SiC{0001} surfaces exhibit step bunching in various environments. Recent systematic studies have found a greater propensity for step bunching on the (0001) face,[89, 69, 71, 11] with vicinal miscuts toward $\langle 1\bar{1}00\rangle$ displaying bunching of parallel steps into $(1\bar{1}0n)$ "nanofacets" up to $4-5$ unit cells in height, oriented at an angle of $\sim 25^\circ$ to the basal plane.[69, 71] It has been suggested that such nanofacet formation may be understood as a minimization of surface free energy.[68, 69] Steps perpendicular to the directions $\langle 1\bar{1}00\rangle$ are strongly favored on (0001), such that steps formed macroscopically toward $\langle 11\bar{2}0\rangle$ are microscopically zigzagged, with segments perpendicular to $\langle 1\bar{1}00\rangle$.[89, 69, 71, 11] The $(000\bar{1})$ face,

by contrast, seems to form steps without restriction on orientation.[71] Step-bunched nanofaceting has not been observed there previously,[71, 11] but I show in Fig. 6.1 that a $(1\bar{1}0n)$ facet is induced by pre-processing (see below). These results are qualitatively true of both $6H$- and $4H$-SiC polytypes.[71] It is perhaps expected that graphene growth should proceed first on facets, given the lesser bonding of Si atoms, and this has been observed on etching-induced $(1\bar{1}0n)$ [77] and $(11\bar{2}n)$[91] nanofacets.

6.2 Selective growth on SiC$(1\bar{1}0n)$

We propose exertion of control over the natural step bunching mechanism to prepare a crystal facet for self-organized graphene growth [see Fig. 6.2]. Given the discussion above, the best choice for this purpose may be $(1\bar{1}0n)$. Controlled facets are achieved by photolithographic definition of Ni lines on a SiC substrate perpendicular to the $\langle 1\bar{1}00\rangle$ direction; these lines are transferred into the SiC by a fluorine-based reactive ion etch (RIE), which, while relatively simple technologically, allows nm-precision in the etch depth. As depicted in Fig. 6.2, it is the etch depth that ultimately defines the width of nanoribbons prepared. 15 nm etch depths were readily achieved in this work [see Fig. 6.6], which resulting ribbon width (~ 30 nm) is sufficiently narrow to result in a sizable band gap at room temperature.[33, 92, 45] Much narrower widths should be reachable with modest effort. I have nevertheless chosen to focus here on a 100 nm etch depth/~ 250 nm ribbon width that allows convincing demonstration of the concept via accessibility to characterization probes including Raman spectroscopy, yet is narrow enough to exhibit a band gap at low temperature. After removal of the Ni mask and cleaning, the crystal is heated to elevated temperatures (1200 – 1300 °C) at intermediate vacuum (10^{-4} Torr) for 30 min., inducing SiC step flow. The abrupt step relaxes to a $(1\bar{1}0n)$ facet, and the temperature is elevated to > 1450 °C within 1.5 min., maintained for 10 min. for graphene growth, then allowed to cool naturally, falling below 1300 °C within 0.25 min.[4, 5, 35]

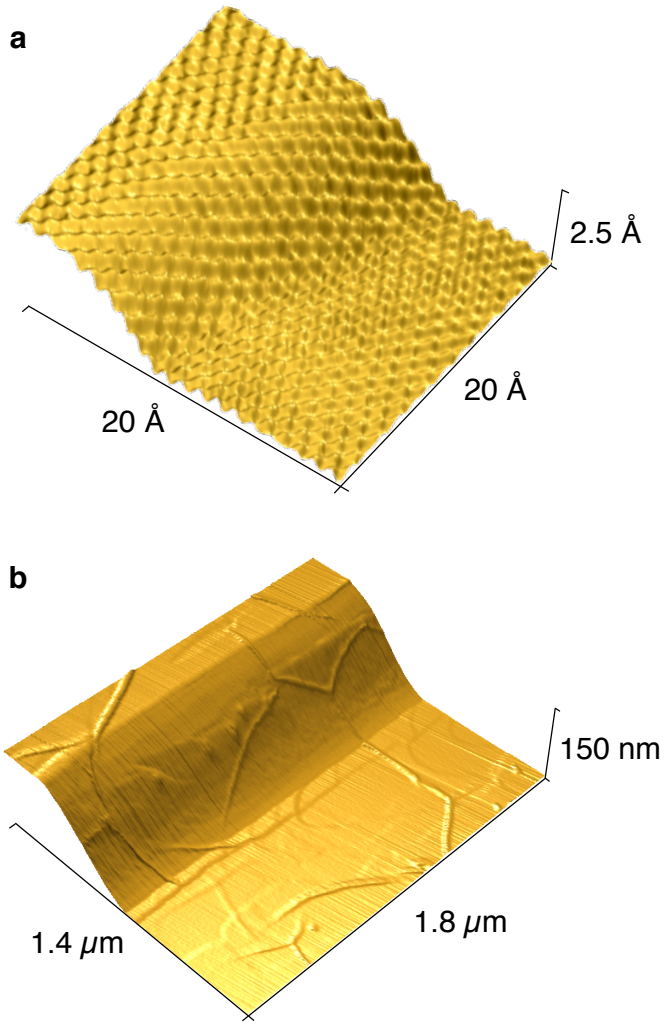

Figure 6.1: (a) STM scan demonstrating continuity of epitaxial graphene over a 2.5 Å step on SiC(0001). Reproduced from Ref. [81] (b) AFM scan demonstrating continuity of multilayer epitaxial graphene over a $\sim$ 145 nm step on the SiC(000$\bar{1}$) plane. Raised pleats are caused by relative contraction of SiC as the sample cools from elevated growth temperatures,[35] and their traversal of the step clearly indicates continuity of graphene over the step.

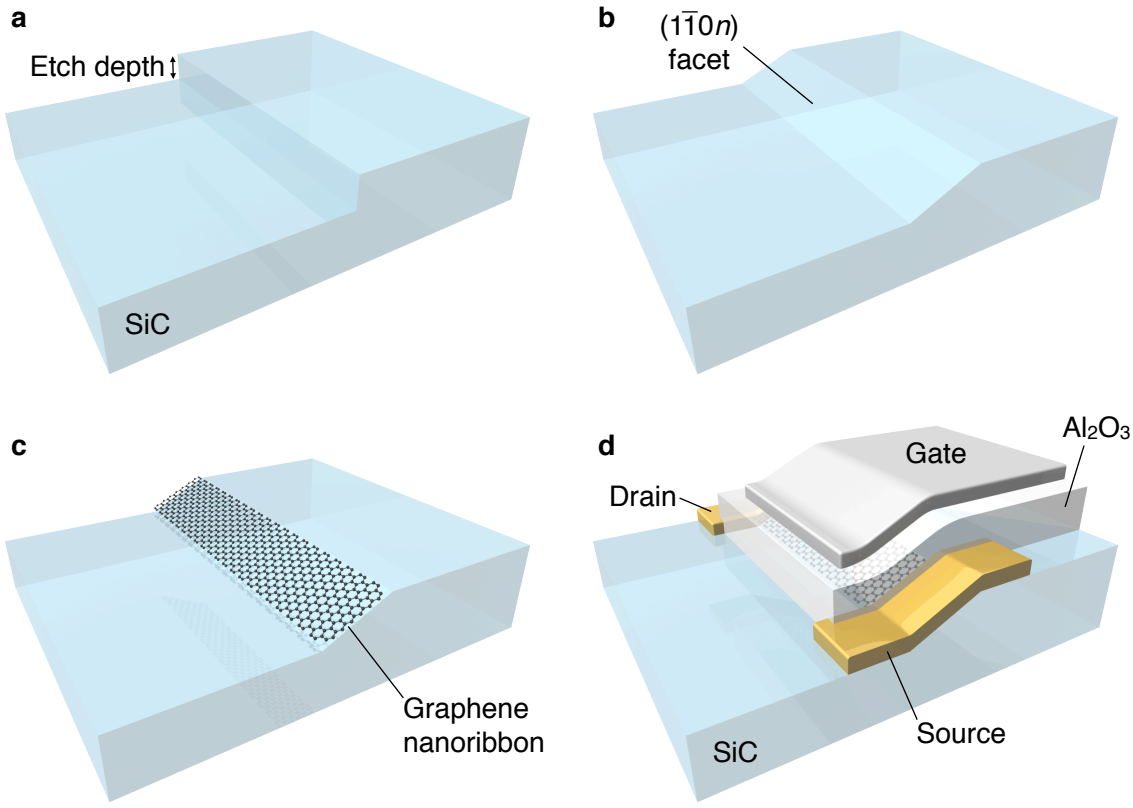

Figure 6.2: Process for tailoring of the SiC crystal for selective graphene growth and device fabrication. (a) nm-scale step is etched into SiC crystal by fluorine-based RIE. (b) Crystal is heated to 1200 – 1300 °C (at low vacuum), inducing step flow and relaxation to the (1$\bar{1}$0n) facet. (c) Upon further heating to $\sim$ 1450°C, self-organized graphene nanoribbon forms on the facet. (d) Complete device with source and drain contacts, graphene nanoribbon channel, Al_2O_3 gate dielectric, and metal top gate, as pictured in Fig. 6.5b.

6.3 Results

This careful control of the growth temperature, time, and atmosphere allows selective growth on the facet, as shown by Raman mapping in Fig. 6.3f. The intensity of the 2D Raman band ($2700\,\mathrm{cm}^{-1}$) characteristic of graphene is mapped over a 100 nm SiC step and adjacent (0001) faces. Little to no intensity is observed on the horizontal surfaces, but significant intensity is seen at the step edge, indicating presence of graphene there. Note that the lateral resolution of the Raman instrument, at $\sim 1\,\mu$m, is much larger than the facet width and the mapping grid spacing.

Cross-sectional HRTEM images (with slightly thicker graphene for visibility) [see Fig. 6.3g] confirm preferential growth. Graphene is observed on the facet, with only partial layers on the horizontal (0001) plane. The facet angle observed, 24°, is in agreement with AFM measurements (not shown) of $24 - 28°$ across multiple samples and locations, corresponding to the high-index SiC facet $(1\bar{1}0n)$, where $n \approx 8$. The precise facet obtained is dependent on processing temperature.[89] It must be noted that apparent imperfections in the graphene sheets may be introduced by the HRTEM specimen polishing process or the high energy electron beam during imaging.[]

Ribbon samples formed on $(000\bar{1})$ [Figs. 6.4a, 6.5b] were prepared for electrical measurement by exposure to an extremely short directional O_2 RIE to remove any graphene fragments from the horizontal $(000\bar{1})$ surface. This was verified by Raman mapping as shown in Fig. 6.3d, and extensive electrical probing confirmed lack of measurable conductivity on the horizontal surfaces. As discussed above, on (0001) [Figs. 6.3g, 6.4b, 6.4c], the selective graphene growth required no post-processing. Metal contacts were deposited for four-terminal measurements without gate and two-terminal measurements with top gates. In the latter case, the graphene surface was functionalized by NO_2,[105] followed by atomic layer deposition (ALD) of Al_2O_3 and lift-off of a metal gate [see Fig. 6.2].

Four-terminal measurements of prepared ribbons [see insets, Figs. 6.4a and 6.4b]

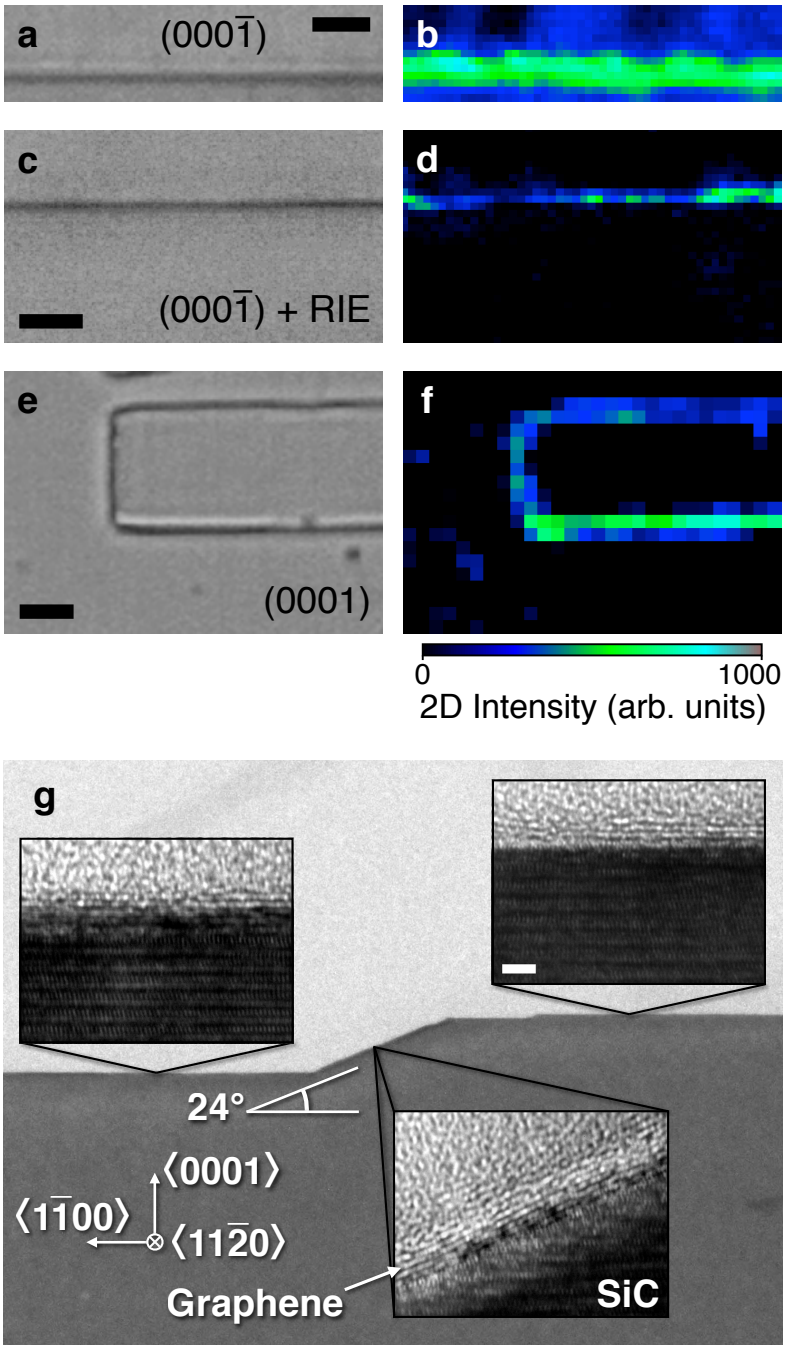

Figure 6.3: (a) Optical micrograph of pre-patterned 100 nm step on the SiC(000$\bar{1}$) face following graphene growth. Scale bars in (a, c, e) are 2 μm. (b) Raman map ($\sim$ 1 μm lat. res., 0.25 μm grid) of the 2D peak intensity at this location indicates preferential graphene growth on the (1$\bar{1}$0n) facet. (c – d) Optical micrograph and Raman map of step on SiC(000$\bar{1}$) following exposure to directional O_2 RIE. (e – f) Optical micrograph and Raman map demonstrating fully selective growth on SiC(0001) without post-treatment. (g) HRTEM cross-sectional images of a similar step on (0001) confirm preferential growth on the (1$\bar{1}$0n) facet. Scale bar is 2 nm, and applies to all insets.

yield sheet resistances of 180 – 1000 Ω/sq., values typically observed in as-grown planar graphene.[19] Fig. 6.4a shows a series of conductance vs. source-drain voltage curves taken between 77 K and 4 K. The behavior is metallic at high temperatures, but quantum confinement is clearly manifested in the nonlinearity observed at 4 K, indicating presence of a small band gap, as expected of this ~ 250 nm-wide ribbon and in agreement with previous reports.[5]

Top-gated two-terminal measurement of similar devices at room temperature is presented in Fig. 6.4b. Though the NO_2-functionalization, one of a handful of recent techniques for enabling adhesion of high-κ dielectrics to graphene, is known to dramatically degrade mobility, on-off ratio, and electron-hole symmetry,[25] I observe large field-effect mobilities, between $\mu_{\mathrm{FE}} = 900$ and 2,700 $\mathrm{cm}^2/(\mathrm{V}\cdot\mathrm{s})$, and on-off ratios as large as four, which values are comparable to or better than those previously reported at room temperature for ribbons of this dimension.[47, 66, 58] The Dirac point (resistance maximum) is typically observed at $V_{\mathrm{g\,Dirac}} \approx -4\,\mathrm{V}$, corresponding to an electron density at $V_{\mathrm{g}} = 0\,\mathrm{V}$ of $3\times10^{12}\,\mathrm{cm}^{-2}$, in agreement with numerous measurements of the first graphene layer above the SiC interface.[4, 5, 19, 57, 58] This indicates that the first graphene layer is modulated by the top gate and the graphene channel is not more than a few layers in thickness. The gating efficiency further confirms selectivity of graphene growth. Recently devised dielectric adhesion methods are expected to result in improved performance by reducing interaction between the graphene channel and dielectric stack.[25]

6.4 Scaling up: 40,000 devices/cm^2

Photolithographic processing allows fabrication of a large number of devices at higher density. An array of top-gated graphene transistors prepared on the $(000\bar{1})$ face of a 4×6 mm SiC chip with SiC etch depth 100 nm is shown in Fig. 6.5b. A single device (source, drain, channel, and gate, as illustrated in Fig. 6.2) occupies a $35\times65\,\mu$m

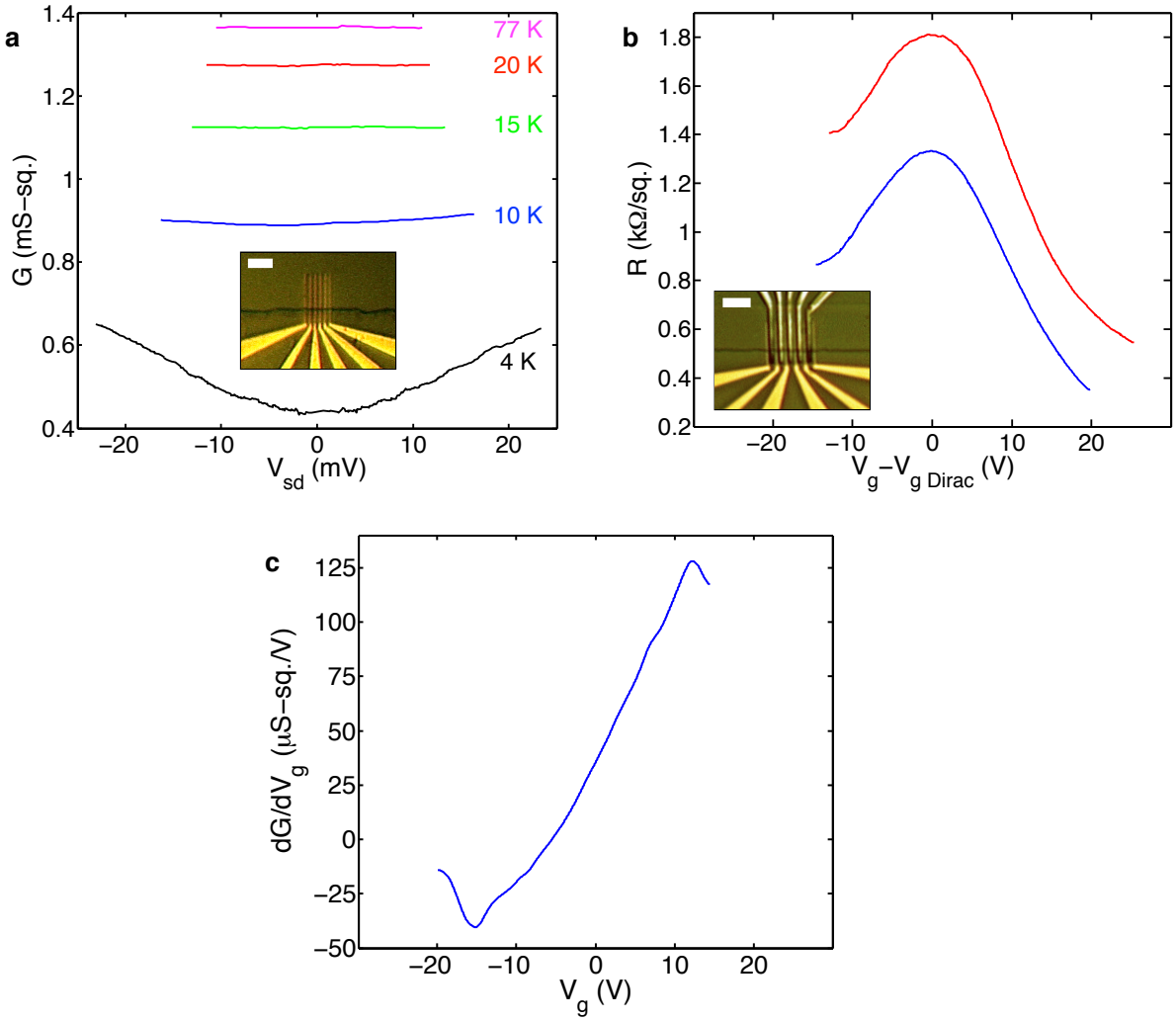

Figure 6.4: (a) Conductance vs. source-drain voltage as a function of temperature. Band gap is observed at 4K as expected for a ribbon of this width (250 nm). Inset: optical micrograph of test structure. Scale bar is 15 μm; channel length is 3 μm. (b) Resistance vs. top-gate voltage, $V_{\rm g}$, relative to voltage at which Dirac point is observed, $V_{\rm g\,Dirac} \approx -4\,{\rm V}$, for two representative self-organized nanoribbons, red, and blue, measured at room temperature. Asymmetry and mobility degradation are due to interaction with NO_2 adhesion layer. Inset: optical micrograph of top-gated devices as studied here and in (c). Scale bar is 3 μm; gate length is 450 nm. (c) $dG/dV_{\rm g}$ vs. top-gate voltage for a similar device, the maximum of which, 130 μS-sq./V, corresponds to electron mobility $\mu_{\rm FE} = 950\,{\rm cm}^2/({\rm V}\cdot{\rm s})$.

area, so the $0.24\,\mathrm{cm}^2$ chip accommodates more than 10,000 transistors. This density was limited primarily by the size of the probe tips used for electrical measurement, but it is, to my knowledge, the highest density of graphene devices achieved to date. The room temperature gating effect is plotted in Fig. 6.5b.

6.5 Outlook

It should be noted that there are likely fundamental differences in the graphene growth among the possible SiC facets, analogous to the dramatic differences in growth speed and layer orientation observed on the (0001) and $(000\bar{1})$ faces,[19, 35] and the $(1\bar{1}0n)$ facet chosen here is possibly not the most desirable in terms of selectivity and quality of graphene produced. This is particularly true of facets prepared on the $(000\bar{1})$ surface, where there is apparently more freedom in facet choice. This is a topic of ongoing work, but the research directions are clear.

These results demonstrate that graphene growth on non-traditional crystal faces is viable and incredibly useful in device fabrication, particularly for production of nanoribbons on a large scale, and fabrication of graphene transistors at a density greater than 40,000 per cm^2 represents a milestone in the development of graphene electronics. Refinement of this approach appears imminent, as ribbon width is reduced and facet selection and dielectric are optimized. Importantly, damage to ribbon edges by violent cutting processes such as O_2 etching is eliminated. Pre-patterning of the SiC substrate is, in general, a new and promising direction in the development of epitaxial graphene electronics, as more complex structures and applications are readily envisaged. This is an important coalescence of top-down and bottom-up lithographies.

6.6 Methods

Substrates were nominally on-axis research-grade semi-insulating $4H$-SiC from Cree, Inc. Arrays of Ni lines were defined on the (0001) or $(000\bar{1})$ SiC crystal face by a

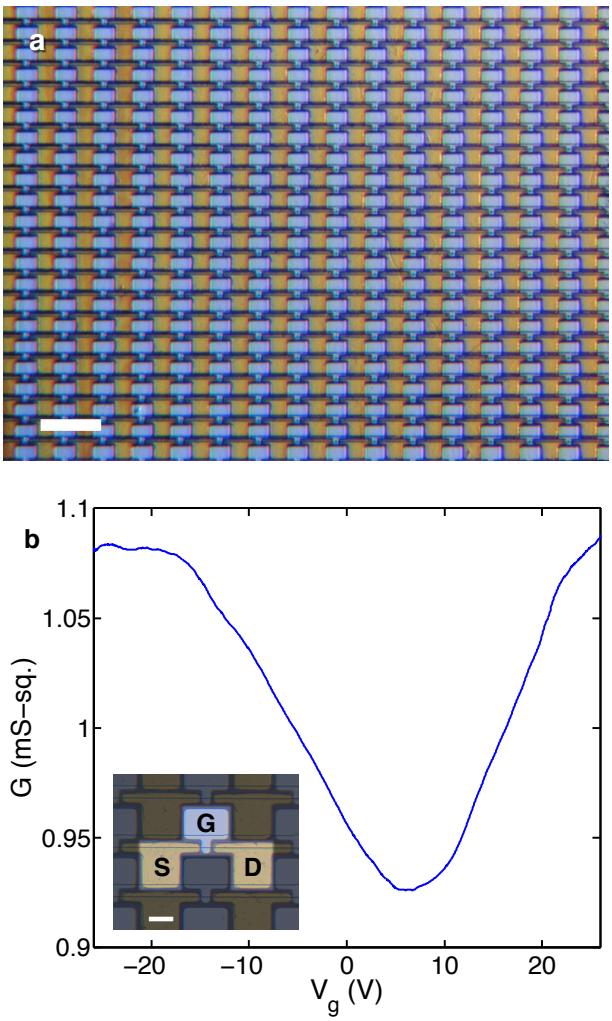

Figure 6.5: (a) Graphene transistor array with density 40,000 devices per cm^2 prepared on SiC$(000\bar{1})$. Scale bar is 100 μm. (b) Room temperature ambipolar gating effect: conductance vs. gate voltage. Inset: an individual FET consisting of source (S), drain (D), graphene channel, and gate (G). Scale bar is 20 μm; channel length is 7 μm.

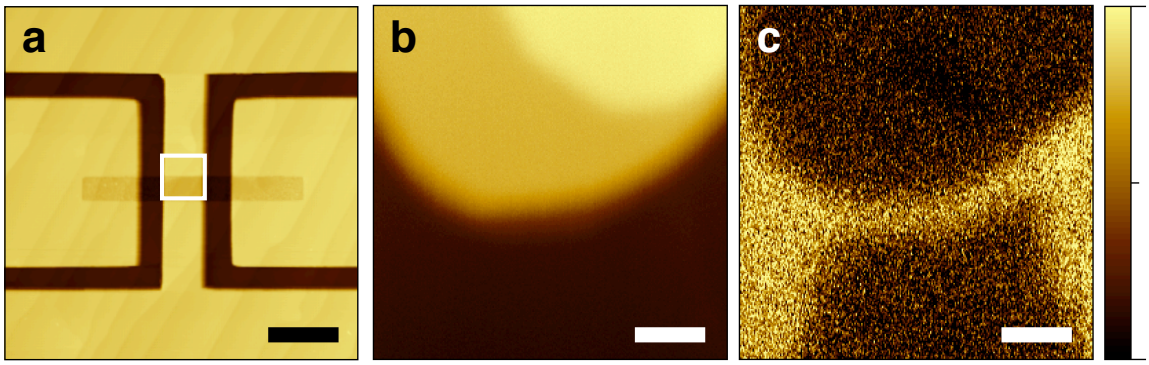

Figure 6.6: (a) AFM (topography) image of patterned nanofacet structure on SiC(0001). (b) Topography detail of the white outlined area in (a) following graphene growth. (c) Corresponding EFM detail highlights graphene nanoribbon relative to adjacent substrate. Scale bars and color scales (far right) in (a), (b), (c) are $2\,\mu$m, 100 nm, 100 nm, $0-150$ nm, $0-34$ nm, and $3.7-8.4$ V, respectively.

standard photolithographic lift-off process, and transferred into the SiC by a 43% SF_6/23% O_2/33% Ar RIE operating at 30 mTorr. RF power was tuned to give a SiC etch rate of 8 Å/s, allowing fine control of the etch depth. Ultrasonic treatment in nitric acid removed Ni from the SiC surface, and further cleaning and graphene growth proceeded as described previously.[4, 5, 35] O_2 RIE operating at 100 mTorr was tuned to give a graphene etch rate of ~ 1 Å/s, and etch time on $(000\bar{1})$ faces was several to a maximum of ten seconds. Samples were mounted with $(1\bar{1}0n)$ facet parallel to ion flux. Contacts were defined by e-beam or photo-lithographic lift-off of 5 nm Pd/60 nm Au. Atomic layer deposition (ALD) of 39 nm Al_2O_3 was performed as described by Williams *et al.*[105] in a commercial Cambridge Nanosystems Savannah ALD system prior to lift-off of an Al top-gate. Al_2O_3 does not deposit uniformly without an adhesion layer (NO_2 functionalization in this case). The Al_2O_3 dielectric constant as deposited is $\kappa = 6$.

Raman mapping was performed with excitation wavelength 532 nm, lateral resolution $\sim 1\,\mu$m, and $0.25-0.5\,\mu$m grid spacing. 2D intensity was taken at 2D maxima near 2725 cm^{-1}. HRTEM measurements were performed by Evans Analytical Group in Raleigh, NC, USA, with acceleration voltage 200 kV.

Electrostatic force microscopy (EFM, related to Kelvin probe force microscopy) allows observation of narrow epitaxial graphene nanoribbons, as shown in Fig. 6.6. Probing of the local relative work functions differentiates epitaxial graphene on the nanofacet from the adjacent substrate as seen in Fig. 6.6c. Here, the SiC step is 20 nm, and the apparent graphene ribbon width as observed by EFM is 50 nm. Because this value is exaggerated by the finite size of the conductive probe tip ($\sim$ 20 nm radius), the true epitaxial graphene ribbon width is estimated as $\lesssim$ 40 nm. EFM data were obtained on a Park XE-70 in enhanced non-contact EFM mode with 2 VAC at $\omega = 17$ kHz on the tip, sample floating, and ω response (pictured) monitored by lock-in amplifier.

Electrical transport measurements were performed at atmospheric pressure. Field-effect mobility is calculated according to $\mu_{\mathrm{FE}} = dG/dV_g \; LW/C$,[47, 58] where G, L, W, and C are square conductance, channel length, width, and dielectric capacitance, respectively, after subtracting contact resistance determined by four-terminal measurement of the device [see Fig. 6.4c].

CHAPTER VII

CONCLUSION

The progress in epitaxial graphene research is incredibly exciting. The growth process is better understood, as demonstrated by much-improved control and sample quality. This has enabled study of basic graphene physics through techniques that are otherwise out of reach, including infrared magneto-transmission, scanning tunneling microscopy, x-ray diffraction, and angle-resolved photoemission spectroscopy (ARPES), and the quality observed on the carbon-face, in particular, encourages optimism with regard to the utility of graphene for electronics.

Ellipsometry is a very useful tool for rapid, non-destructive characterization of film thickness and uniformity, and provides a valuable feedback on the growth process. Widely used and trusted in industry for Å-scale precision, ellipsometric measurement of epitaxial graphene will likely be useful for many years to come.

ARPES observations of linear bands (almost exclusively) on the carbon-face is an important verification of the electronic decoupling introduced by rotational stacking, and is an indicator of the quasi-ordered nature of the stacking. This adds to the body of evidence that encourages further development of carbon-face epitaxial graphene technology and its implementation in electronic devices. A $\sim$ three-layer carbon-face film may prove ideal for use in electronics, as the outer layers may be considered sacrificial (due to interaction with the substrate and dielectric) while the inner sheet is protected, yet easily gated by a top-gate.

Chemical modification of graphene will undoubtedly be an important part of graphene technology, even if graphene oxide in particular does not turn out to be the best choice. Localized chemical modification of selected areas is an important

aspect of that technology.

Epitaxial graphene is attractive to industrial firms precisely because it is largely compatible with existing process technology, but clever exploitation of aspects of the silicon carbide crystal are particularly exciting. Nanofacet growth may eliminate the problems of edge roughness that are endemic to graphene and bring the properties of epitaxial graphene nanoribbons in line with those of their carbon nanotube predecessors, while retaining the the manageability and practicality that they so frustratingly lacked.

APPENDIX A

EPITAXIAL GRAPHENE OXIDATION PROCEDURE

Phrases in *italics* below do not apply to epitaxial graphene samples.

A.1 Penn State pre-oxidation procedure

1. Stir 2 g (10 g) $K_2S_2O_8$ and 2 g (10 g) P_2O_5 into 6 mL (30 mL) H_2SO_4
2. Heat to 80 °C
3. Add sample (20 g), *gives "dark blue mixture"*
4. Thermally isolate and allow to gradually cool to room temperature over 6 hrs.
5. Dilute with distilled water, rinse, and dry

A.2 Hummers and Offeman oxidation process

From Ref. [42]. Numbers in parentheses are those used by Hummers and Penn State, respectively.

1. Pour 11.5 mL (2.3 L, 460 mL) H_2SO_4 into a 75 mL (15 L) beaker, in a crushed ice bath
2. Add 250 mg (50 g, 0 g) $NaNO_3$
3. Add sample (100 g, 20 g)
4. Slowly add 1.5 g (300 g, 60 g) $KMnO_4$ while stirring "vigorously," keeping temperature < 20 °C

5. Remove solution from ice bath, and heat to 35 3 C, stir for 30 min. (Penn State: 2 hrs.)

6. "Mixture gradually thickens with a diminishing in effervescence."

7. "After 20 min., *becomes brownish grey paste* with evolution of only a small amount of gas."

8. Place beaker inside a "spill container", lower fume hood sash

9. Slowly stir in 23 mL (4.6 L, 920 mL) distilled water. Take extreme care as this is a highly exothermic reaction.

    a) Violent effervescence

    b) Temperature increases to 98 °C

    c) Maintain at this temperature for 15 min.

10. Terminate the reaction by adding 70 mL (14 L, 2.8 L) "warm" distilled water and (50 mL) 30% H_2O_2

11. "Upon treatment with peroxide, the *suspension turns bright yellow*"

12. "Peroxide treatment reduces residual permanganate and manganese dioxide to colorless soluble manganese sulfate"

13. Wash with 25 mL 1:10 HCl (5 L) to remove metal ions

14. Rinse sample in DI H_2O

15. N_2 dry

Epitaxial graphene samples, intially a dark grey, become a transparent light grey after oxidation. Note that when oxidizing a patterned sample, "stirring" should be replaced by "swishing"—that is, we do not want to scratch off the contacts or the

patterned structure, so we "swish" (i.e. manually agitate without the use of a stir rod) the beaker around to dissolve the solutes and maintain temperature. This seems to work well.

REFERENCES

[1] Ando, T., Fowler, A. B., and Stern, F., "Electronic-properties of two-dimensional systems," *Rev. Mod. Phys.*, vol. 54, no. 2, pp. 437–672, 1982.

[2] Anwar, A., Nabet, B., Culp, J., and Castro, F., "Effects of electron confinement on thermionic emission current in a modulation doped heterostructure," *J. Applied Phys.*, vol. 85, pp. 2663–2666, Mar. 1999.

[3] Bekyarova, E., Itkis, M. E., Ramesh, P., Berger, C., Sprinkle, M., de Heer, W. A., and Haddon, R. C., "Chemical modification of epitaxial graphene: Spontaneous grafting of aryl groups," *J. Am. Chem. Soc.*, vol. 131, p. 1336, Feb. 2009.

[4] Berger, C., Song, Z. M., Li, T. B., Li, X. B., Ogbazghi, A. Y., Feng, R., Dai, Z. T., Marchenkov, A. N., Conrad, E. H., First, P. N., and de Heer, W. A., "Ultrathin epitaxial graphite: 2D electron gas properties and a route toward graphene-based nanoelectronics," *J. Phys. Chem. B*, vol. 108, no. 52, pp. 19912 –19916, 2004.

[5] Berger, C., Song, Z. M., Li, X. B., Wu, X. S., Brown, N., Naud, C., Mayo, D., Li, T. B., Hass, J., Marchenkov, A. N., Conrad, E. H., First, P. N., and de Heer, W. A., "Electronic confinement and coherence in patterned epitaxial graphene," *Science*, vol. 312, pp. 1191 – 1196, May 2006.

[6] Biedermann, L. B., Bolen, M. L., Capano, M. A., Zemlyanov, D., and Reifenberger, R. G., "Insights into few-layer epitaxial graphene growth on 4H-SiC(000$\bar{1}$) substrates from STM studies," *Physical Review B*, vol. 79, no. 12, p. 125411, 2009.

[7] Boehm, H.-P., Setton, R., and Stumpp, E., "Nomenclature and terminology of graphite intercalation compounds," *Pure & Applied Chem.*, vol. 66, pp. 1893 –1901, 1994.

[8] Boehm, H., Clauss, A., Fischer, G., and Hofmann, U., "Dünnste Kohlenstoff-folien," *Z. Naturforschung*, vol. 17b, pp. 150 – 153, 1962.

[9] Bolotin, K. I., Sikes, K. J., Hone, J., Stormer, H. L., and Kim, P., "Temperature-dependent transport in suspended graphene," *Physical Review Letters*, vol. 101, p. 096802, Aug. 2008.

[10] Bolotin, K. I., Ghahari, F., Shulman, M. D., Stormer, H. L., and Kim, P., "Fractional quantum hall effect and insulating phase of dirac electrons in graphene," *Nature*, vol. 462, p. 196, 2009.

[11] Borovikov, V. and Zangwill, A., "Step bunching of vicinal 6H-SiC{0001} surfaces," *Physical Review B*, vol. 79, p. 245413, Jun 2009.

[12] Borovikov, V. and Zangwill, A., "Step-edge instability during epitaxial growth of graphene from SiC(0001)," *Physical Review B*, vol. 80, no. 12, p. 121406, 2009.

[13] Bostwick, A., Ohta, T., Seyller, T., Horn, K., and Rotenberg, E., "Quasiparticle dynamics in graphene," *Nature Physics*, vol. 3, pp. 36–40, Jan. 2007.

[14] Brodie, B. *Phil. Trans.*, vol. 149, p. 249, 1859.

[15] Bychkov, Y. A. and Martinez, G., "Magnetoplasmon excitations in graphene for filling factors $\nu \leq 6$," *Physical Review B*, vol. 77, p. 125417, Mar 2008.

[16] Calandra, M. and Mauri, F., "Electron-phonon coupling and electron self-energy in electron-doped graphene: Calculation of angular-resolved photoemission spectra," *Physical Review B*, vol. 76, p. 205411, Nov 2007.

[17] Chen, Z., Lin, Y.-M., Rooks, M. J., and Avouris, P., "Graphene nano-ribbon electronics," *Physica E*, vol. 40, no. 2, pp. 228 – 232, 2007.

[18] Cree, Inc., "Silicon carbide substrates and epitaxy." http://www.cree.com/products/pdf/MAT-CATALOG.pdf, 2009. [Online; accessed 1 Mar. 2010].

[19] de Heer, W. A., Berger, C., Wu, X. S., First, P. N., Conrad, E. H., Li, X. B., Li, T. B., Sprinkle, M., Hass, J., Sadowski, M. L., Potemski, M., and Martinez, G., "Epitaxial graphene," *Solid State Communications*, vol. 143, pp. 92 – 100, July 2007.

[20] dos Santos, J. M. B. L., Peres, N. M. R., and Neto, A. H. C., "Graphene bilayer with a twist: Electronic structure," *Physical Review Letters*, vol. 99, no. 25, p. 256802, 2007.

[21] Du, X., Skachko, I., Barker, A., and Andrei, E. Y., "Approaching ballistic transport in suspended graphene," *Nature Nanotechnology*, vol. 3, pp. 491–495, Aug. 2008.

[22] Du, X., Skachko, I., Duerr, F., Luican, A., and Andrei, E. Y., "Fractional quantum hall effect and insulating phase of dirac electrons in graphene," *Nature*, vol. 462, p. 192, 2009.

[23] Emtsev, K. V., Speck, F., Seyller, T., Ley, L., and Riley, J. D., "Interaction, growth, and ordering of epitaxial graphene on SiC{0001} surfaces: A comparative photoelectron spectroscopy study," *Physical Review B*, vol. 77, p. 155303, Apr 2008.

[24] Emtsev, K. V., Bostwick, A., Horn, K., Jobst, J., Kellogg, G. L., Ley, L., McChesney, J. L., Ohta, T., Reshanov, S. A., Rohrl, J., Rotenberg, E., Schmid, A. K., Waldmann, D., Weber, H. B., and Seyller, T., "Towards wafer-size graphene layers by atmospheric pressure graphitization of silicon carbide," *Nature Materials*, vol. 8, pp. 203 – 207, Mar. 2009.

[25] Farmer, D. B., Chiu, H.-Y., Lin, Y.-M., Jenkins, K. A., Xia, F., and Avouris, P., "Utilization of a buffered dielectric to achieve high field-effect carrier mobility in graphene transistors," *Nano Letters*, vol. 9, pp. 4474 – 4478, dec 2009.

[26] Forbeaux, I., Themlin, J.-M., and Debever, J.-M., "Heteroepitaxial graphite on 6H-SiC(0001): interface formation through conduction-band electronic structure," *Physical Review B*, vol. 58, pp. 16396–16406, Dec 1998.

[27] Fujita, M., Wakabayashi, K., Nakada, K., and Kusakabe, K., "Peculiar localized state at zigzag graphite edge," *J. Phys. Soc. Jpn.*, vol. 65, no. 7, pp. 1920 – 1923, 1996.

[28] Galuska, A. A., Madden, H. H., and Allred, R. E., "Electron-spectroscopy of graphite, graphite oxide and amorphous-carbon," *Applied Surface Science*, vol. 32, pp. 253–272, July 1988.

[29] Geim, A. K. and Novoselov, K. S., "The rise of graphene," *Nature Materials*, vol. 6, pp. 183–191, Mar. 2007.

[30] Gilje, S., Han, S., Wang, M., Wang, K., and Kaner, R., "A chemical route to graphene for device applications," *Nano Letters*, vol. 7, no. 11, pp. 3394–3398, 2007.

[31] Gomez-Navarro, C., Weitz, R., Bittner, A., Scolari, M., Mews, A., Burghard, M., and Kern, K., "Electronic transport properties of individual chemically reduced graphene oxide sheets," *Nano Letters*, vol. 7, no. 11, pp. 3499–3503, 2007.

[32] Haering, R., "Band structure of rhombohedral graphite," *Canadian J. Phys.*, vol. 36, no. 3, pp. 352 – 362, 1958.

[33] Han, M. Y., Brant, J. C., and Kim, P., "Electron transport in disordered graphene nanoribbons," *Physical Review Letters*, vol. 104, p. 056801, 2010.

[34] Han, M. Y., Ozyilmaz, B., Zhang, Y., and Kim, P., "Energy band-gap engineering of graphene nanoribbons," *Physical Review Letters*, vol. 98, no. 20, p. 206805, 2007.

[35] Hass, J., de Heer, W. A., and Conrad, E. H., "The growth and morphology of epitaxial multilayer graphene," *J. Phys.: Condens. Matter*, vol. 20, no. 32, p. 323202, 2008.

[36] Hass, J., Feng, R., Millan-Otoya, J. E., Li, X., Sprinkle, M., First, P. N., de Heer, W. A., Conrad, E. H., and Berger, C., "Structural properties of the multilayer graphene/4H-SiC(000$\bar{1}$) system as determined by surface x-ray diffraction," *Physical Review B*, vol. 75, p. 214109, June 2007.

[37] Hass, J., Varchon, F., Millán-Otoya, J. E., Sprinkle, M., Sharma, N., de Heer, W. A., Berger, C., First, P. N., Magaud, L., and Conrad, E. H., "Why multilayer graphene on 4H-SiC(000$\bar{1}$) behaves like a single sheet of graphene," *Physical Review Letters*, vol. 100, no. 12, p. 125504, 2008.

[38] Hass, J. R., *Structural characterization of epitaxial graphene on silicon carbide*. PhD thesis, Georgia Institute of Technology, 2008.

[39] Heinze, S., Tersoff, J., Martel, R., Derycke, V., Appenzeller, J., and Avouris, P., "Carbon nanotubes as schottky barrier transistors," *Physical Review Letters*, vol. 89, p. 106801, Aug 2002.

[40] Hiebel, F., Mallet, P., Varchon, F., Magaud, L., and Veuillen, J.-Y., "Graphene-substrate interaction on 6H-SiC (000$\bar{1}$): A scanning tunneling microscopy study," *Physical Review B*, vol. 78, p. 153412, Oct 2008.

[41] Hill, R. M., "Hopping conduction in amorphous solids," *Philos. Mag.*, vol. 24, no. 192, pp. 1307–&, 1971.

[42] Hummers, W. S. and Offeman, R. E., "Preparation of graphitic oxide," *J. Am. Chem. Soc.*, vol. 80, no. 6, pp. 1339–1339, 1958.

[43] Jellison, G. E., Hunn, J. D., and Lee, H. N., "Measurement of optical functions of highly oriented pyrolytic graphite in the visible," *Physical Review B*, vol. 76, p. 085125, 2007.

[44] Jiang, Z., Henriksen, E. A., Tung, L. C., Wang, Y.-J., Schwartz, M. E., Han, M. Y., Kim, P., and Stormer, H. L., "Infrared spectroscopy of landau levels of graphene," *Physical Review Letters*, vol. 98, no. 19, p. 197403, 2007.

[45] Jiao, L., Zhang, L., Wang, X., Diankov, G., and Dai, H., "Narrow graphene nanoribbons from carbon nanotubes," *Nature*, vol. 458, pp. 877 – 880, Apr. 2009.

[46] Jobst, J., Waldmann, D., Speck, F., Hirner, R., Maude, D. K., Seyller, T., and Weber, H. B., "Quantum oscillations and quantum Hall effect in epitaxial graphene," *Physical Review B*, vol. 81, p. 195434, May 2010.

[47] Kedzierski, J., Hsu, P. L., Healey, P., Wyatt, P. W., Keast, C. L., Sprinkle, M., Berger, C., and de Heer, W. A., "Epitaxial graphene transistors on SiC substrates," *IEEE T. Electron Dev.*, vol. 55, pp. 2078 – 2085, Aug. 2008.

[48] Kittel, C., *Introduction to Solid State Physics*. Wiley, 7 ed., 1995.

[49] Knox, K. R., Wang, S., Morgante, A., Cvetko, D., Locatelli, A., Mentes, T. O., Niño, M. A., Kim, P., and Osgood, R. M., "Spectromicroscopy of single and multilayer graphene supported by a weakly interacting substrate," *Physical Review B*, vol. 78, p. 201408, Nov 2008.

[50] Kong, H. S., Glass, J. T., and Davis, R. F., "Chemical vapor deposition and characterization of 6H-SiC thin films on off-axis 6H-SiC substrates," *J. Applied Phys.*, vol. 64, no. 5, pp. 2672 – 2679, 1988.

[51] Kong, J., Franklin, N. R., Zhou, C., Chapline, M. G., Peng, S., Cho, K., and Dai, H., "Nanotube molecular wires as chemical sensors," *Science*, vol. 287, no. 5453, pp. 622–625, 2000.

[52] Kovtyukhova, N., Ollivier, P., Martin, B., Mallouk, T., Chizhik, S., Buzaneva, E., and Gorchinskiy, A., "Layer-by-layer assembly of ultrathin composite films from micron-sized graphite oxide sheets and polycations," *Chem. Mater.*, vol. 11, no. 3, pp. 771–778, 1999.

[53] Latil, S., Meunier, V., and Henrard, L., "Massless fermions in multilayer graphitic systems with misoriented layers: Ab initio calculations and experimental fingerprints," *Physical Review B*, vol. 76, p. 201402, Nov 2007.

[54] Lee, Y. S., Nardelli, M. B., and Marzari, N., "Band structure and quantum conductance of nanostructures from maximally localized wannier functions: The case of functionalized carbon nanotubes," *Physical Review Letters*, vol. 95, p. 076804, Aug. 2005.

[55] Li, X., Zhang, G., Bai, X., Sun, X., Wang, X., Wang, E., and Dai, H., "Highly conducting graphene sheets and Langmuir-Blodgett films," *Nature Nanotechnology*, vol. 3, pp. 538–542, Sept. 2008.

[56] Li, X., *Epitaxial graphene films on SiC: growth, characterization, and devices*. PhD thesis, Georgia Institute of Technology, 2008.

[57] Li, X., Wu, X., Sprinkle, M., Ming, F., Ruan, M., Hu, Y., Berger, C., and de Heer, W. A., "Top- and side-gated epitaxial graphene field effect transistors," *Phys. Stat. Sol. A*, vol. 207, p. 286, 2010.

[58] Lin, Y.-M., Dimitrakopoulos, C., Jenkins, K. A., Farmer, D. B., Chiu, H.-Y., Grill, A., and Avouris, P., "100-GHz transistors from wafer-scale epitaxial graphene," *Science*, vol. 327, no. 5966, p. 662, 2010.

[59] Lin, Y.-M., Jenkins, K. A., Valdes-Garcia, A., Small, J. P., Farmer, D. B., and Avouris, P., "Operation of graphene transistors at Gigahertz frequencies," *Nano Letters*, vol. 9, no. 0, p. 422, 2009.

[60] Martin, J., Akerman, N., Ulbricht, G., Lohmann, T., Smet, J. H., von Klitzing, K., and Yacoby, A., "Observation of electron-hole puddles in graphene using a scanning single-electron transistor," *Nature Physics*, vol. 4, pp. 144 –148, 2008.

[61] McClure, J. W., "Band structure of graphite and de Haas-van Alphen effect," *Phys. Rev.*, vol. 108, pp. 612 – 618, Nov 1957.

[62] McLean, T. P., "The absorption edge spectrum of semiconductors," *Prog. Semicond.*, vol. 5, p. 53, 1960.

[63] Meyer, F. and Loyen, G. J., "Ellipsometry applied to surface problems," *Acta Electron.*, vol. 18, pp. 33–38, 1975.

[64] Meyer, J., Geim, A., Katsnelson, M., Novoselov, K., Obergfell, D., Roth, S., Girit, C., and Zettl, A., "On the roughness of single- and bi-layer graphene membranes," *Solid State Communications*, vol. 143, no. 1-2, pp. 101 – 109, 2007. Exploring graphene - Recent research advances.

[65] Miller, D. L., Kubista, K. D., Rutter, G. M., Ruan, M., de Heer, W. A., First, P. N., and Stroscio, J. A., "Observing the quantization of zero mass carriers in graphene," *Science*, vol. 324, pp. 924–927, May 2009.

[66] Moon, J., Curtis, D., Hu, M., Wong, D., McGuire, C., Campbell, P., Jernigan, G., Tedesco, J., VanMil, B., Myers-Ward, R., Eddy, C., and Gaskill, D., "Epitaxial-graphene RF field-effect transistors on Si-face 6H-SiC substrates," *IEEE Electron Dev. Letters*, vol. 30, pp. 650 – 652, June 2009.

[67] Nakada, K., Fujita, M., Dresselhaus, G., and Dresselhaus, M. S., "Edge state in graphene ribbons: Nanometer size effect and edge shape dependence," *Physical Review B*, vol. 54, pp. 17954 – 17961, Dec 1996.

[68] Nakagawa, H., Tanaka, S., and Suemune, I., "Self-ordering of nanofacets on vicinal SiC surfaces," *Physical Review Letters*, vol. 91, p. 226107, Nov 2003.

[69] Nakajima, A., Yokoya, H., Furukawa, Y., and Yonezu, H., "Step control of vicinal 6H–SiC(0001) surface by H_2 etching," *J. Applied Phys.*, vol. 97, no. 10, p. 104919, 2005.

[70] Nakamura, S., Kimoto, T., Matsunami, H., Tanaka, S., Teraguchi, N., and Suzuki, A., "Formation of periodic steps with a unit-cell height on 6H–SiC (0001) surface by HCl etching," *Applied Physics Letters*, vol. 76, no. 23, pp. 3412 – 3414, 2000.

[71] Nie, S., Lee, C., Feenstra, R., Ke, Y., Devaty, R., Choyke, W., Inoki, C., Kuan, T., and Gu, G., "Step formation on hydrogen-etched 6H-SiC{0001} surfaces," *Surface Science*, vol. 602, no. 17, pp. 2936 – 2942, 2008.

[72] Novoselov, K. S., Geim, A. K., Morozov, S. V., Jiang, D., Katsnelson, M. I., Grigorieva, I. V., Dubonos, S. V., and Firsov, A. A., "Two-dimensional gas of massless dirac fermions in graphene," *Nature*, vol. 438, no. 7065, pp. 197–200, 2005.

[73] Novoselov, K. S., Geim, A. K., Morozov, S. V., Jiang, D., Zhang, Y., Dubonos, S. V., Grigorieva, I. V., and Firsov, A. A., "Electric field effect in atomically thin carbon films," *Science*, vol. 306, no. 5296, pp. 666–669, 2004.

[74] Ohta, T., Bostwick, A., McChesney, J. L., Seyller, T., Horn, K., and Rotenberg, E., "Interlayer interaction and electronic screening in multilayer graphene investigated with angle-resolved photoemission spectroscopy," *Physical Review Letters*, vol. 98, no. 20, p. 206802, 2007.

[75] Orlita, M., Faugeras, C., Plochocka, P., Neugebauer, P., Martinez, G., Maude, D. K., Barra, A.-L., Sprinkle, M., Berger, C., de Heer, W. A., and Potemski, M., "Approaching the dirac point in high-mobility multilayer epitaxial graphene," *Physical Review Letters*, vol. 101, no. 26, p. 267601, 2008.

[76] Rhoderick, E. H. and Williams, R. H., *Metal-Semiconductor Contacts*. Oxford, 2 ed., 1988.

[77] Robinson, J., Weng, X., Trumbell, K., Cavalero, R., Wetherington, M., Frantz, E., LaBella, M., Hughes, Z., Fanton, M., and Snyder, D., "Nucleation of epitaxial graphene on SiC(0001)," *ACS Nano*, vol. 4, p. 153, 2010.

[78] Sadowski, M. L., Martinez, G., Potemski, M., Berger, C., and de Heer, W. A., "Landau level spectroscopy of ultrathin graphite layers," *Physical Review Letters*, vol. 97, no. 26, p. 266405, 2006.

[79] Sadowski, M. L., Martinez, G., Potemski, M., Berger, C., and de Heer, W. A., "Magnetospectroscopy of epitaxial few-layer graphene," *Solid State Communications*, vol. 143, pp. 123–125, July 2007.

[80] Schedin, F., Geim, A. K., Morozov, S. V., Hill, E. W., Blake, P., Katsnelson, M. I., and Novoselov, K. S., "Detection of individual gas molecules adsorbed on graphene," *Nature Materials*, vol. 6, pp. 652–655, Sept. 2007.

[81] Sharma, N., *Microscopic and Spectroscopic Studies of Epitaxial Graphene on SiC*. PhD thesis, Georgia Institute of Technology, 2009.

[82] Shen, T., Gu, J. J., Xu, M., Wu, Y. Q., Bolen, M. L., Capano, M. A., Engel, L. W., and Ye, P. D., "Observation of quantum-Hall effect in gated epitaxial graphene grown on SiC (0001)," *Applied Physics Letters*, vol. 95, no. 17, p. 172105, 2009.

[83] Smith, C. and McGilp, J. F., "Ellipsometry — Surface and Interface Physics — Trinity College Dublin." http://www.tcd.ie/Physics/Surfaces/ellipsometry2.php, 2010. [Online; accessed 1 Mar. 2010].

[84] Sprinkle, M., Hicks, J., Tejeda, A., Taleb-Ibrahimi, A., Fèvre, P. L., Bertran, F., Tinkey, H., Clark, M. C., Soukiassian, P., Martinotti, D., Hass, J., de Heer, W. A., Berger, C., and Conrad, E. H., "Structure and electronic properties of epitaxial graphene grown on SiC," *J. Phys. D: Appl. Phys.*, In press 2010.

[85] Sprinkle, M., Ruan, M., Wu, X., Hu, Y., Rubio-Roy, S., Hankinson, J., Madiomanana, N. K., Berger, C., and de Heer, W. A., "Directed self-organization of graphene nanoribbons on SiC," *arXiv:1002.0775*, Feb. 2010.

[86] Sprinkle, M., Siegel, D., Hu, Y., Hicks, J., Soukiassian, P., Tejeda, A., Taleb-Ibrahimi, A., Fevre, P. L., Bertran, F., Berger, C., de Heer, W. A., Lanzara, A., and Conrad, E. H., "First direct observation of a nearly ideal graphene band structure," *Physical Review Letters*, vol. 103, p. 226803, 2009.

[87] Sprinkle, M., Soukiassian, P., de Heer, W. A., Berger, C., and Conrad, E. H., "Epitaxial graphene: the material for graphene electronics," *Physica Status Solidi*, vol. 3, pp. A91 – A94, 2009.

[88] Stankovich, S., Dikin, D. A., Piner, R. D., Kohlhaas, K. A., Kleinhammes, A., Jia, Y., Wu, Y., Nguyen, S. T., and Ruoff, R. S., "Synthesis of graphene-based nanosheets via chemical reduction of exfoliated graphite oxide," *Carbon*, vol. 45, pp. 1558–1565, June 2007.

[89] Syväjärvi, M., Yakimova, R., and Janzn, E., "Step-bunching in SiC epitaxy: anisotropy and influence of growth temperature," *J. Cryst. Growth*, vol. 236, no. 1-3, pp. 297 – 304, 2002.

[90] Tan, Y.-W., Zhang, Y., Bolotin, K., Zhao, Y., Adam, S., Hwang, E. H., Das Sarma, S., Stormer, H. L., and Kim, P., "Measurement of scattering rate and minimum conductivity in graphene," *Physical Review Letters*, vol. 99, p. 246803, Dec 2007.

[91] Tanaka, S., Morita, K., and Hibino, H., "Anisotropic layer-by-layer growth of graphene on vicinal SiC(0001) surfaces," *Physical Review B*, vol. 81, p. 041406, Jan 2010.

[92] Tapasztó, L., Dobrik, G., Lambin, P., and Biró, L. P., "Tailoring the atomic structure of graphene nanoribbons by scanning tunnelling microscope lithography," *Nature Nanotechnology*, vol. 3, pp. 397 – 401, July 2008.

[93] Thompson-Flagg, R. C., Moura, M. J. B., and Marder, M., "Rippling of graphene," *Europhys. Letters*, vol. 85, no. 4, p. 46002, 2009.

[94] Tikhonenko, F. V., Kozikov, A. A., Savchenko, A. K., and Gorbachev, R. V., "Transition between electron localization and antilocalization in graphene," *Physical Review Letters*, vol. 103, p. 226801, Nov 2009.

[95] Tompkins, H., "Very thin films," in *Spectroscopic Ellipsometry Short Course*, J.A. Woollam Co., Sept. 2006.

[96] Van Bommel, A., Crombeen, J., and Van Tooren, A., "LEED and Auger electron observations of the SiC(0001) surface," *Surface Science*, vol. 48, pp. 463–472, Mar. 1975.

[97] Varchon, F., Feng, R., Hass, J., Li, X., Nguyen, B. N., Naud, C., Mallet, P., Veuillen, J. Y., Berger, C., Conrad, E. H., and Magaud, L., "Electronic structure of epitaxial graphene layers on SiC: Effect of the substrate," *Physical Review Letters*, vol. 99, p. 126805, Sept. 2007.

[98] Virojanadara, C., Yakimova, R., Osiecki, J., Syvjrvi, M., Uhrberg, R., Johansson, L., and Zakharov, A., "Substrate orientation: A way towards higher quality monolayer graphene growth on 6H-SiC(0001)," *Surface Science*, vol. 603, no. 15, pp. L87 – L90, 2009.

[99] Wagner, L., Young, R., and Sugerman, A., "A note on the correlation between the schottky-diode barrier height and the ideality factor as determined from I-V measurements," *IEEE Electron Device Letters*, vol. 4, no. 9, pp. 320–322, 1983.

[100] Wakabayashi, K., "Electronic transport properties of nanographite ribbon junctions," *Physical Review B*, vol. 64, p. 125428, Sep 2001.

[101] Wakabayashi, K., Fujita, M., Ajiki, H., and Sigrist, M., "Electronic and magnetic properties of nanographite ribbons," *Physical Review B*, vol. 59, pp. 8271–8282, Mar 1999.

[102] Wallace, P. R., "The band theory of graphite," *Phys. Rev.*, vol. 71, pp. 622–634, May 1947.

[103] Wikipedia, "ARPES — Wikipedia, the free encyclopedia." http://en.wikipedia.org/wiki/ARPES, 2010. [Online; accessed 1 Mar. 2010].

[104] Wikipedia, "Birefringence — Wikipedia, the free encyclopedia." http://en.wikipedia.org/wiki/Birefringence, 2010. [Online; accessed 1 Mar. 2010].

[105] Williams, J. R., DiCarlo, L., and Marcus, C. M., "Quantum Hall effect in a gate-controlled p-n junction of graphene," *Science*, vol. 317, no. 5838, pp. 638 – 641, 2007.

[106] Wu, X. S., Sprinkle, M., Li, X. B., Ming, F., Berger, C., and de Heer, W. A., "Epitaxial-graphene/graphene-oxide junction: An essential step towards epitaxial graphene electronics," *Physical Review Letters*, vol. 101, p. 026801, July 2008.

[107] Wu, X. S., Li, X. B., Song, Z. M., Berger, C., and de Heer, W. A., "Weak anti-localization in epitaxial graphene: evidence for chiral electrons," *Physical Review Letters*, vol. 98, p. 136801, 2007.

[108] Wu, X., Hu, Y., Ruan, M., Madiomanana, N. K., Hankinson, J., Sprinkle, M., Berger, C., and de Heer, W. A., "Half integer quantum Hall effect in high mobility single layer epitaxial graphene," *Applied Physics Letters*, vol. 95, p. 223108, 2009.

[109] Yamamoto, K., Akita, S., and Nakayama, Y., "Orientation and purification of carbon nanotubes using ac electrophoresis," *J. Phys. D: Applied Phys.*, vol. 31, no. 8, pp. L34–L36, 1998.

[110] Zhang, Y. B., Tan, Y. W., Stormer, H. L., and Kim, P., "Experimental observation of the quantum Hall effect and Berry's phase in graphene," *Nature*, vol. 438, no. 7065, pp. 201–204, 2005.

[111] Zhi, C. Y., Bando, Y., Tang, C. C., and Golberg, D., "Engineering of electronic structure of boron-nitride nanotubes by covalent functionalization," *Physical Review B*, vol. 74, p. 153413, Oct. 2006.

[112] Zhou, S. Y., Gweon, G.-H., Fedorov, A. V., First, P. N., de Heer, W. A., Lee, D.-H., Guinea, F., Castro Neto, A. H., and Lanzara, A., "Substrate-induced bandgap opening in epitaxial graphene," *Nature Materials*, vol. 6, pp. 770–775, Oct. 2007.

[113] Zhou, S. Y., Gweon, G.-H., Graf, J., Fedorov, A. V., Spataru, C. D., Diehl, R. D., Kopelevich, Y., Lee, D.-H., Louie, S. G., and Lanzara, A., "First direct observation of Dirac fermions in graphite," *Nature Physics*, vol. 2, pp. 595–599, Sept. 2006.

VITA

Michael W. Sprinkle was born in Alberta, Canada, in 1981. He has lived in Virginia, Utah, Montana, Texas, Arizona, and Brazil. Michael earned a B.S. in physics from Brigham Young University in Provo, Utah, in 2005, studying chemical vapor deposition and manipulation of carbon nanotubes under Prof. Robert C. Davis. His interest in carbon nanotubes and carbon electronics led him to Prof. Walt A. de Heer's group at Georgia Tech in 2005.